

AD-A068 211

SPERRY RESEARCH CENTER SUDBURY MASS
LOW EM SIGNATURE RESPONSE TECHNIQUES. (U)

MAR 79 C L BENNETT, H MIERAS, S L TEEETER
SCRC-CR-78-61

F/G 17/9

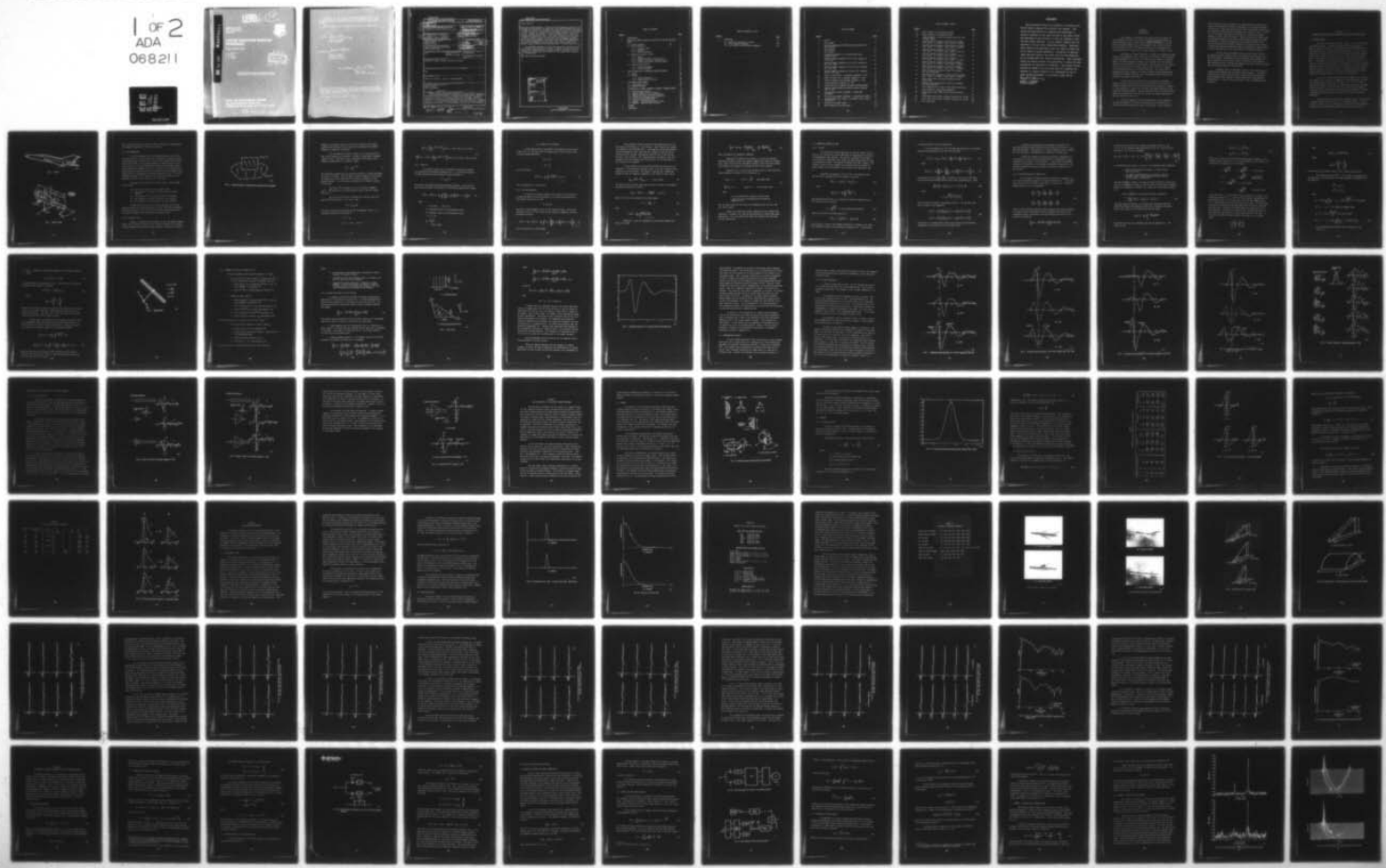
UNCLASSIFIED

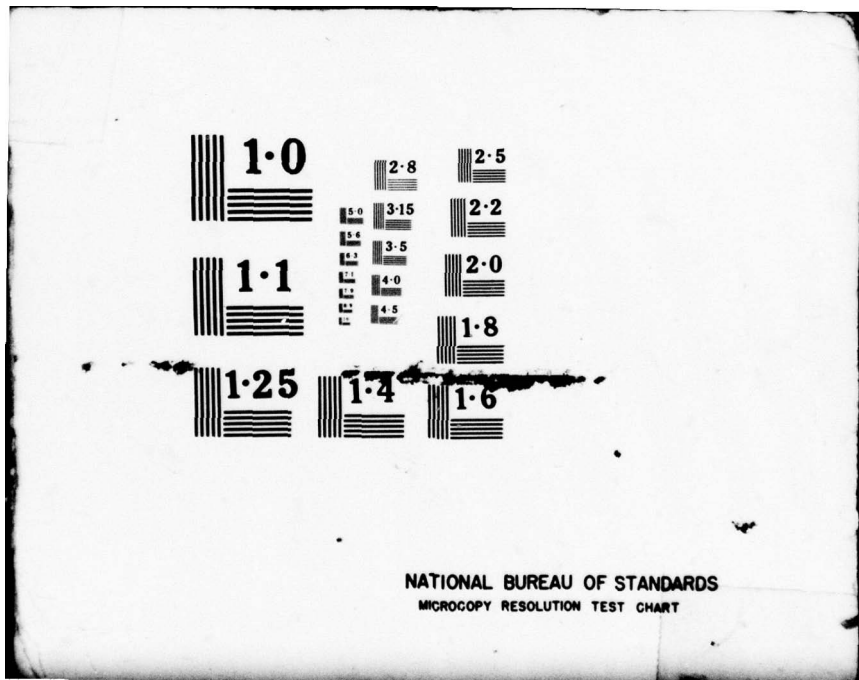
F30602-77-C-0166

NL

RADC-TR-78-287

1 OF 2
ADA
068211

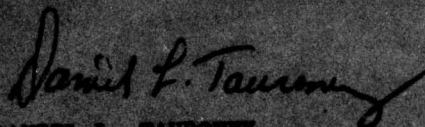




This report has been reviewed by the RADOC Information Office (OI) and is releasable to the National Technical Information Service (NTIS). At NTIS it will be releasable to the general public, including foreign nations.

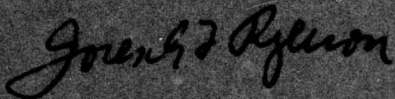
RADC-TR-78-287 has been reviewed and is approved for publication.

APPROVED:



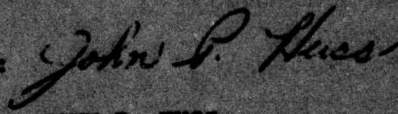
DANIEL L. TAURONY
Project Engineer

APPROVED:



JOSEPH L. RYERSON
Technical Director
Surveillance Division

FOR THE COMMANDER:



JOHN P. HUSS
Acting Chief, Plans Office

If your address has changed or if you wish to be removed from the RADOC mailing list, or if the addressee is no longer employed by your organization, please notify RADOC (OCTM) Griffiss AFB NY. This will assist us in maintaining a current mailing list.

Do not return this copy. Retain or destroy.

UNCLASSIFIED

SECURITY CLASSIFICATION OF THIS PAGE (When Data Entered)

(19) REPORT DOCUMENTATION PAGE

READ INSTRUCTIONS
BEFORE COMPLETING FORM

3. RECIPIENT'S CATALOG NUMBER

1. REPORT NUMBER RADCR-TR-78- 287	2. GOVT ACCESSION NO.	3. RECIPIENT'S CATALOG NUMBER
4. TITLE (or NAME OF REPORT) LOW EM SIGNATURE RESPONSE TECHNIQUES .		9. TYPE OF REPORT & PERIOD COVERED Final Technical Report. Sep 77 - Oct 78
6. AUTHOR(s) C. L. Bennett, S. L. Teeter H. Mieras, J. P. Toomey		14. CONTRACTOR OR GRANT NUMBER(s) SCRC-CR-78-61
7. PERFORMING ORGANIZATION NAME AND ADDRESS Sperry Research Center 100 North Road Sudbury MA 01776		10. PROGRAM ELEMENT, PROJECT, TASK AREA & WORK UNIT NUMBERS 63789P 23140009
11. CONTROLLING OFFICE NAME AND ADDRESS Rome Air Development Center (OCTM) Griffiss AFB NY 13441		12. REPORT DATE March 1979
14. MONITORING AGENCY NAME & ADDRESS (if different from Controlling Office) Same		15. SECURITY CLASS. (of this report) UNCLASSIFIED
16. DISTRIBUTION STATEMENT (of this Report) Approved for public release; distribution unlimited.		15a. DECLASSIFICATION DOWNGRADING SCHEDULE N/A
17. DISTRIBUTION STATEMENT (of the abstract entered in Block 20, if different from Report) Same		
18. SUPPLEMENTARY NOTES RADC Project Engineer: Daniel L. Tauroney (OCTM)		
19. KEY WORDS (Continue on reverse side if necessary and identify by block number) Space-Time Integral Equation Impulse Response Frequency Response (extends)		
20. ABSTRACT (Continue on reverse side if necessary and identify by block number) In this study the technique for computing the smoothed impulse response has been extended to the case of scattering from triangular plates, quadrilateral plates, and more refined aircraft models that consist of a cylindrical fuselage with triangular or quadrilateral plates for the wings, stabilizers, and rudder. To the knowledge of Sperry, this is the first time that a successful solution of these problems has been obtained. The numerical techniques that were developed consisted of the simultaneous solution of two vector (Cont'd)		

DD FORM 1473A EDITION OF 1 NOV 65 IS OBSOLETE

UNCLASSIFIED

SECURITY CLASSIFICATION OF THIS PAGE (When Data Entered)

408 199 SW 79 05 03 003

UNCLASSIFIED

SECURITY CLASSIFICATION OF THIS PAGE(When Data Entered)

Item 20 (Cont'd)

space-time integral equations. A major effort was required in order to be able to handle non-rectangular plate geometries. The resulting numerical procedure consisted of a set of local coordinate transformations in the plate edge regions in order to be able to properly satisfy the boundary conditions on the surface currents. Results were computed for several triangular plates, finned cylinders, and a MIG-21 aircraft model. These results were found to be in good agreement with measurements taken on the Sperry time domain scattering range. In addition measured results were obtained for the response of scattering centers when coated with RAM. These results show that RAM can indeed lower the scattered response but that the amount of reduction is dependent upon the spectrum of the illumination and the aspect angle. Moreover, there were several frequencies where the RCS experienced nulls of an additional 8-10 db.

The outstanding achievement of this work has been the development of general techniques for computing the wideband (or impulse) response of realistic targets with a highly efficient and accurate method of computing the noise-corrupted, pulse-compressed video response of these targets when illuminated by a wideband radar.

*RAM (Radar Absorbing Material).

Radar absorbing
materials

ACCESSION for	
NTIS	White Section <input checked="" type="checkbox"/>
DDC	Buff Section <input type="checkbox"/>
UNANNOUNCED	<input type="checkbox"/>
JUSTIFICATION	
BY	
DISTRIBUTION/AVAILABILITY CODES	
Gr.	SPECIAL
A	

UNCLASSIFIED

SECURITY CLASSIFICATION OF THIS PAGE(When Data Entered)

TABLE OF CONTENTS

<u>Section</u>	<u>Page</u>	
1	INTRODUCTION	1
2	SPACE-TIME INTEGRAL EQUATION SOLUTION FOR REFINED AIRCRAFT MODEL	3
2.1	General Problem	3
2.2	STIE Formulation	5
2.2.1	Incident Field	5
2.2.2	Farfield	8
2.2.3	Surface Equations	9
2.3	Numerical Solution of STIE	12
2.3.1	General	12
2.3.2	Detailed Solution of STIE on Fin	14
2.3.3	Summary of Solution Procedure on Fin	20
2.3.4	Surface Derivatives on Flat Surface	21
2.4	Computational Results	25
2.4.1	Triangle Responses	26
2.4.2	Fins on Cylinder	32
3	STIE CALCULATION OF SCATTERING CENTER RESPONSES	37
3.1	Method	38
3.2	Results	40
3.2.1	Prolate Spheroid	40
3.2.2	Right Circular Cylinder	42
4	TIME DOMAIN MEASUREMENTS	48
4.1	Measurement System	48
4.2	Measured Results	50
5	CALCULATION OF TARGET RESPONSE AS SEEN BY WIDEBAND RADARS	74
5.1	Backscattered Waveform	74
5.2	Coherent Radar Signal Processing	75
5.3	Complex Envelope of the Return Signal	76
5.4	Matched Filtering and Pulse Compression	79
5.5	Scaling Via the Radar Equation	80
5.6	Inclusion of Noise Effects	82
5.7	Example: Idealized Two-Element Target	84
5.8	Example: Right Circular Cylinder	85
6	SUMMARY	90
7	REFERENCES	92

TABLE OF CONTENTS (Contd)

<u>Section</u>		<u>Page</u>
8	APPENDICES	93
8.1	Self-Patch Integration at Edge	93
8.2	Finite Element Technique	97
8.3	First Order Scattering Center Response	102

LIST OF FIGURES

<u>Figure</u>		<u>Page</u>
1	MIG-21	4
2	MIG-21 Model	4
3	Equivalent problem of scattering from surfaces with fins attached	6
4	Edge geometry	19
5	Grid choices	22
6	Calculated response of 2 x 2 square plate with hexagonal grid	24
7	Smoothed impulse response of 4 x 4 (45°) triangle at 0, 45°, 90°	27
8	Smoothed impulse response of 4 x 4 (45°) triangle at 90°, 135°, 180°	28
9	Smoothed impulse response of 4 x 6.28 (30°) triangle at 0, 45°, 90°	29
10	Smoothed impulse response of 4 x 6.28 (30°) triangle at 90°, 135°, 180°	30
11	Small fin variations - calculated responses, $\alpha = 90^\circ$	31
12	Effect of small fin on cylinder response, $\alpha = 90^\circ$	33
13	Effect of large fin on cylinder response, $\alpha = 90^\circ$	34
14	Calculated MIG-21 response, $\alpha = 90^\circ$	36
15	Scattering center response calculation relationships	39
16	Typical prolate spheroid scattering center response (TM, $\alpha = 60^\circ$)	41
17	RCC scattering center responses -- end-on and broadside	44
18	RCC scattering center responses -- intermediate angles	47
19	Incident pulse (hor. scale: 0.5 ns/div.; vert. scale: 100 mV/div.)	51
20	Spectrum of incident pulse	52
21	MIG-21 models on a mirror plane	56

LIST OF FIGURES (contd)

<u>Figure</u>		<u>Page</u>
22	MIG-21 models on the scattering range	57
23	Target geometry of triangular plates	58
24	Target geometry of large triangular plate and large cylinder models	59
25	Smoothed impulse response of Reveille MIG-21 model (hor. scale: 0.5 ns/div.; vert. scale: 5 mV/div.)	60
26	Smoothed impulse response of machined MIG-21 model (hor. scale: 0.5 ns/div.; vert. scale: 5 mV/div.)	62
27	Smoothed impulse response of 30° triangle (hor. scale: 0.5 ns/div.; vert. scale: 5 mV/div.)	63
28	Smoothed impulse response of 45° triangle (hor. scale: 0.5 ns/div.; vert. scale: 5 mV/div.)	65
29	Smoothed impulse response of 60° triangle (hor. scale: 0.5 ns/div.; vert. scale: 5 mV/div.)	66
30	Smoothed impulse response of scattering centers (hor. scale: 0.5 ns/div.; vert. scale: 5 mV/div.)	68
31	Smoothed impulse response of large 30° triangle (hor. scale: 0.5 ns/div.; vert. scale: 5 mV/div.)	69
32	Radar Cross Section (RCS) of large 30° triangle with and without RAM	70
33	Smoothed impulse response of large circular cylinder (hor. scale: 0.5 ns/div.; vert. scale: 5 mV/div.)	72
34	Radar Cross Section of large cylinder with and without RAM	73
35	Radar receiver processing for p and q (or complex envelope) generation	77
36	Pulse compression by complex video matched filtering	81
37	Block diagram of radar system operation	81
38	ALCOR linear video ($\sqrt{\text{RCS}}$) return from two element target	86
39	ALCOR video return from a cylinder (Average S/N = 80 dB)	87
40	ALCOR video return from a cylinder (Average S/N = 20 dB)	89
41	Edge Integration	94

EVALUATION

Sperry Research Center was successful in obtaining the smooth impulse response for aircraft like targets. This result has application for computing the backscatter or bistatic response for any type aircraft at any aspect angle. The advantage of this solution is that the response is over the whole radar spectrum. One can readily compute what the response is for any radar transmitted waveform. Therefore, these results have application over all types of radars and can be used for system evaluation. Evaluation of applying radar absorbing material has shown that 8-10 db reductions can be accomplished over certain frequencies. This technique allows the design engineer the opportunity to choose the best frequencies for detection or reduction. The success of this program has added to the Air Force goal for computing the response of complex targets at all frequencies to use in radar system development, as outlined in RADC TPO 2E.

Daniel L. Tauroney

DANIEL L. TAURONEY
Project Engineer

SECTION 1
INTRODUCTION

This document is submitted as the final report in response to the requirements set forth in Contract No. F30602-77-C-0166 between the Sperry Corporate Research Center (SCRC), Sudbury, Massachusetts, and the Air Force Systems Command, Rome Air Development Center (RADC), Griffiss Air Force Base, New York. The general objective of this program is to develop techniques for predicting the radar response of airborne targets.

Predicting the wideband response of targets for a particular radar involves two fundamental steps. The first is to calculate, from the given structural geometry of the target, the target impulse response or, equivalently, the target frequency response at all frequencies. This impulse response is the fundamental electromagnetic characterization of the target. It is the knowledge of this impulse response that enables the response for any incident waveform to be simply calculated. The second step in predicting the radar response is to apply standard linear systems theory to develop a wideband, coherent, radar range equation which includes the effects of sky and receiver noise.

In this effort the techniques for calculating the smoothed impulse response from triangular fins, quadrilateral fins and from more realistic aircraft models have been developed and are described in Section 2. The responses are computed by the direct time domain solution of the space-time integral equation. Results obtained for fins and a MIG-21 model using this technique were verified with direct time domain measurements and are discussed in Section 2.

At high frequencies when the characteristic target dimensions are many wavelengths, the target scattering model can be reduced to a set of returns from scattering centers on the target. These scattering

center returns are due to regions of the target where the surface derivatives are discontinuous and yield a singularity in the impulse response of the target. Since these returns result from local regions in space-time, time domain techniques provide the natural way to solve for them. In Section 3 time domain techniques are developed to calculate the impulse response of these scattering centers. Again the space-time integral equation approach provides a very efficient and accurate technique for these calculations. Results are presented for the prolate spheroid, right circular cylinder and flat plate triangles as a function of aspect angle. For scattering centers separated by several wavelengths the total response is then a superposition (in the time domain) of individual responses.

The time domain measurement facility is described in Section 4 and smoothed impulse response results are displayed for triangular fins and MIG-21 models. Measurements of the scattering center responses of a large triangular fin and a large circular cylinder are also presented. These scattering center responses were measured for both conducting targets and radar absorbing material coated target.

A computer method is developed in Section 5 for calculating the broadband radar response from the target impulse response. This method is both highly efficient and accurate and provides the noise-computed, pulse-compressed video response of these targets when illuminated by a wideband radar. A model of the ALCOR radar is used to demonstrate these techniques.

SECTION 2

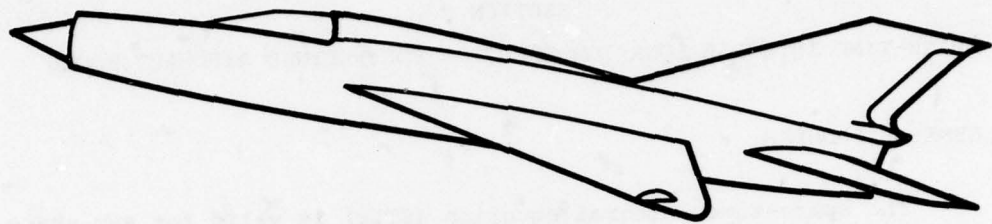
SPACE-TIME INTEGRAL EQUATION SOLUTION FOR REFINED AIRCRAFT MODEL

2.1 GENERAL PROBLEM

The space-time integral equation (STIE) is valid for any shape of conducting target. Solution techniques have been developed for a number of important classes, such as capped and flat-end cylinders, prolate spheroids, wires, flat plates, and others [1-4]. In Ref. 1, the response of a simple aircraft model with rectangular wings was computed. In the present effort, the aim was to treat a more realistic aircraft model: the aircraft chosen for analysis was a MIG-21, illustrated in Fig. 1. The model for calculation purposes, illustrated in Fig. 2, consists of quadrilateral wings (basically triangular) on a thin cylindrical fuselage. Central to this problem is the solution of the STIE on triangular and general quadrilateral plates. The solution to this problem and the extension to plates on a cylinder is presented in this section. Comparison with measurements are also made in this section.

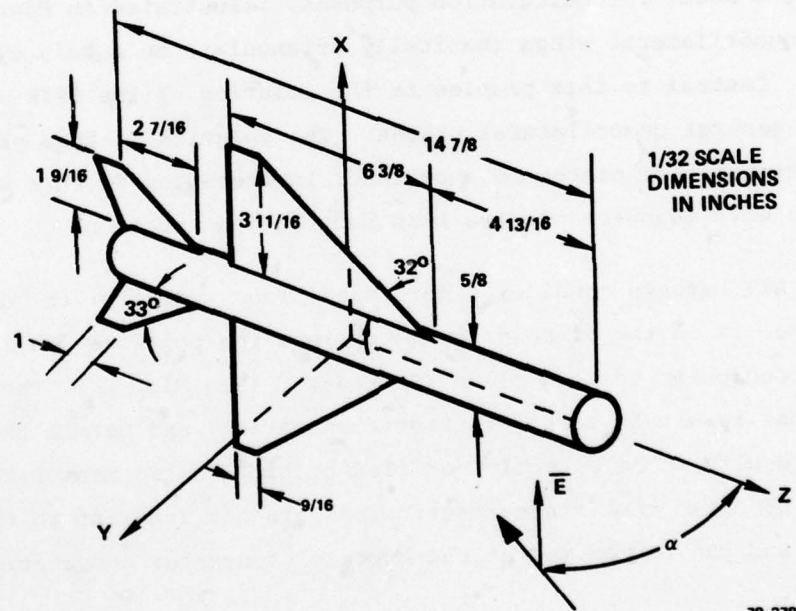
All targets considered here have plane symmetry; the direction of incidence is in the plane of symmetry; and the polarization is taken to be perpendicular to this plane (TE mode). (See Fig. 2.) These restrictions result in more efficient computation, and permit the computational results to be directly verified by time domain measurements. It should be noted that these restrictions are not inherent to the STIE technique and can be removed at the expense of greater computational complexity.

The incident field is taken as a smoothed impulse, which yields a response valid from DC to well into the resonance region. The techniques of Section 3 (direct computation of scattering center responses) coupled with the high-frequency-augmentation technique described in



78-277

FIG. 1 MIG-21.



78-278

FIG. 2 MIG-21 model.

Ref. 5 can then be used to obtain the impulse response, or equivalently, the frequency response over the entire spectrum.

2.2 STIE FORMULATION

In the STIE approach to the scattering problem, the solution is found directly in the time domain by a procedure of stepping in time. The surface currents induced on the target by the incident field and the mutual interactions of the surface elements are computed first for all time, using a set of integro-differential equations (the STIE), subject to the appropriate boundary conditions. Once the surface currents have been found, the scattered field in any direction can be calculated, using another STIE, by considering the equivalent problem of Fig. 3. In this equivalent statement of the problem, the conducting surface has been replaced by source currents radiating into free space.

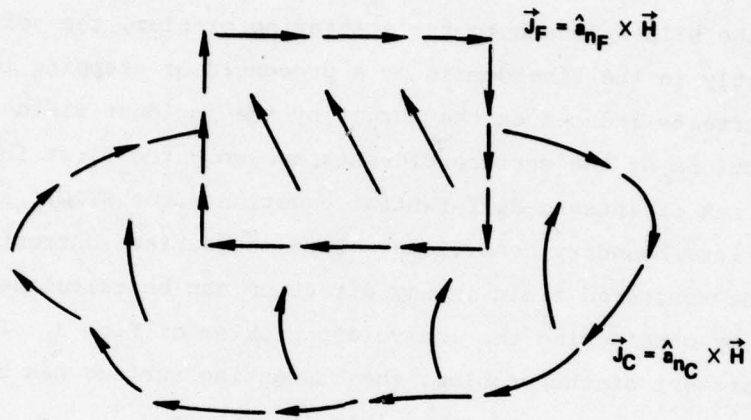
The equations describing the surface solution, contain terms which reflect:

- (a) the direct influence of the incident field,
- (b) the influence of cylinder currents on other cylinder currents,
- (c) the influence of fin currents on other fin currents,
- (d) the influence of cylinder currents on fin currents,
- (e) the influence of fin currents on cylinder currents.

The derivation and solution of these equations has been described in detail in the above references and will therefore be presented here only in outline. The solution to the general quadrilateral plate, not treated elsewhere, will be discussed in greater detail.

2.2.1 Incident Field

Ideally, one would choose an impulse as the time domain incident field, since a simple convolution of the impulse response with an actual incident waveform would yield the actual response. Moreover, the impulse



78-279

FIG. 3 Equivalent problem of scattering from surfaces with fins attached.

response is intimately related to the actual geometry of the target, suggesting the possibility for techniques that determine the impulse response by inspection of geometry.

For the numerical solution, however, it is not practical to use an ideal impulse for excitation. Instead a regularized or smoothed impulse is used. The form of this illumination at the origin is the Gaussian regularization of an impulse, namely

$$H^i(t) = \frac{n}{\sqrt{\pi}} e^{-n^2 t^2} \quad (1)$$

which has unit integral over all time and converges to a delta functional as n goes to infinity. The time domain integral equations can be solved for bodies with linear dimensions up to several pulselwidths of this smoothed impulse. In this solution consideration is limited to bodies of this size.

The vector \vec{H}^i is assumed to lie in the plane of symmetry ($x = 0$). The direction of incidence makes an angle α with the z -axis. (See Fig. 2.)

Let \hat{r}_o be the unit vector pointing to the source, and β the angle of \vec{E}^i with respect to the x -axis. Then

$$\epsilon \vec{E}^i = \frac{1}{c} \hat{r}_o \times \vec{H}^i$$

For time in units of light meters and for the geometry of Fig. 2, in cartesian coordinates at the point \vec{r} :

$$\rho \equiv \vec{r} \cdot \hat{r}_o$$

$$\hat{r}_o = (0, \sin \alpha, \cos \alpha)$$

calculated to produce the following solution in rectangular coordinates

$$\vec{H}(\vec{r}, t) = \left\{ \frac{n}{\sqrt{\pi}} e^{-n^2(t+\rho)^2} \right\} (\sin \beta, -\cos \alpha \cos \beta, \sin \alpha \cos \beta) \quad (2)$$

$$\epsilon \frac{\partial \vec{E}}{\partial t}(\vec{r}, t) = -n^2(t+\rho) \left\{ \frac{n}{\sqrt{\pi}} e^{-n^2(t+\rho)^2} \right\} (\cos \beta, \cos \alpha \sin \beta, -\sin \alpha \sin \beta).$$

2.2.2 Farfield

An integral equation for the scattered field may be obtained by considering the equivalent problem of Fig. 3, in which the scatterer has been replaced by source currents \vec{J} which are equal to

$$\vec{J} = \hat{a}_n \times \vec{H},$$

by virtue of the conducting surface boundary condition. Using the free space Green's function, the solution to the EM wave equation then becomes

$$\vec{H}(\vec{r}, t) = \vec{H}^i(\vec{r}, t) + \frac{1}{4\pi} \int_S \left\{ \left[\frac{1}{R^2} + \frac{1}{RC} \frac{\partial}{\partial \tau} \right] \vec{J}(\vec{r}', \tau) \times \hat{a}_R \right\} dS' \quad (3)$$

where

τ = the retarded time $t - R/c$

\vec{r} = position vector to the observation point

\vec{r}' = position vector to the integration point

$$R = |\vec{r} - \vec{r}'|$$

$$\hat{a}_R = \frac{\vec{r} - \vec{r}'}{R}$$

c = speed of light

and no currents in \hat{a}_n = normal to the surface. at no time and

Imperial and naval to sonic velocity and current in the body

In most applications, the quantity of interest is the far scattered field. In the limit that $|\vec{r}|$ becomes large the first term in the integral becomes negligible,

$$\hat{a}_R \rightarrow \hat{a}_r$$

$$\frac{1}{R} \rightarrow \frac{1}{r}$$

We can thus write

$$\vec{r} \vec{H}^s(\vec{r}, t) = \frac{1}{4\pi} \int_S \frac{\partial \vec{J}(\vec{r}', \tau)}{\partial \tau} \times \hat{a}_r dS' \quad (4)$$
$$\tau = t - R$$

with time expressed in light meters.

2.2.3 Surface Equations

To obtain the integral equation for currents on the surface of a conducting body with finite thickness, we can start from equation (3). The boundary conditions are that

$$\vec{J} = \hat{a}_n \times \vec{H}$$

and that the electromagnetic field is zero inside the body. Moving the observation point \vec{r} to the surface of the conductor, applying a limiting procedure, we obtain

$$\vec{J}(\vec{r}, t) = 2\hat{a}_n \times \vec{H}^i(\vec{r}, t) + \frac{1}{2\pi} \int_S \hat{a}_n \times \left\{ \left[\frac{1}{R^2} + \frac{1}{R} \frac{\partial}{\partial \tau} \right] \vec{J}(\vec{r}', \tau) \times \hat{a}_R \right\} dS' \quad (5)$$
$$\tau = t - R$$

with time expressed in light meters.

This equation is used to solve for the surface current on the thick part of the target, i.e. the cylinder. Since \vec{J} under the integral is evaluated at the retarded time, τ , this equation can be solved numerically by stepping in time. Note that the integral is over the entire surface and thus contains contributions from the fins as well as from the rest of the cylinder. This formulation does not apply to open thin surfaces, since the boundary condition that $\vec{H} = 0$ on the other side of the surface is not satisfied.

A thin surface is one in which \vec{E} and \vec{H} do not vary across its thickness. In our equivalent problem of Fig. 3, the thin surface is thus replaced by a current sheet. The boundary condition for a conducting surface is that the tangential component of the total \vec{E} is zero, hence

$$\vec{E}_{\tan} = [\vec{E}^s + \vec{E}^i]_{\tan} = 0 \quad \text{on the surface} \quad (6)$$

The total electric field in space can be written in terms of the magnetic and electric potentials (\vec{A} and ϕ):

$$\vec{E}(\vec{r}, t) = \vec{E}^i(\vec{r}, t) - \mu \frac{\partial \vec{A}(\vec{r}, t)}{\partial t} - \nabla \phi(\vec{r}, t), \quad (7)$$

where, if \vec{A} and ϕ are related by the Lorentz gauge:

$$\nabla \cdot \vec{A} + \epsilon \frac{\partial \phi}{\partial t} = 0 \quad (8)$$

then

$$\vec{A}(\vec{r}, t) = \frac{1}{4\pi} \int_S \left\{ \frac{\vec{J}(\vec{r}', \tau)}{R} \right\} d\vec{s}' \quad (9)$$

$\tau = t - R$

Equations (7) and (8) combined with the surface boundary condition (6) yields

$$\left[\nabla \left(\nabla \cdot \vec{A}(\vec{r}, t) \right) - \frac{\partial^2 \vec{A}(\vec{r}, t)}{\partial t^2} \right]_{\tan} = - \left[\epsilon \frac{\partial \vec{E}^i(\vec{r}, t)}{\partial t} \right]_{\tan} \quad (10)$$

where \tan denotes the tangential component.

Replacing \vec{A} by equation (9) results in a first kind integro-differential equation, where the unknown \vec{J} appears only under the integral sign. Again, note that the (retarded) integral is over the entire surface and represents the influence of cylinder as well as fin currents.

Equation (10) is to be solved subject to the fin edge conditions. These conditions are known for \vec{J} at edge point \vec{r}_e :

$$J_{\perp}(\vec{r}_e, t) = 0 \quad , \quad J_{\parallel}(\vec{r}_e, t) \propto \sqrt{\frac{1}{d}} \quad (\text{free-space edge}) \quad (11)$$

$$\frac{\partial J_{\perp}}{\partial n}(\vec{r}_e, t) = 0 \quad , \quad J_{\parallel}(\vec{r}_e, t) = 0 \quad (\text{fin-cylinder join}),$$

where

d is the perpendicular distance from the edge

\perp and \parallel refer to the perpendicular and parallel components of J .

The join edge conditions also hold at the symmetry plane, for the case of a fin by itself.

Unlike the second kind integral equation for the cylinder body (equation 5), equation (10) requires the evaluation of second order space derivatives. It is this aspect that makes this equation more difficult to solve numerically.

2.3 NUMERICAL SOLUTION OF STIE

2.3.1 General

The space-time integral equations (5) for the cylinder and (9) and (10) for the fins are solved numerically by representing the surfaces as approximately equal patches. The current is assumed to be constant over a patch at a particular time, except for edge patches where the analytic variation is known. The centers of patches are called "nodes". The distance factor R is also assumed to be constant over the integration patch, except for the "self-patch" which contains the observation node \vec{r}_i .

Consider first equation (9) on the fin. We separate "self" and "non-self" contributions to the integral, obtaining:

$$\vec{A}(\vec{r}_i, t) = \gamma_i \vec{J}(\vec{r}_i, t) + \vec{A}_{NS}(\vec{r}_i, t) , \quad (12)$$

where

$$\vec{A}_{NS}(\vec{r}_i, t) = \frac{1}{4\pi} \sum_{j \neq i} \frac{\vec{J}(\vec{r}_j, t)}{R_{ij}} \Delta S_j \quad (13)$$

The proportionality factor γ_i is obtained by analytic integration over the self-patch and is given by

$$\gamma_i = \frac{1}{2} \sqrt{\frac{\Delta S_i}{\pi}} , \text{ a purely geometrical quantity.} \quad (14)$$

Hence we can write the surface current as

$$\vec{J}(\vec{r}_i, t) = \frac{1}{\gamma_i} \left(\vec{A}(\vec{r}_i, t) - \vec{A}_{NS}(\vec{r}_i, t) \right) \quad (15)$$

The term \vec{A}_{NS} is found by the retarded integration of equation (13), while \vec{A} is found by solution of the differential equation (10). This solution

is pursued further in the next subsection.

To write equation (5) for a cylinder node numerically, we proceed similarly by separating out the self-term, obtaining

$$\vec{J}(\vec{r}_i, t) = 2\hat{a}_{ni} \times \vec{H}^i(\vec{r}_i, t) + \left[\left[\zeta_i \vec{J}(\vec{r}_i, t) \right] \right] + \vec{I}_{NS}(\vec{r}_i, t) \quad (16)$$

where

$$\vec{I}_{NS}(\vec{r}_i, t) = \frac{1}{2\pi} \sum_{j \neq i} \hat{a}_{nj} \times \left\{ \left[\frac{1}{R_{ij}^2} + \frac{1}{R_{ij}} \frac{\partial}{\partial \tau} \right] \vec{J}(\vec{r}_j, \tau) \times \hat{a}_{ij} \right\} \Delta s_j \quad (17)$$

The meaning of the term $\left[\left[\zeta_i J_i \right] \right]$ is as follows: Let \hat{a}_u, \hat{a}_v be the directions of principal curvature on the surface with curvatures K_u, K_v . Then

$$\left[\left[\zeta_i J_i \right] \right] \equiv \zeta_i \left(\hat{a}_u \vec{J}_u(\vec{r}_i, t) - \hat{a}_v \vec{J}_v(\vec{r}_i, t) \right) \quad (18)$$

where

$$\zeta_i = \frac{1}{2} \sqrt{\frac{\Delta s_i}{\pi}} \left(\frac{K_u - K_v}{2} \right)_i \quad (19)$$

This is derived in detail in an appendix to Ref. 1. We can thus solve for \vec{J} in terms of its components

$$J_u(\vec{r}_i, t) = \left(\frac{1}{1 - \zeta} \right) \left\{ I_{NSu}(\vec{r}_i, t) + 2 \left(\hat{a}_{ni} \vec{H}^i(\vec{r}_i, t) \hat{a}_u \right) \right\} \quad (20)$$

$$J_v(\vec{r}_i, t) = \left(\frac{1}{1 + \zeta} \right) \left\{ I_{NSv}(\vec{r}_i, t) + 2 \left(\hat{a}_{ni} \vec{H}^i(\vec{r}_i, t) \hat{a}_v \right) \right\} .$$

The current at a cylinder node is thus given directly by the retarded integration over the surface and the incident field.

Coordinate transformations are necessary to evaluate (20): from the Cartesian system in which the \vec{J} are stored to the local u, v system, and back again. (Alternatively, \vec{J} could be stored in the u, v system, but then coordinate transformations are required to evaluate I_{NS} .)

\vec{J} and \vec{A} are computed at discrete time points, separated by Δt . To evaluate $\vec{J}(\tau)$ and its first time derivative, an interpolation is performed on the five points in time nearest τ . These points are smoothed linearly and a quadratic is fit through the resulting three points. The process of smoothing reduces the problem of numerical instabilities in the solution.

2.3.2 Detailed Solution of STIE on Fin

We now discuss in greater detail the solution of equations (9), (10) on the flat plate, subject to the edge conditions (11). In our geometry, the flat fin is located in the plane $y = 0$ (see Fig. 2). Then expanding equation (10) into components

$$\frac{\partial^2 A_x}{\partial t^2} = \frac{\partial^2 A_x}{\partial x^2} + \frac{\partial^2 A_x}{\partial x \partial z} + \frac{\partial^2 A_x}{\partial x \partial y} + \epsilon \frac{\partial E_x^i}{\partial t} \quad (21)$$

$$\frac{\partial^2 A_z}{\partial t^2} = \frac{\partial^2 A_z}{\partial z^2} + \frac{\partial^2 A_z}{\partial z \partial x} + \frac{\partial^2 A_z}{\partial z \partial y} + \epsilon \frac{\partial E_z^i}{\partial t}$$

Using a finite difference approach, these equations are solved by forming the numerical space derivatives of $\vec{A}(r_i, t)$ based on the values of \vec{A} at surrounding nodes. Representing the time derivative also in the finite difference formulation

$$\frac{\partial^2 A}{\partial t^2}(t) = \frac{A(t + \Delta t) - 2A(t) + A(t - \Delta t)}{(\Delta t)^2} \quad (22)$$

we can thus solve for $\vec{A}(t + \Delta t)$, based on the values of \vec{A} at (t) and $(t - \Delta t)$, on the numerical space derivatives of \vec{A} at (t) , and on the incident field: e.g. for the x -component

$$A_x(t + \Delta t) = 2A_x(t) - A_x(t - \Delta t) + (\Delta t)^2 \left\{ \frac{\partial^2 A_x(t)}{\partial x^2} + \frac{\partial^2 A_z(t)}{\partial x \partial z} + \frac{\partial^2 A_y(t)}{\partial x \partial y} + \epsilon \frac{\partial E_x^i(t)}{\partial t} \right\} \quad (23)$$

all evaluated at the nodes \vec{r}_i on the fin. Two problems present themselves:

1. How to form the space derivatives, so that a stable solution results;
2. The numerical differentiation is invalid at and near the edges, where the edge conditions have to be invoked to derive a value for \vec{A} .

The edge conditions, however, are known for \vec{J} and not for \vec{A} . On the other hand, \vec{A} is bounded at the edge, as will be shown, so that \vec{A} may be obtained directly by integration of equation (9), making use of the known variation of \vec{J} .

Again we separate the self-patch from the integration:

$$\vec{A}(\vec{r}_e, t) = \vec{A}_{NS}(\vec{r}_e, t) + \vec{A}_S(\vec{r}_e, t), \quad (24)$$

where \vec{A}_{NS} , given by equation (13) contains the contribution from all patches (including the cylinder and other fins), except the self-edge patch at \vec{r}_e , and \vec{A}_S is the integral over the self patch:

$$\vec{A}_S(\vec{r}_e, t) = \frac{1}{4\pi} \int_{S_e} \frac{\vec{J}(\vec{r}', t) d\vec{s}'}{R}$$

The details of this last integration are left for Appendix 8.1. The result is that

$$A_{S\parallel}(\vec{r}_e, t) = \gamma_{\parallel} J_{\parallel}^{\text{eff}}(\vec{r}_e, t) \quad (25)$$

$$A_{S\perp}(\vec{r}_e, t) = \gamma_{\perp} J_{\perp}^{\text{eff}}(\vec{r}_e, t)$$

where \parallel and \perp refer to the parallel and perpendicular components. The proportionality constants γ_{\parallel} , γ_{\perp} are purely geometrical, but reflect the variation of \vec{J} (equation 11) over the patch.

$$\gamma_{\parallel} = \frac{3}{8} \sqrt{\frac{2\Delta S_e}{\pi}} \quad , \quad \gamma_{\perp} = \frac{3}{16} \sqrt{\frac{2\Delta S_e}{\pi}} \quad \text{at a free edge;}$$

$$\gamma_{\parallel} = 0 \quad , \quad \gamma_{\perp} = \frac{1}{4} \sqrt{\frac{2\Delta S_e}{\pi}} \quad \text{at a bound or symmetry edge;}$$

$$\gamma_{\parallel} = \gamma_{\perp} \approx \frac{5}{48} \sqrt{\frac{4\Delta S_e}{\pi}} \quad \text{at a free corner;}$$

$$\gamma_{\parallel} = 0 \quad , \quad \gamma_{\perp} = \frac{3}{8} \sqrt{\frac{4\Delta S_e}{\pi}} \quad \text{at a bound corner.}$$

(The directions \parallel , \perp of the bound corner are defined to be those of the bound edge attached to it.) The free corner constants are derived from the assumption that $\vec{J} \rightarrow \vec{0}$ at the corner, and that the corner is about 90° . A more obtuse corner could be treated as an edge. The bound corner constants are obtained from the observation that one edge is bound and the other free. (Confusion is avoided, when it is noted that for all these constants γ as well as for (19) and (14), the quantity under $\sqrt{}$ represents ρ or the radius of a circular patch with the area ΔS_e .) If M is the transformation from Cartesian to the edge (\parallel, \perp) coordinate system,

$$\begin{bmatrix} J_{\parallel} \\ J_{\perp} \end{bmatrix} = M \begin{bmatrix} J_z \\ J_x \end{bmatrix}$$

then

$$\vec{A}_S(\vec{r}_e, t) = [\gamma] \vec{J}^{\text{eff}}(\vec{r}_e, t) \quad (27)$$

where

$$[\gamma] = M^{-1} \begin{bmatrix} \gamma_0 & 0 \\ 0 & \gamma_1 \end{bmatrix} M.$$

This value of \vec{A}_S can then be used in (24) to obtain \vec{A} at the edge.

The effective current, J^{eff} , is also found by integration over the edge patch in accordance with the edge conditions (see Appendix 8.1). The result is

$$J_{\parallel}^{\text{eff}} = k_{\parallel} J_{\parallel 0}$$

$$J_{\perp}^{\text{eff}} = k_{\perp} J_{\perp 0},$$

where

$$k_{\parallel} = 2.226 \frac{\sqrt{d}}{(2\Delta S_e/\pi)^{\frac{1}{4}}} \quad , \quad k_{\perp} = .4244 \frac{\sqrt{2\Delta S_e/\pi}}{d} \quad \text{at a free edge};$$

$$k_{\parallel} = 0 \quad , \quad k_{\perp} = 1 \quad \text{at a bound or symmetry edge};$$

$$k_{\parallel} = k_{\perp} = 1.2113 \frac{(4\Delta S_e/\pi)^{\frac{1}{4}}}{\sqrt{d}} \quad \text{at a free corner};$$

$$k_{\parallel} = 0 \quad , \quad k_{\perp} = 2.226 \frac{\sqrt{d}}{(4\Delta S_e/\pi)^{\frac{1}{4}}} \quad \text{at a bound corner}, \quad (29)$$

d is the perpendicular distance from the edge node to the point \vec{r}_o ;

$\vec{J}_o = \vec{J}(\vec{r}_o)$, obtained by interpolating between the two nearest interior nodes:

$$\vec{J}_o = \alpha_1 \vec{J}(\vec{r}_1) + \alpha_2 \vec{J}(\vec{r}_2) . \quad (30)$$

The edge geometry is illustrated in Fig. 4. Again we need to apply the coordinate transformation M , obtaining

$$\vec{J}_{eff}(\vec{r}_e, t) = [\delta] \vec{J}_o(\vec{r}_o, t) , \quad (31)$$

where

$$[\delta] = M^{-1} \begin{bmatrix} k_{\parallel} & 0 \\ 0 & k_{\perp} \end{bmatrix} M .$$

We have thus obtained the effective current at the edges based on interior currents and the edge conditions. These effective values are used in forming the integrals. The values of \vec{A} at the edge are used for evaluating space derivatives of \vec{A} at interior nodes.

Another detail is required for the evaluation of equation (23): Since observation nodes exist only on the fin plane which has $y = 0$, it is not possible to evaluate $\partial^2 A_y / \partial x \partial y$ numerically. Instead we perform $\partial / \partial x$ numerically and obtain $\partial A_y / \partial y$ from the integral equation,

$$\frac{\partial}{\partial y} A_y(\vec{r}, t) = \frac{1}{4\pi} \frac{\partial}{\partial y} \int_S \frac{\vec{J}_y(\vec{r}', \tau)}{R} ds'$$

$$\frac{\partial}{\partial y} A_y(\vec{r}, t) = - \frac{1}{4\pi} \int_S (\hat{R} \cdot \hat{y}) \left(\frac{1}{R^2} + \frac{\partial}{R \partial \tau} \right) J_y(\vec{r}', \tau) ds' \quad (32)$$

Note that nodes on the fin itself do not contribute to this term on account of the factor $(\hat{R} \cdot \hat{y})$, which is zero when observation and source point are both in the $y = 0$ plane.

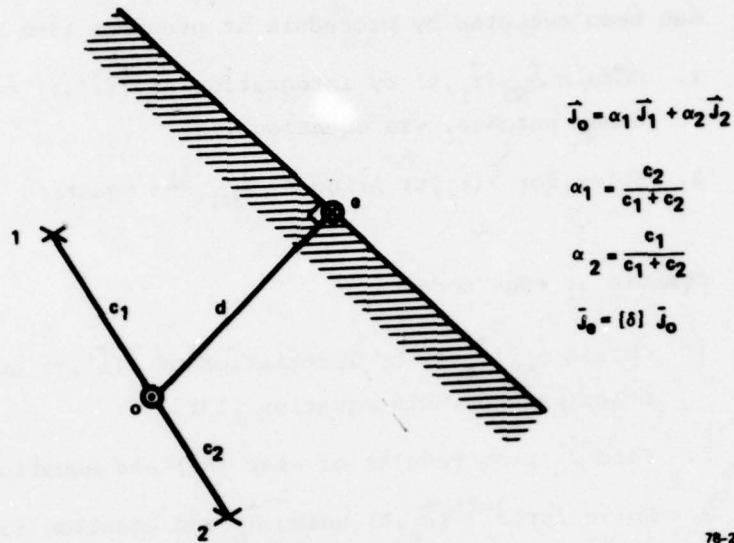


FIG. 4 Edge geometry.

78-280

2.3.3 Summary of Solution Procedure on Fin

We can now summarize the solution procedure. At time t :

A. First compute at interior nodes \vec{r}_i ; assuming that $\vec{A}(\vec{r}_i, t)$ has been computed by procedure at previous time step

1. Obtain $\vec{A}_{NS}(\vec{r}_i, t)$ by integration of $\vec{J}(\vec{r}', t)$ over all other patches, via equation (13)
2. Solve for $\vec{J}(\vec{r}_i, t)$ using \vec{A} , \vec{A}_{NS} and equation (15).

B. Compute at edge nodes \vec{r}_e .

1. Obtain $\vec{A}_{NS}(\vec{r}_e, t)$ by integration of $\vec{J}(\vec{r}', t)$ over all other patches, via equation (13).
2. Find \vec{J}_o from results of step (A2) and equation (30).
3. Solve for $\vec{J}^{eff}(\vec{r}_e, t)$ using \vec{J}_o and equation (31).
4. Solve for $\vec{A}_S(\vec{r}_e, t)$ using \vec{J}^{eff} and equation (27).
5. Solve for $\vec{A}(\vec{r}_e, t)$ using \vec{A}_S , \vec{A}_{NS} and equation (24).

We now have \vec{A} and \vec{J} at all nodes of the fin up to time t .

C. Solve differential equation at interior nodes \vec{r}_i .

1. Evaluate $\partial A_y / \partial y (\vec{r}, t)$ by equation (32).
2. Evaluate space derivatives of $\vec{A}(\vec{r}_i, t)$ using values of \vec{A} at surrounding nodes.
3. Evaluate incident fields at (\vec{r}_i, t)
4. Obtain $\vec{A}(\vec{r}_i, t + \Delta t)$ from equation (23).

We are now ready to repeat the process at the next time step.

Notes:

1. This procedure is performed after calculation of surface currents on cylinder at time t .
2. Interaction of fins and cylinder occurs via integrals (17) and (13) which are over all patches.
3. Computational storage and time is reduced by invoking symmetry: surface currents are not stored or computed at image points (in the present case, points $x < 0$), but their contributions are included in the integrals.

2.3.4 Surface Derivatives on Flat Surface

It remains to discuss the problem of forming the derivatives numerically on the surface of the flat fins. In earlier formulations of the thin plate problem [3], a rectangular grid was used (Fig. 5a). The derivatives were then evaluated by standard finite difference formulas.

For example,

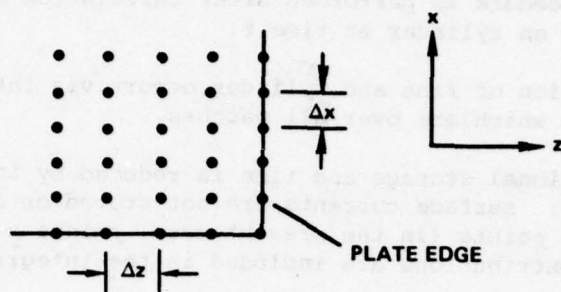
$$\frac{\partial^2 \vec{A}}{\partial x^2}(\vec{r}) = \frac{\vec{A}(\vec{r} + \Delta \vec{x}) + \vec{A}(\vec{r} - \Delta \vec{x}) - 2\vec{A}(\vec{r})}{(\Delta x)^2} \quad (33)$$

This method requires modification when the plate outline is not rectangular and the grid cannot be made to coincide with the plate edges.

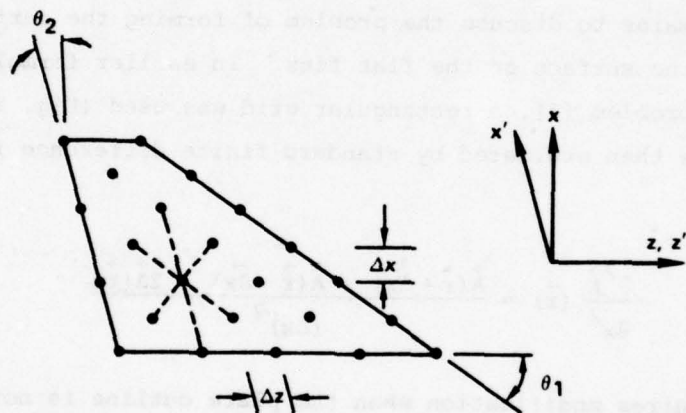
A skew hexagonal grid is illustrated in Fig. 5b. This grid is still regular in the sense that all intervals Δx are equal and all intervals Δz are equal. The angle θ_1 is restricted to $< 45^\circ$ (for larger values of θ_1 , the grid can be rotated by 90°).

A skew coordinate system x' , z' is defined (see Fig. 5b) and the derivatives are found by the chain rule. For example

$$\begin{aligned} \frac{\partial^2 \vec{A}}{\partial x^2}(\vec{r}) &= \frac{\partial^2 \vec{A}}{\partial x'^2} \left(\frac{dx'}{dx} \right)^2 + 2 \frac{\partial^2 \vec{A}}{\partial x' \partial z'} \left(\frac{dx'}{dx} \frac{dz'}{dz} \right) + \frac{\partial^2 \vec{A}}{\partial z'^2} \left(\frac{dz'}{dx} \right)^2 \\ &= \left(\frac{1}{\cos^2 \theta_2} \right) \frac{\partial^2 \vec{A}}{\partial x'^2} + \left(\frac{2 \tan \theta_2}{\cos \theta_2} \right) \frac{\partial^2 \vec{A}}{\partial x' \partial z'} + \left(\tan^2 \theta_2 \right) \frac{\partial^2 \vec{A}}{\partial z'^2} \end{aligned}$$



(a) RECTANGULAR GRID



(b) REGULAR SKEW HEXAGONAL GRID

FIG. 5 Grid choices.

78-281

where

$$\frac{\partial^2 \vec{A}}{\partial x'^2}(\vec{r}) = \frac{\vec{A}(\vec{r} + \Delta \vec{x}') + \vec{A}(\vec{r} - \Delta \vec{x}') - 2\vec{A}(\vec{r})}{(\Delta x')^2},$$

$$\frac{\partial^2 \vec{A}}{\partial z'^2}(\vec{r}) = \frac{\vec{A}(\vec{r} + \Delta \vec{z}') + \vec{A}(\vec{r} - \Delta \vec{z}') - 2\vec{A}(\vec{r})}{(\Delta z')^2}, \text{ etc.}$$

and where

$$\vec{A}(\vec{r} + \Delta \vec{z}') = \frac{1}{2} \vec{A}\left(\vec{r} + \Delta \vec{z}' + \frac{\Delta \vec{x}'}{2}\right) + \frac{1}{2} \vec{A}\left(\vec{r} + \Delta \vec{z}' - \frac{\Delta \vec{x}'}{2}\right)$$

with

$$\Delta z' = \Delta z, \Delta x' = \Delta x / \cos \theta_2$$

Although still not completely general (the outside dimensions have to be commensurate with the Δx and Δz which in turn are related to each other by θ_1 and θ_2), this grid permits a large class of targets to be treated. Most aircraft wings, for example, can be represented closely by this configuration. Variations of the illustrated case are the trapezoid, parallelogram, and triangle. The hexagonal grid concept was tested by comparing the calculation of a square with hexagonal grid with the results for a rectangular grid. The latter had previously been compared with measurement [3]. Although some differences were observed in the intermediate calculation of surface currents, the scattered farfield results were indistinguishable. This response is illustrated in Fig. 6; it is for a 2×2 plate with incident pulse $n = 1$ at normal incidence.

The skew hexagonal grid was used for all the response calculations presented in the next section.

While the regular hexagonal grid was adequate for present purposes, an effort was made to generalize the representation of surface derivatives in order to make the solution procedure truly independent of

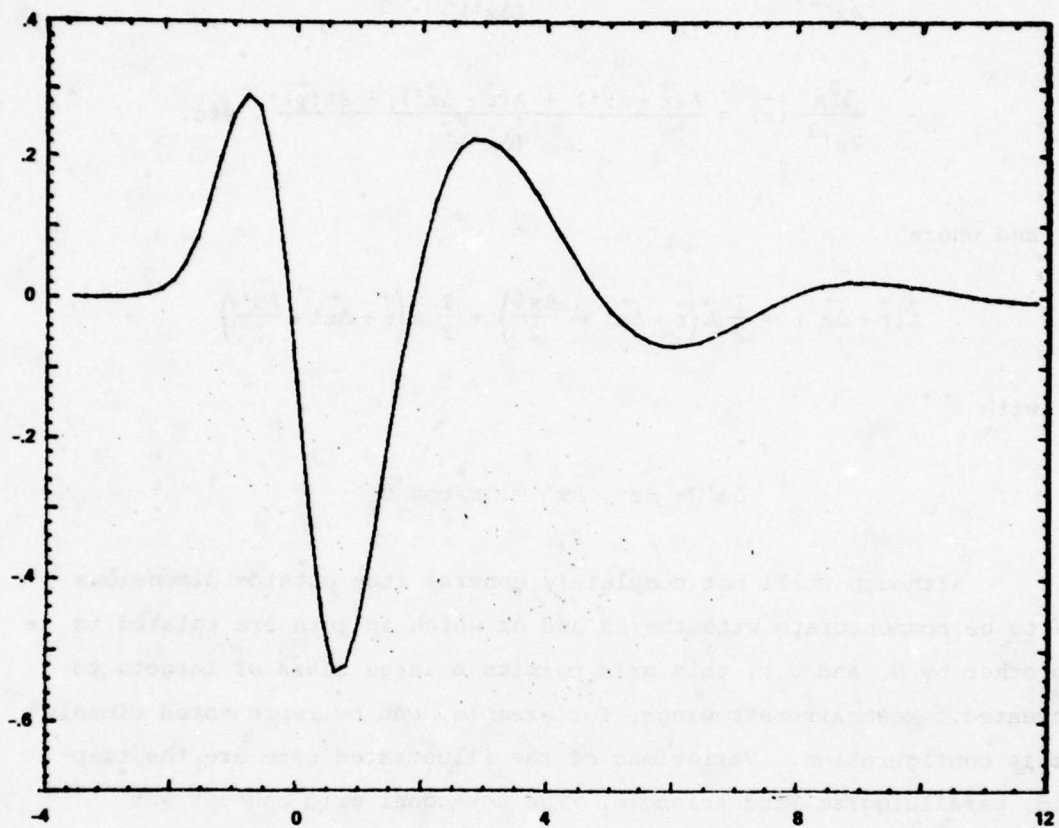


FIG. 6 Calculated response of 2 X 2 square plate with hexagonal grid.

plate geometry. One method was to write a second order Taylor expansion of \vec{A} about the point \vec{r} . The coefficients (i.e., the derivatives at \vec{r}) were then found by a least square fit of this polynomial to the values of \vec{A} at surrounding nodes. Such a procedure would allow an arbitrary arrangement of nodes. Although the derivatives obtained this way had reasonable values, the insertion of this technique in our time-stepping STIE solution caused numerical instabilities which increased in time. Moreover, these instabilities were worst the more asymmetrically the surrounding nodes were placed. Even for a completely regular grid, however, the solution was unstable. The reason for this result is apparently as follows: the fitting procedure assumes constant values of second order derivatives over the entire region of the fit. (In contrast, the simple finite difference method assumes only the constancy of one second derivative along each of the axes of evaluation; e.g. formula 33 assumes only that $\partial^2 A / \partial x^2$ is constant along the x-axis.) For our problem this is a bad approximation, which effectively results in discontinuities in second and first derivatives in going from one patch to an adjacent patch.

A solution to this problem may be a higher order development of \vec{A} so that derivatives can be made continuous across patch boundaries. This is precisely what is done in the procedure for solving differential equations known as the finite element technique. This technique was investigated. It was decided that the complexity of implementation did not warrant its use in the present problem. However, for more general problems, it appears to be the method of choice and it is therefore presented in outline in Appendix 8.2.

2.4 COMPUTATIONAL RESULTS

We have already presented in Fig. 6 the results of plate response calculations for a square plate with a hexagonal grid, which showed good agreement with previous calculations made with a normal finite difference grid. As a further test of the method, calculations were made for 45° and 30° right triangles (standing on an image plane) as a function of incidence angle. Finally, the response of two triangles attached to a

right circular cylinder, representing the model of a MIG-21, was computed. All these calculations were verified by measurement on the time-domain scattering range.

2.4.1 Triangle Responses

The 45° triangle has 4" sides. The 30° triangle has sides of 4" x 6.9282" with the long side on the symmetry plane. Note that the free-space equivalent of this geometry is the triangle augmented by its image.

The response of the 45° triangle is given in Figures 7 and 8 for α at 45° intervals from 0° to 180° . The polarization is TE. The incident smoothed impulse has $n = 0.5$ (/inch); that is, the pulsedwidth, given between 2% points as $W = 4/n$, is 8". The pulsedwidth used in the measurements was slightly shorter than this. The measured response was transformed by a convolution procedure to the same (n) so that direct comparison could be made. The transformed measured responses are superposed in dotted lines on the calculated response curves.

The response of the 30° triangle is given in Figures 9 and 10. Other parameters are the same as for the 45° triangle. These responses are discussed further in Section 4.

In Figure 11 the effect of shape changes is illustrated. Responses are given for variations on the shape of the small fin of the MIG model. All fins have the same area. The fin illustrations are drawn to the same scale as the time axis (ct) of the responses. Also shown to scale is the incident pulse. The effect of the shape change is not pronounced. It is seen that the solution for trapezoidal shape responses have a problem, in that there is residual oscillation. For this reason, the MIG model responses were calculated with triangular wings. The part of the aircraft response due to the large fins should not be affected by this approximation since the wing is very nearly triangular; the part of the response due to the small fin may be affected somewhat (according to Fig. 11), but the magnitude of the small fin response is small in

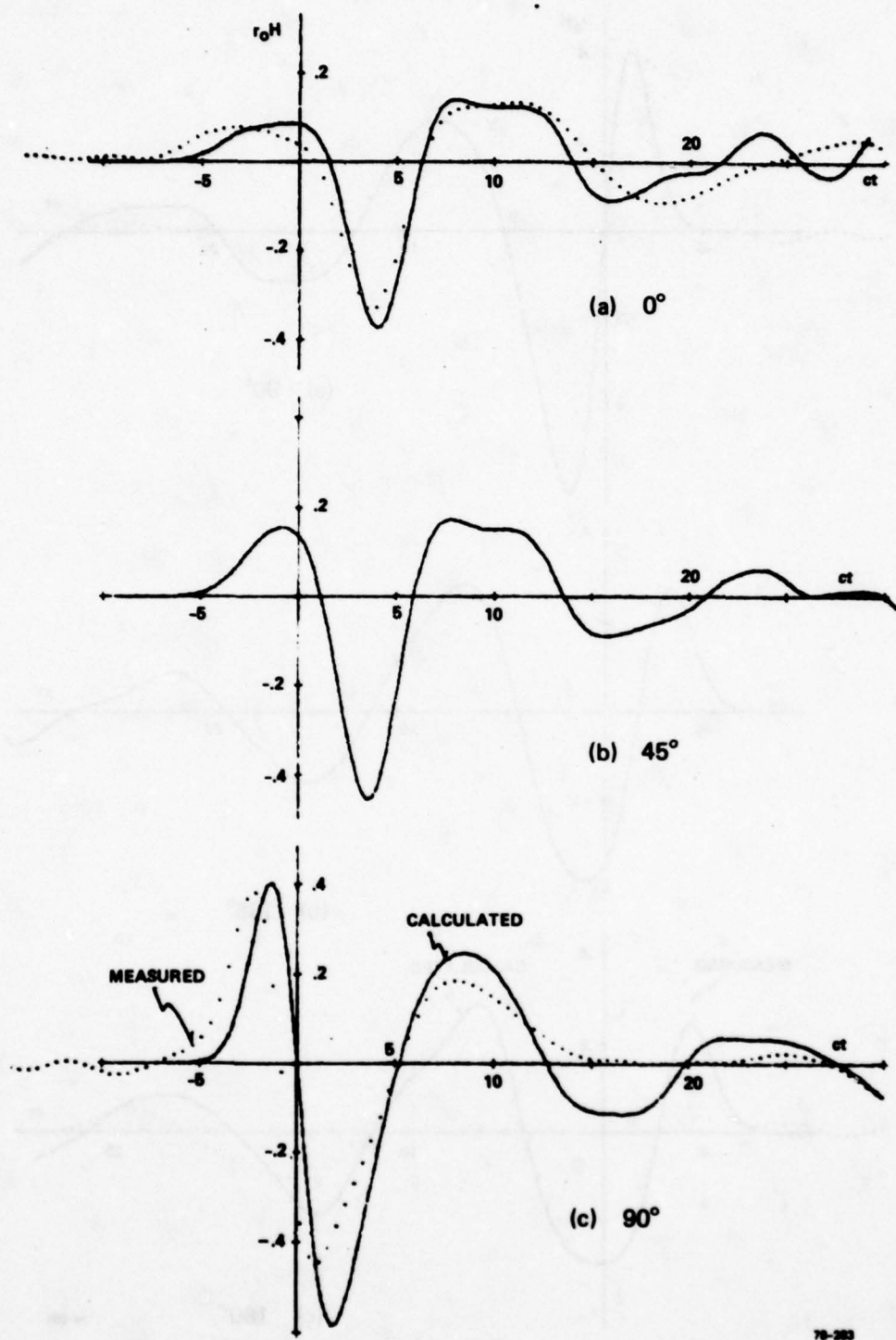


FIG. 7 Smoothed impulse response of 4×4 (45°) triangle at $0, 45^\circ, 90^\circ$.

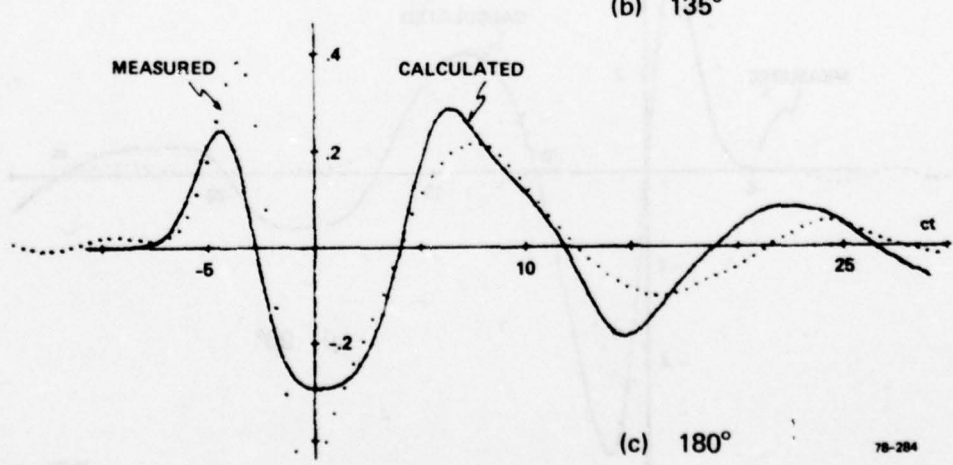
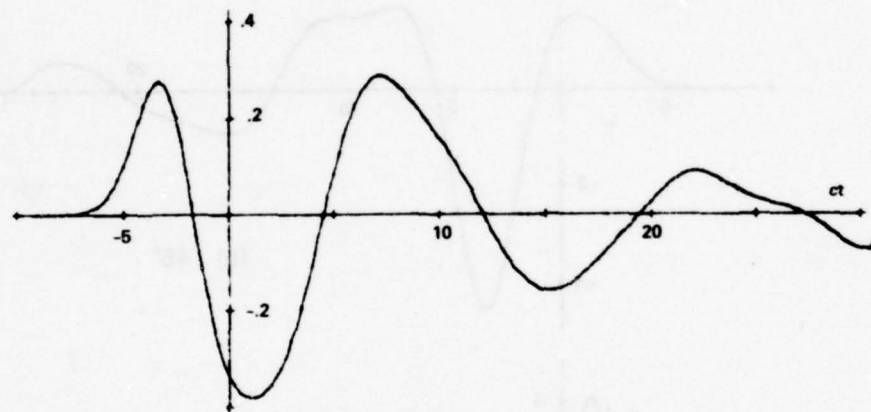
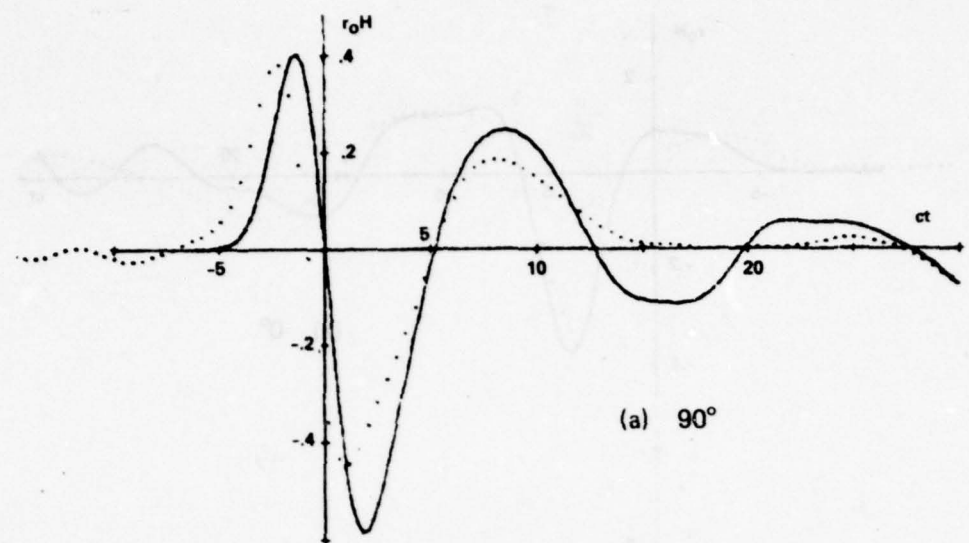


FIG. 8 Smoothed impulse response of 4×4 (45°) triangle at 90° , 135° , 180° .

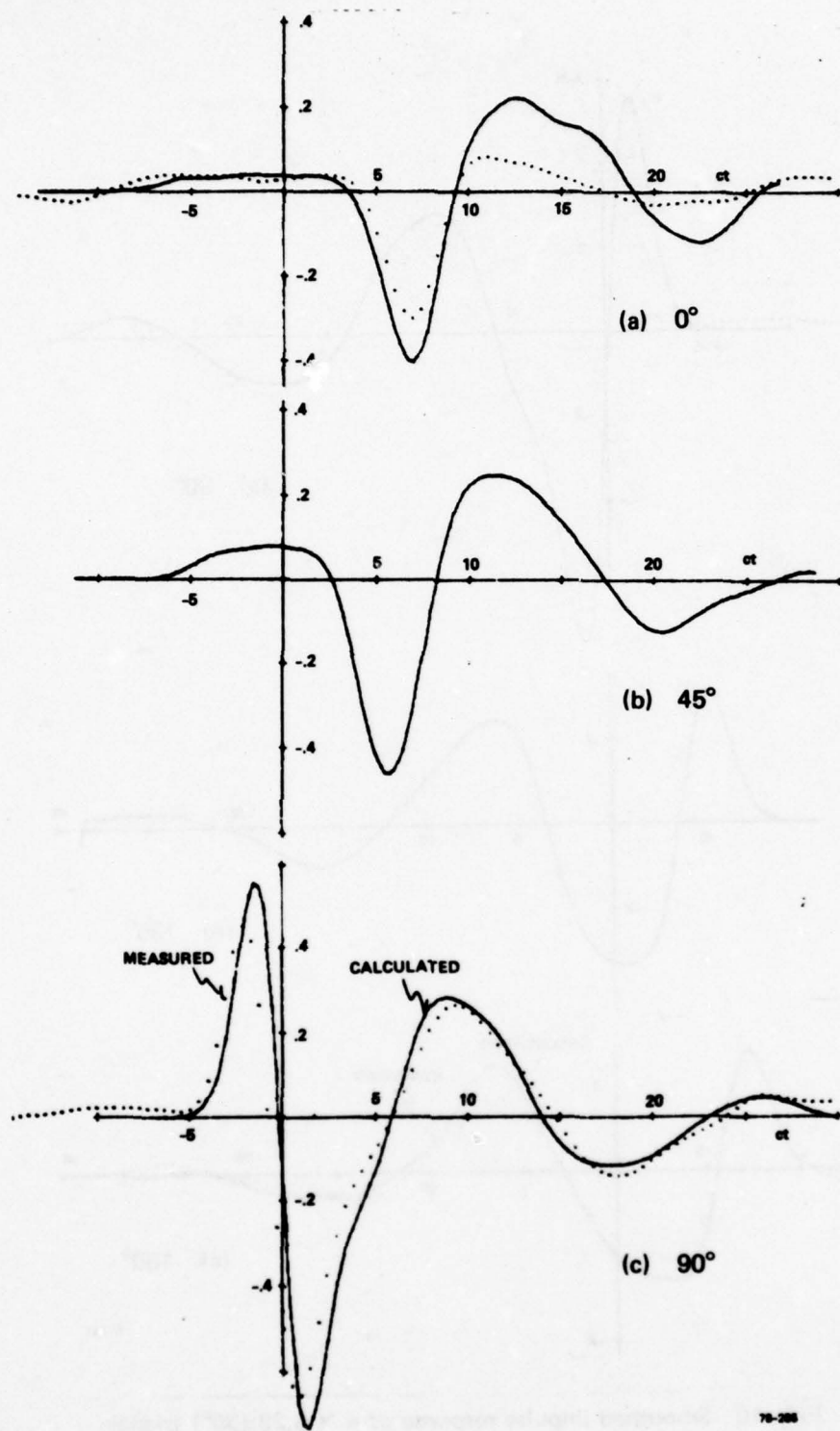


FIG. 9 Smoothed impulse response of 4×6.28 (30°) triangle at $0, 45^\circ, 90^\circ$.

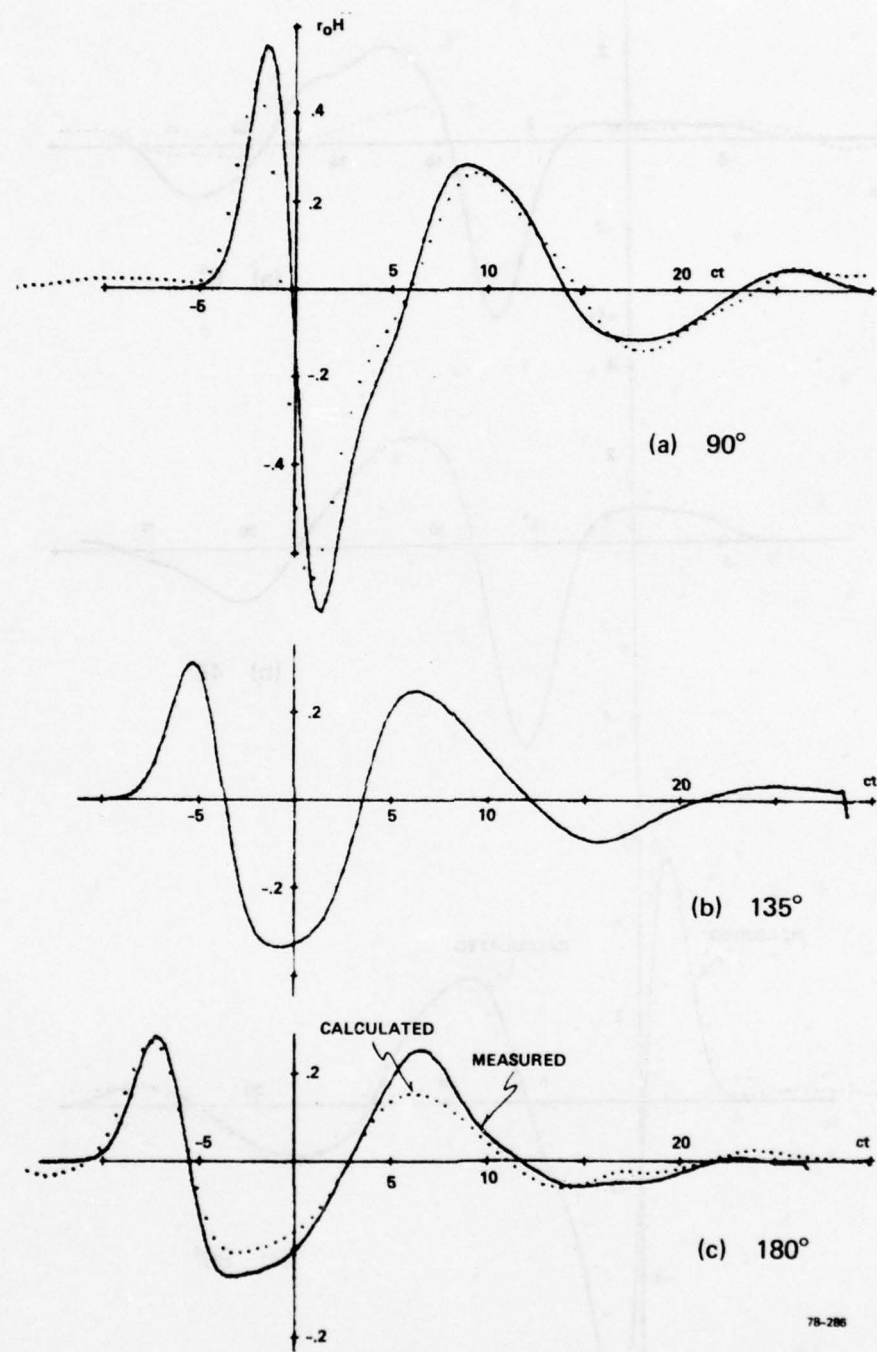
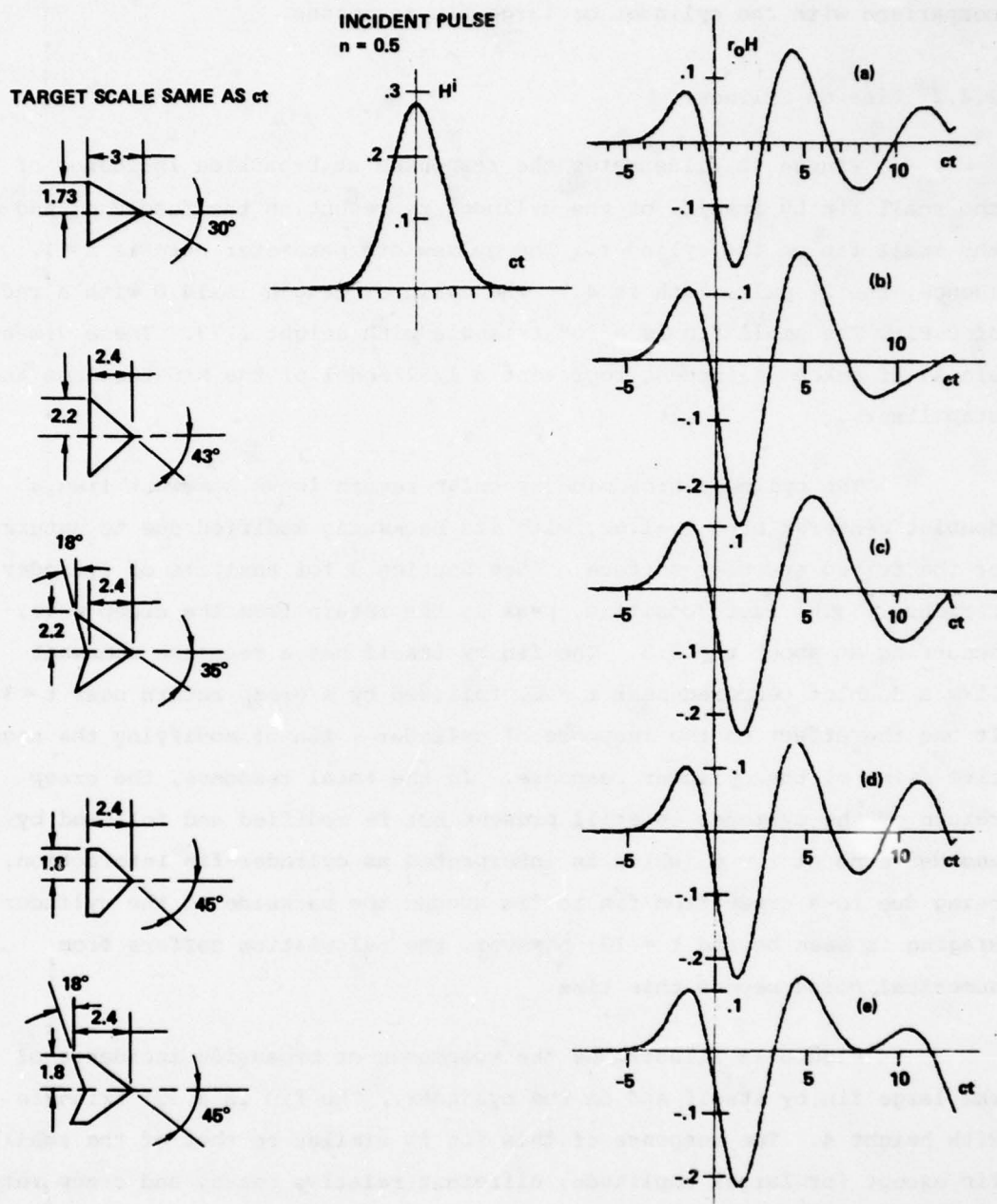


FIG. 10 Smoothed impulse response of 4×6.28 (30°) triangle at 90° , 135° , 180° .



78-267

FIG. 11 Small fin variations - calculated responses, $\alpha = 90^\circ$.

comparison with the cylinder or large fin responses.

2.4.2 Fins on Cylinder

Figure 12 illustrates the responses at broadside incidence of the small fin by itself, of the cylinder representing the fuselage, and of the small fin on the cylinder. The pulsedwidth parameter here is $n = 1$. (Hence, the 2% pulsedwidth is 4.) The cylinder length is 14.8 with a radius of 0.81. The small fin is a 30° triangle with height 1.73. These dimensions, if taken as inches, represent a 1/32 model of the MIG fuselage and stabilizers.

The cylinder broadside specular return looks somewhat like a doublet centered at $t = -1.62$, with its backswing modified due to nature of the curved specular surface. (See Section 3 for analysis of cylinder response.) The last, positive, peak is the return from the creep wave, occurring at about $t = 2.5$. The fin by itself has a response somewhat like a doublet centered near $t = 0$, followed by a creep return near $t = 3$. It has the effect on the response of cylinder + fin of modifying the negative swing of the cylinder response. In the total response, the creep return of the cylinder is still present but is modified and followed by another echo at $t = 6$, which is interpreted as cylinder-fin interaction, being due to a creep from fin to fin around the backside of the cylinder. Ringing is seen beyond $t = 10$; however, the calculation suffers from numerical noise beyond this time.

Figure 13 illustrates the responses at broadside incidence of the large fin by itself and on the cylinder. The fin is a 30° triangle with height 4. The response of this fin is similar to that of the small fin except for larger amplitude, different relative peaks, and creep return time due to the difference in relative length of fin and incident pulse. The magnitude of the fin response is about the same as the specular return of the cylinder and hence causes a large modification around $t = 0$ of the cylinder response when the fin is added to the cylinder. The creep response of the cylinder is still evident near $t = 3$, and is followed by fin-cylinder

TARGET SCALE SAME AS ct

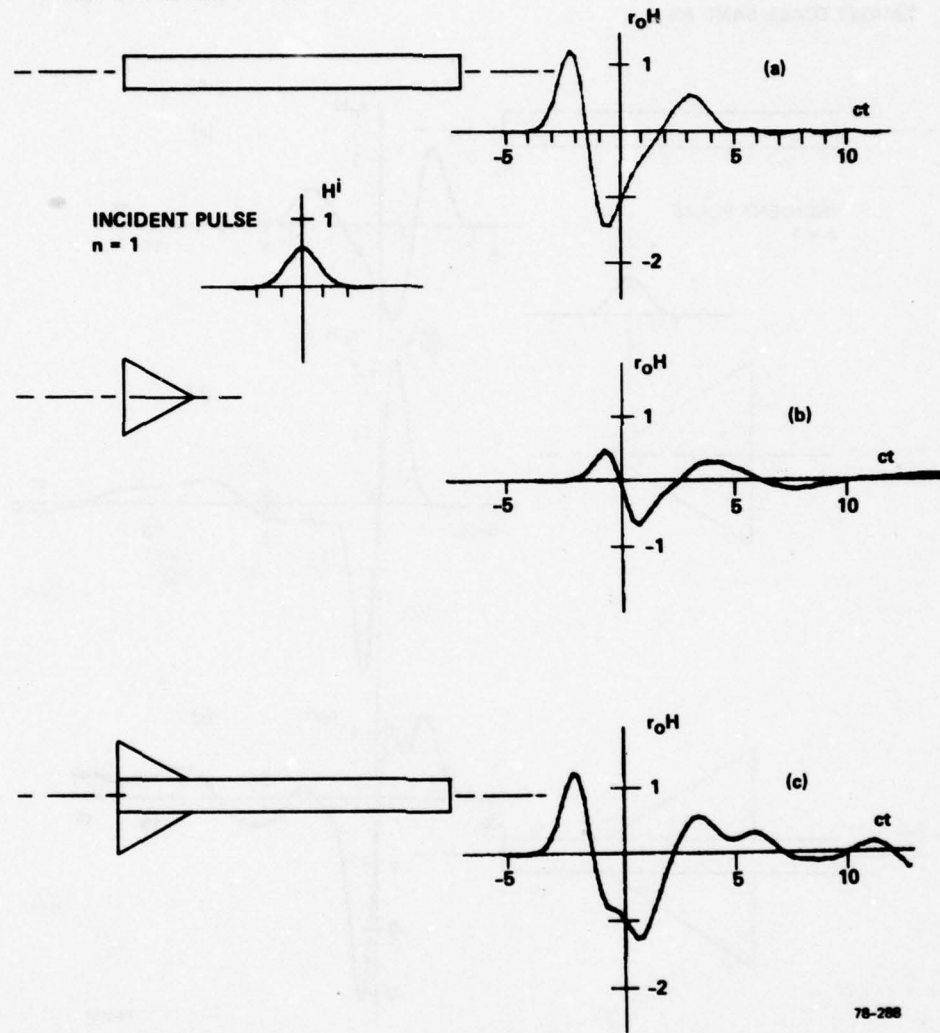


FIG. 12 Effect of small fin on cylinder response, $\alpha = 90^\circ$.

TARGET SCALE SAME AS ct

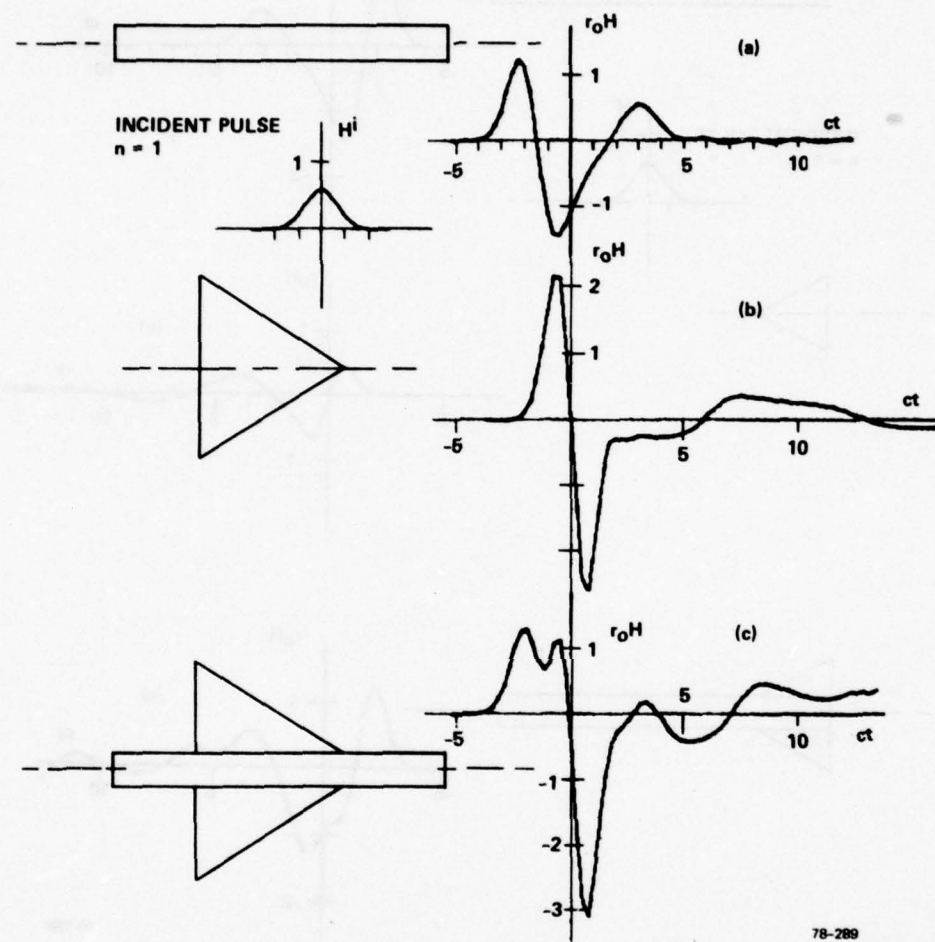
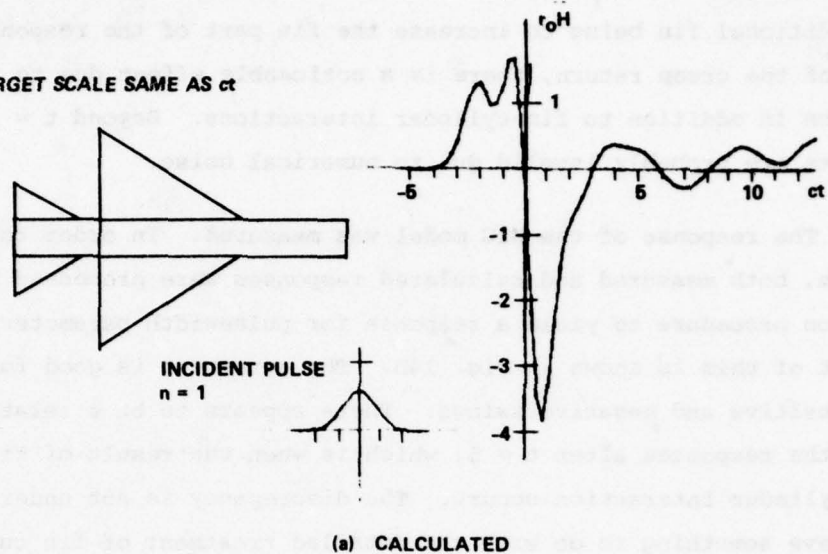


FIG. 13 Effect of large fin on cylinder response, $\alpha = 90^\circ$.

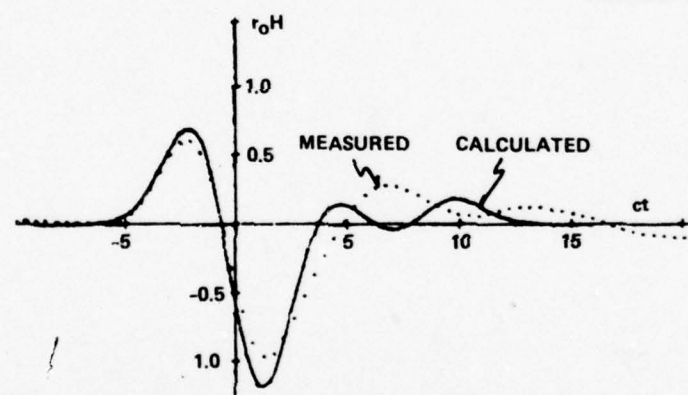
creep return near $t = 8$. The total response of the MIG model is shown in Fig. 14, also at broadside incidence. At this aspect, to first order, this looks similar to the large-fin-on-cylinder response, the main effect of the additional fin being to increase the fin part of the response. At the time of the creep return, there is a noticeable effect due to fin-fin interaction in addition to fin-cylinder interactions. Beyond $t = 10$ or so, the results are probably invalid due to numerical noise.

The response of the MIG model was measured. In order to permit comparison, both measured and calculated responses were processed by a convolution procedure to yield a response for pulselwidth parameter $n = 0.5$. The result of this is shown in Fig. 14b. The agreement is good for the initial positive and negative swings. There appears to be a relative time shift in the responses after $t = 5$, which is when the result of fin-fin and fin-cylinder interaction occurs. The discrepancy is not understood, but may have something to do with the detailed treatment of fin currents at the singular edges.

TARGET SCALE SAME AS ct



(a) CALCULATED



(b) CALCULATED COMPARED WITH MEASUREMENT $n = 0.5$

78-290

FIG. 14 Calculated MIG-21 response, $\alpha = 90^\circ$.

bedjomec edf ddfw redapar (2) "superficed nofisimwupu yonupert yipin"
salugur ofelqmo edf Rleiy of , & nofisimwupu betelqoed as eanaper salugur
.seroqer

SECTION 3

STIE CALCULATION OF SCATTERING CENTER RESPONSES

CONTIN. 1.2

The principal contributors to the response of a complex target are the scattering centers (surface discontinuities and points on a surface with a normal bisecting the angle between incidence and observation). This is more true at higher frequency, when the separation between scattering centers is greater than a few wavelengths, or equivalently, when the separation is larger than the incident pulselength, and the direct interaction between scattering centers via surface currents (creep waves) can be neglected. This fact has permitted the successful application to response calculations of physical optics theory (which holds only in the limit of very high frequency and fails to predict polarization dependence) and the geometrical theory of diffraction, GTD (which is based on the response of a wedge and includes polarization dependence, but requires the application of a transformation from wedge to actual scattering center geometry).

In the time domain, the impulse response predicted by these theories can be viewed as a series of singularities. These response singularities can also be obtained analytically by considering the surface currents in the immediate neighborhood of the scattering center. (See Ref. 1 and Appendix 8.3). Such an approach yields the physical optics terms and a first order (polarization dependent) correction. This method is made use of in what follows as an approximate verification of the new technique.

The time domain (STIE) technique presented here is a direct method of calculating the broadband response of scattering centers, edges as well as points on smooth surfaces. The response of a complex target can then be obtained by direct superposition in the time domain. Alternatively, these scattering center responses can be used as input to the

"high frequency augmentation technique" [5] together with the smoothed impulse response as calculated in Section 2, to yield the complete impulse response.

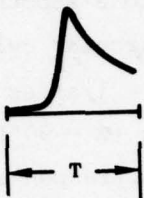
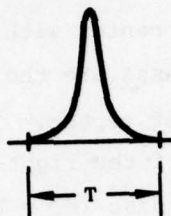
3.1 METHOD

The approach is the well tested technique of the space-time integral equation described in Section 2, but using as the incident field a smoothed impulse of very short duration, T . The farfield response of the scattering center is then considered to occupy a time window equal to the pulselength and corresponding to the time that the scattering center is illuminated (Fig. 15). The region of the target around the center which contributes to this response, are then those points which are within distance $cT/2$ along the direction of incidence. (We consider here only the monostatic case, although the method is readily applicable to the bistatic case as well.)

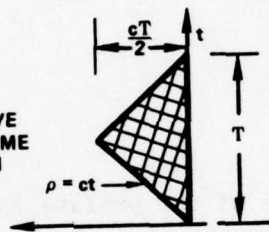
In the numerical implementation, the surface and time are divided into a fine mesh. The surface currents are calculated first and then from them, the farfield. (See Section 2.2.) Considerable efficiency of calculation is realized when use is made of the fact that the space-time region on the surface is bounded by the lines $\rho = ct$ and $\rho = cT - ct$ (see Fig. 15d), where ρ is the projected distance of the surface node from the scattering center along the direction of incidence.

The method is demonstrated on a prolate spheroid and a right circular cylinder as a function of aspect angle. Each of these objects is centered at the origin with axis along the z -axis. The direction of incidence is in the yz plane at an angle, α , with respect to the z -axis. In the response curves, the time of return, T_z , is measured with respect to a return from the origin and is thus given by $cT_z = -2\rho_c$ where ρ_c is the distance of the specular point from the origin along the direction of incidence. The response to both TE and TM polarizations are presented, where TE means \vec{E} transverse to the yz plane. The incident pulselength parameter was $n = 16$. The pulselength for these calculations was $T = 8/n$.

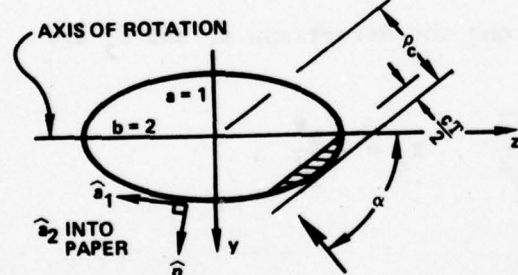
(a) ILLUMINATED AREA (b) INCIDENT PULSE (c) FAR FIELD RESPONSE



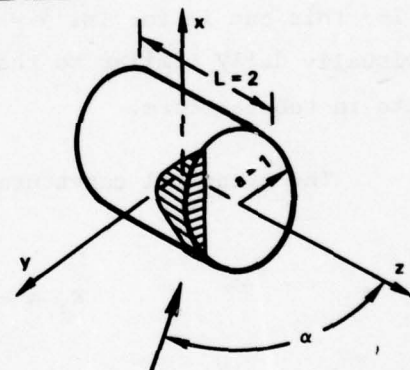
(d) ACTIVE SPACE-TIME REGION



AXIS OF ROTATION



(e) PROLATE SPHEROID



(f) RIGHT CIRCULAR CYLINDER

78-291

FIG. 15 Scattering center response calculation relationships.

The calculations were verified by measurement using a large target and short pulse excitation.

The prolate spheroid responses as a function of α , essentially give the result due to a smooth scattering center with principal curvatures K_1, K_2 . The right-circular cylinder responses are the responses of a curved 90° edge ($K_1 = \infty, K_2 = 1/a$) as a function of aspect. In addition, the end-on ($\alpha = 0$) and broadside ($\alpha = 90^\circ$) responses of the right-circular cylinder represent the specular responses of a flat disc ($K_1 = K_2 = 0$) and a line ($K_1 = 1/a, K_2 = 0$) on a curved surface.

3.2 RESULTS

3.2.1 Prolate Spheroid

A typical response of the prolate spheroid is illustrated in Fig. 16; this one is for TM, $\alpha = 60^\circ$. At other aspects, the responses are visually duly similar so that it is more instructive to present the results in tabular form.

The principal curvatures along the directions \hat{a}_1 and \hat{a}_2 are

$$K_1 = -\frac{B^{3/2}}{a^2 b^2}, \quad K_2 = -\frac{B^{1/2}}{a^2}, \quad (34)$$

where

$$B = a^2 \sin^2 \alpha + b^2 \cos^2 \alpha$$

a, b are the semi-minor and -major axes,

\hat{a}_1 is along a meridian line,

$$\hat{a}_2 = \hat{\phi}. \quad (\text{See Fig. 15e})$$

The expected impulse response for a smooth surface with finite curvatures is of the form (see Appendix 8.3)

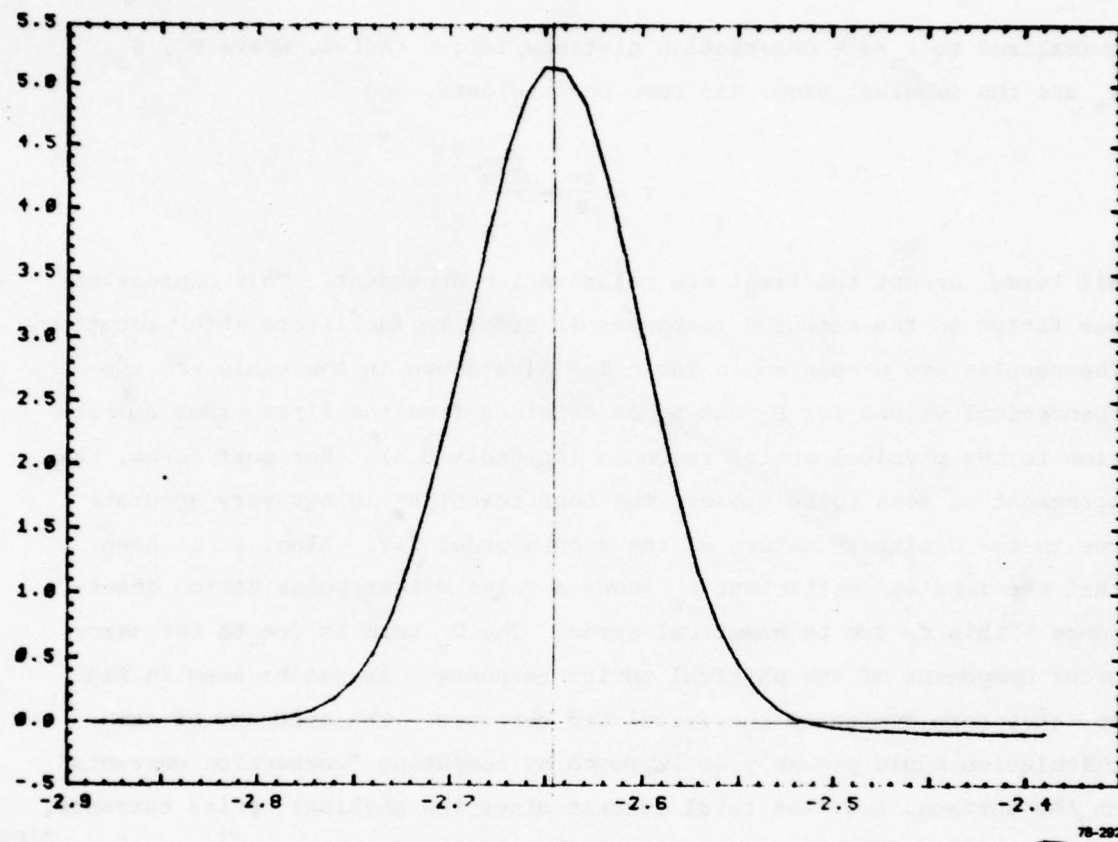


FIG. 16 Typical prolate spheroid scattering center response (TM, $\alpha = 60^\circ$).

$$\frac{r_o}{a} h\left(\frac{ct}{a}\right) = P_z \delta(\tau) + S_z u(\tau) + R_z \tau u(\tau) + \dots, \quad (35)$$

normalized to r_o/a = observation distance/target radius, where P_z , S_z , R_z are the impulse, step, and ramp coefficients, and

$$\tau = \frac{ct}{a} - \frac{cT_z}{a}.$$

All terms, except the first are polarization dependent. This expression was fitted to the computed responses in order to facilitate interpretation. The results are presented in Table I. Also shown in the table are the theoretical values for P_z and S_z as obtained from the first order correction to the physical optics response (Appendix 8.3). For most cases, the agreement is seen to be close. The coefficient R_z is not very accurate due to the arbitrary nature of the second order fit. Also, it is seen that the impulse coefficient P_z shows a false slight polarization dependence - this is due to numerical error. The P_z term is due to the zero-order component of the physical optics response. As can be seen in Fig. 16, this term dominates the calculated response. The accuracy of the calculation could probably be improved by computing "correction currents" on the surface, i.e. the total current minus the physical optics currents.

On the surface STIE of Section 2.2.3, the latter is the term $\vec{J}_{PO} = 2\hat{a}_n \times \vec{H}^{inc}$.

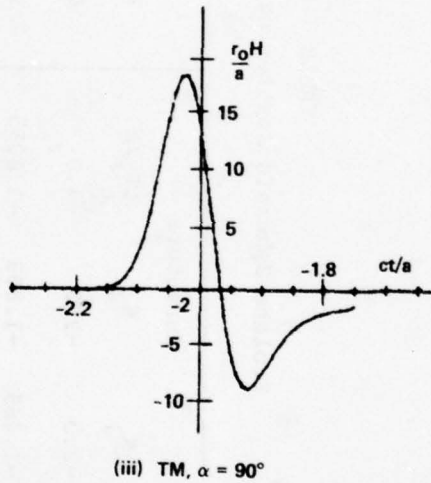
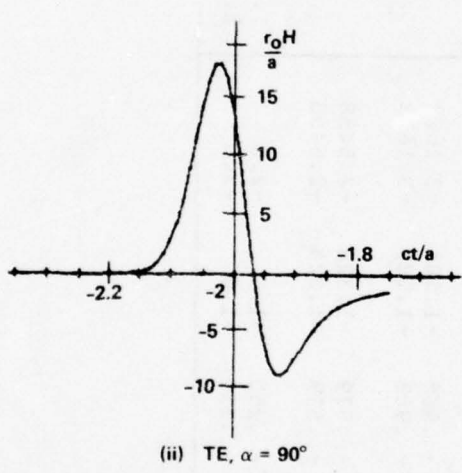
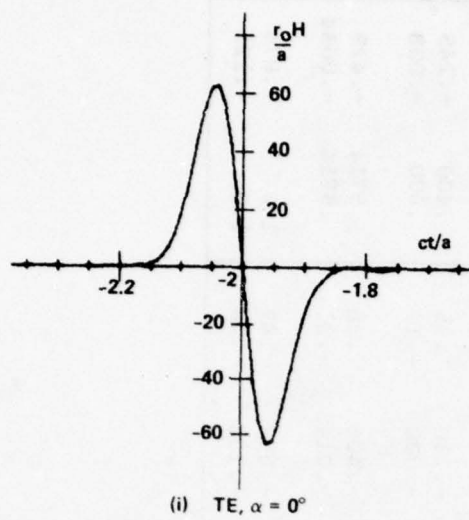
3.2.2 Right Circular Cylinder

The geometry for these cases is illustrated in Fig. 15f. The end-on and broadside aspect responses are presented in Fig. 17. The end-on response is polarization independent and is given theoretically by

$$\frac{r_o}{a} h\left(\frac{ct}{a}\right) = D_z \delta'(\tau) + P_z \delta(\tau) + H_z \tau^{-\frac{1}{2}} u(\tau) + \dots, \quad (36)$$

TABLE I
Prolate Spheroid Scattering Center Responses

Aspect α	Polarization	Curvature			Calculated			Theoretical	
		K_1	K_2	cT_z/a	P_z	S_z	R_z	P_z	S_z
0	NA	-2.0	-2.0	-4.0	.250	-.0615	-.006	.25	-.0625
30	TE	-1.465	-1.803	-3.6055	.3049	-.114	.08	.3077	-.137
30	TM	-1.465	-1.803	-3.6055	.3108	-.052	-.09	.3077	-.033
45	TE	-.988	-1.581	-3.1623	.3958	-.220	.25	.400	-.245
45	TM	-.988	-1.581	-3.1623	.4038	-.030	-.19	.400	-.008
60	TE	-.579	-1.323	-2.6458	.5673	-.406	.38	.5714	-.429
60	TM	-.579	-1.323	-2.6458	.5752	-.0145	-.31	.5714	-.0034
90	TE	-.250	-1.0	-2.0	.9930	-.852	.47	1.0	-.875
90	TM	-.250	-1.0	-2.0	1.0070	-.132	-.28	1.0	-.125



78-293

FIG. 17 RCC scattering center responses — end-on and broadside.

where D_z , P_z are the doublet and impulse coefficients,

H_z is the coefficient of the $t^{-\frac{1}{2}}$ functional,

$$\tau = \frac{ct}{a} - \frac{ct_z}{a}.$$

The expected values (from physical optics) of the first term is $D_z = 0.50$. At broadside the response is polarization dependent and is given by (Appendix 8.3)

$$\frac{r_o}{a} h\left(\frac{ct}{a}\right) = G_z \tau^{-3/2} u(\tau) + H_z \tau^{-1/2} u(\tau) + \dots \quad (37)$$

the expected values are $G_z = .15915$, $H_z = -.079$ (TE), $H_z = +.079$ (TM). The results of fitting these functionals to the measured responses are presented in Table II. Agreement with theoretical expectations is good except for the 90° TE case, which is probably in error.

At intermediate angles the responses are much smaller in magnitude than at 0° or 90° . Responses are plotted at the same scale in Fig. 18 for both TE and TM cases.

The theoretical form of the response is given by

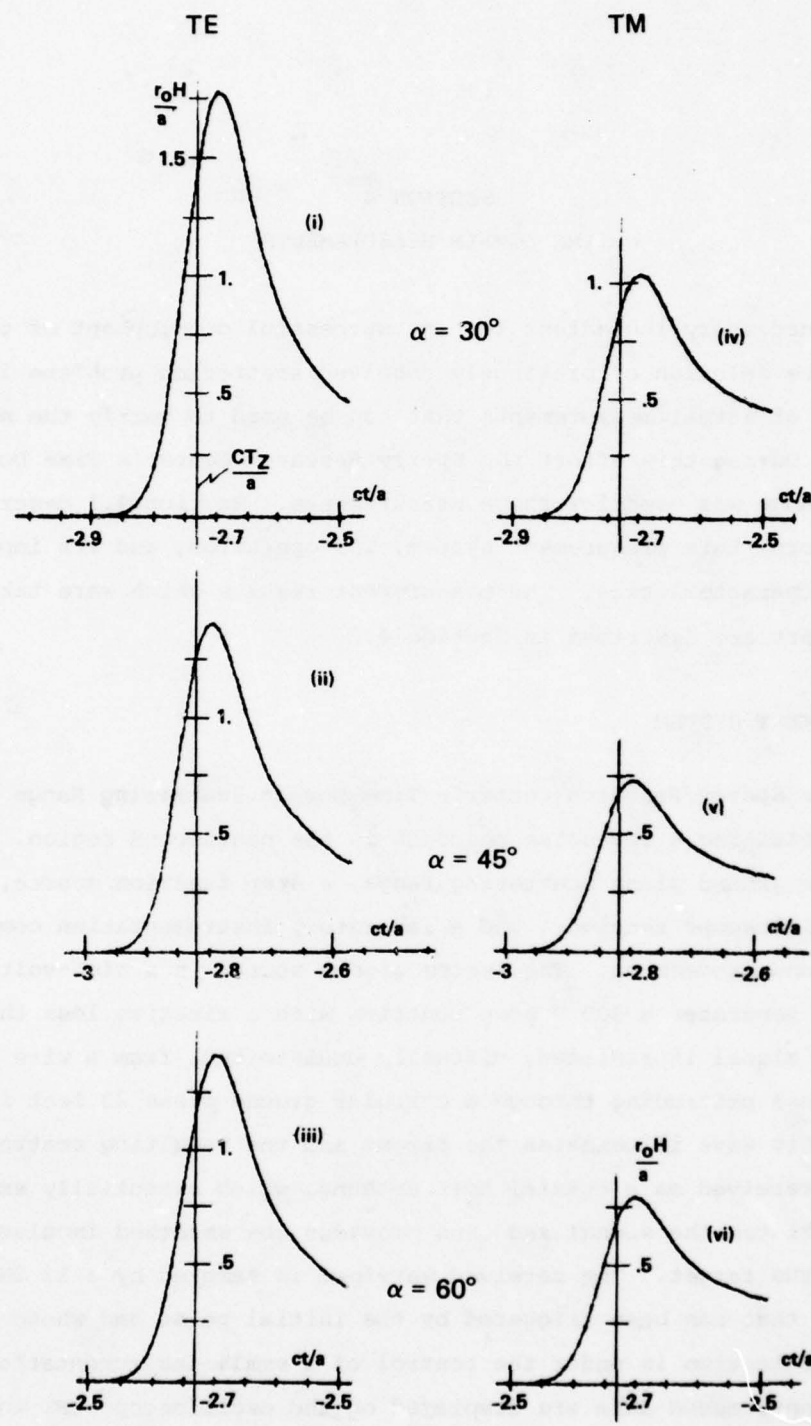
$$\frac{r_o}{a} h\left(\frac{ct}{a}\right) = H_z \tau^{-\frac{1}{2}} u(\tau) + K_z \tau^{\frac{1}{2}} u(\tau) + \dots \quad (38)$$

The results of fitting these functionals to the calculated responses is given in Table II.

Measurements of a RCC are described in Section 4. The measurements were made with a pulselength about 3 times longer than these calculations, so that comparison (after convolution) can only be made over the initial portion of the measured response. The results agree within this time window.

TABLE II
RCC Scattering Center Responses

Aspect	Polarization	cT_z/a	D_z	G_z	P_z	H_z	K_z
0	NA	-2.0	.4930	0.	.162	-.051	
30	TE	-2.7321	0.	0.	0.	.3725	-.63
30	TM		0.	0.	0.	.2067	-.004
45	TE	-2.8284	0.	0.	0.	.2930	-.34
45	TM		0.	0.	0.	.1492	.07
60	TE	-2.7321	0.	0.	0.	.2823	-.39
60	TM		0.	0.	0.	.1574	.02
90	TE	-2.0	0.	-.1585	0.	.006	-.07
90	TM		0.	-.1599	0.	.073	-.29



78-204

FIG. 18 RCC scattering center responses — intermediate angles.

SECTION 4

TIME DOMAIN MEASUREMENTS

A necessary ingredient for any successful development of techniques for the solution of previously unsolved scattering problems is the availability of actual measurements that can be used to verify the new techniques. During this effort the Sperry Research Center's Time Domain Scattering Range was used for these measurements. Section 4.1 describes, in summary form, this measurement system, its operation, and its important performance characteristics. The measurement results which were taken for this effort are described in Section 4.2.

4.1 MEASUREMENT SYSTEM

The Sperry Research Center's Time Domain Scattering Range is a system for obtaining a low-noise response in the nanosecond region. It consists of a ground plane scattering range, a step function source, a sampling oscilloscope receiver, and a laboratory instrumentation computer for control and processing. The system signal source is a high-voltage switch which generates a 300 V step function with a risetime less than 100 ps. The signal is radiated, virtually undistorted, from a wire transmitting antenna protruding through a circular ground plane 20 feet in diameter. This wave illuminates the target and the resulting scattered waveform is received on a coaxial horn antenna, which essentially smoothes and differentiates the signal and thus provides the smoothed impulse response of the target. The received waveform is sampled by a 12 GHz oscilloscope that has been triggered by the initial pulse and whose sampling gate deflection is under the control of a small instrumentation computer. Unprocessed data are displayed on the oscilloscope CRT while the sampled-and-held waveform is passed through a low-pass filter, digitized, read into the computer, and stored on magnetic tape automatically. This

system has been designed to correct the long-term timing drift and/or amplifier drift. In addition, the waveforms are stored in such a way that they are ready for the subsequent operations of averaging (to remove short-term noise) and baseline processing. The effects of a time varying baseline are subtracted from measured waveforms to improve system accuracy.

The salient characteristics of the range are the speed and simplicity with which multi-octave frequency-domain data can be obtained. These advantages accrue because the time-domain scattering range yields an "uncontaminated" interval of time between the arrival of the direct wave and the arrival of unwanted reflections. Targets are usually located anywhere from two to five feet from the transmitting antenna. The response from the antenna tip and the table edge occur at approximately 15 ns. Thus, a "clean window" exists between 4 ns and 15 ns which can be used to view the target responses. The entire region between the direct transmission and the table edge response forms a convenient time "window" to view the target response and allows one to "gate out" (in time) unwanted reflections. Thus, undistorted transient target responses can be viewed without resorting to elaborate and expensive anechoic chambers. In addition, a single time-domain measurement obviates the requirement for tedious measurement of the amplitude and phase responses at many frequencies.

The accuracy of the measurement system has been estimated for the results presented in this section. The peak of the incident pulse as measured on the sampling oscilloscope is approximately 400 mV, and a typical target response has a peak value in the vicinity of 10 mV. When using the 10 mV scale on the sampling oscilloscope, the standard deviation of the sample mean is estimated to be

$$\sigma_{\bar{v}} = 0.5 \text{ mV}$$

if 16 scans are averaged. Thus, the estimated standard deviation of the sample mean \bar{v} is in the vicinity of 5% of the peak value of the target response.

In addition, the measured responses are further processed by means of a convolution procedure to obtain the response due to a Gaussian shaped incident pulse rather than the approximate smoothed impulse used in the actual measurements. Figure 19 displays the actual measured incident pulse along with the smoothed Gaussian pulse that was used in the convolution process. The frequency spectrum of these two pulses is displayed in Fig.

20. The time domain expression for the Gaussian pulse is given by

$$e(t) = E_o \frac{a_n}{\sqrt{\pi}} \exp \left[-a_n^2 (t - t_o)^2 \right]$$

and the frequency domain expression is

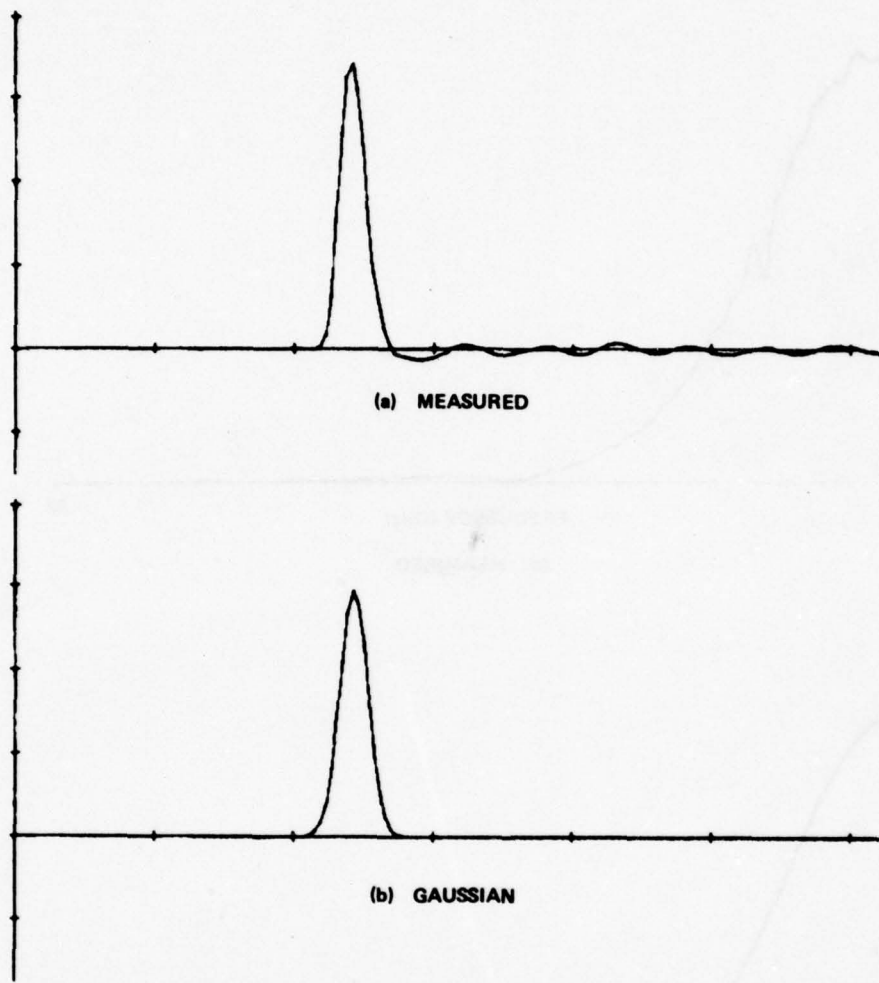
$$E(\omega) = E_o \exp \left[-\omega^2 / (2a_n)^2 \right] \exp(-j\omega t_o)$$

The amplitude coefficient E_o was set equal to the dc value of the measured incident pulse. The width coefficient a_n was obtained by requiring that the 50% value of $|E(\omega)|$ occur at the same point in frequency as the 50% value of the magnitude of the transformed measured incident pulse. The width of the resulting Gaussian pulse becomes 0.59 ns or approximately 7 inches. An added benefit of this process is the reduction of high frequency noise in the response.

This measurement system provides the capability of measuring and recording the processed high precision smoothed impulse response data on computer computable tape. These data may then be used to find the response due to any radar waveform whose spectrum is contained within the spectrum of the original measurement smoothed impulse illumination. Further details of this system may be found in the references [1-7].

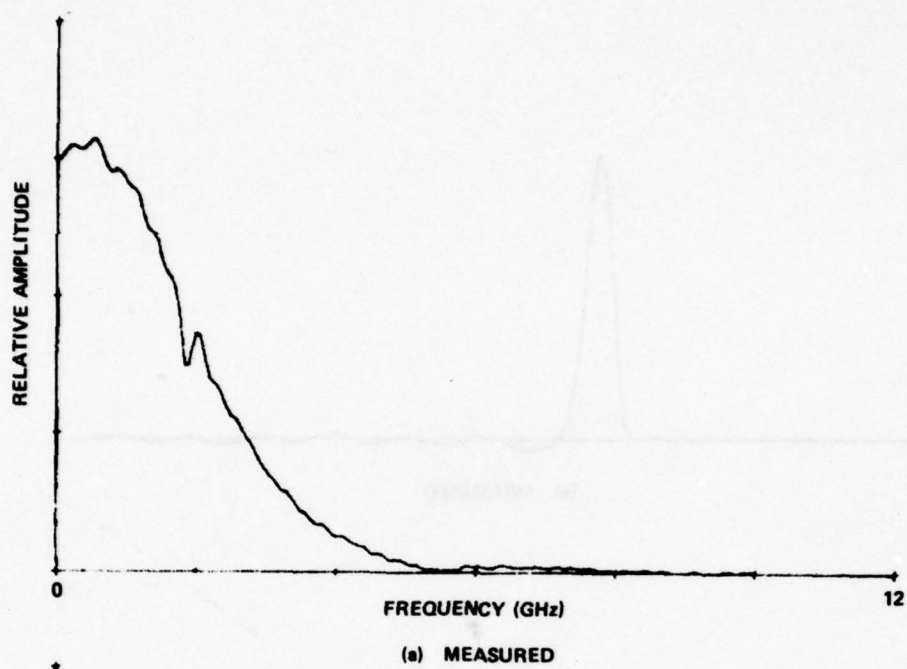
4.2 MEASURED RESULTS

In previous studies [1-6] the smoothed impulse response was measured for numerous target geometries. These previous measurements are summarized in Table 3. During the present contract, smoothed impulse

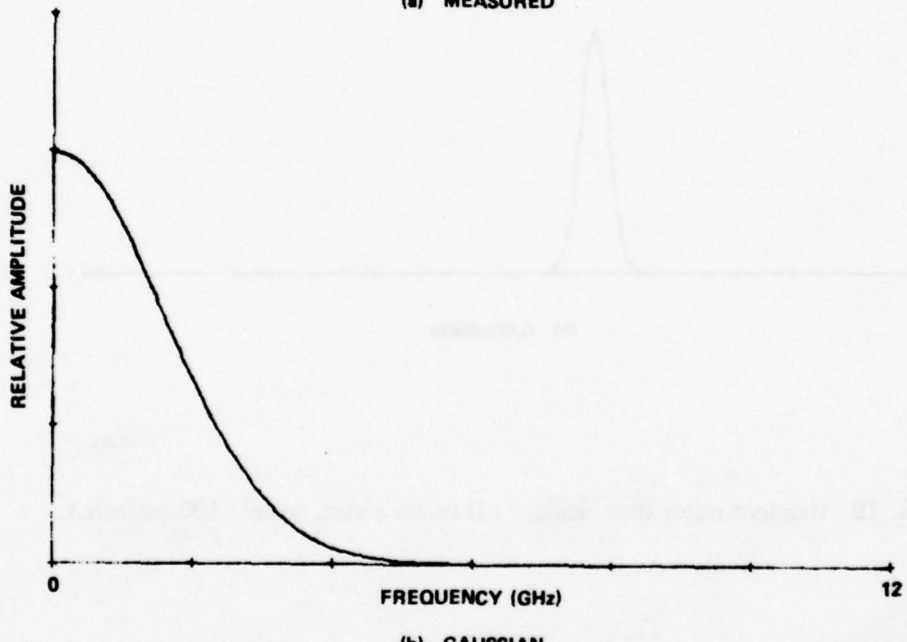


78-295

FIG. 19 Incident pulse (hor. scale: 1.0 ns/div.; vert. scale: 100 mV/div.).



(a) MEASURED



(b) GAUSSIAN

78-296

FIG. 20 Spectrum of incident pulse.

TABLE III
Summary of Previous Measured Responses

June 1970 [2] and May 1973 [5]

ADC	satellite model
UES	satellite model
GGTS-2	satellite model
Wire	$L/10 = 10$
SSS	satellite model
EWRS	satellite model

November 1970 [6] and May 1973 [5]

8 in. cube
Right square cylinder, $L = 12$ in., $D = 4$ in.
Right circular cylinder, $L = 12$ in., $D = 4$ in.
Right circular cylinder, $L = 8$ in., $D = 4$ in.
4½ in. sphere
8 in. sphere
Sphere capped cylinder, $L = 12$ in., $D = 4$ in.
Sphere cone sphere

May 1974 [3]

8 x 8 in. square plate
4 x 8 in. square plate
8 in. circular disc
4 x 8 in. corner reflector
8 x 8 in. circular cylinder section
8 x 8 in. parabolic cylinder section
8 in. parabolic dish

March 1976 [7]

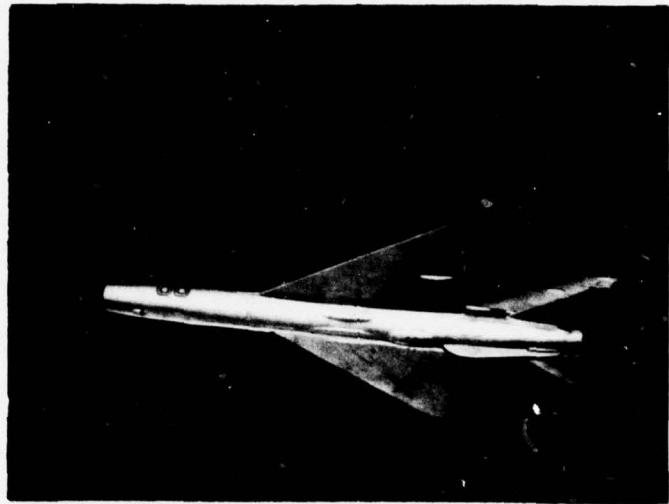
Cylinder with square fins, $L = 8$ in., $D = 4$ in.
Cylinder with square fins, $L = 12$ in., $D = 4$ in.

responses were measured for a number of triangular fins, a Revelle MIG-21 model, and a machined MIG-21 model. In addition smoothed impulse scattering center responses were measured using a large triangular fin and a large right circular drum. The responses were measured for both the naked conducting bodies and for Radar Absorbing Material (RAM) covered bodies. The specific measurements taken on this effort are summarized in Table 4. The Revelle MIG-21 model is 1/32 scale and is displayed in Fig. 21(a). The machined MIG-21 model that was used for the measurements is shown in Fig. 21(b) and the dimensions are given in Fig. 2. Note that the photos in Fig. 21 were taken of the actual models sitting on a mirror surface. Fig. 22 displays the actual models sitting on the time domain scattering range. The target geometries of the triangles is shown in Fig. 23. The target geometries of the large triangle and the large drum are displayed in Fig. 24. The smoothed impulse responses which are displayed in this section are due to the incident smoothed impulse shown in Fig. 19(b), which has a width of 0.59 ns.

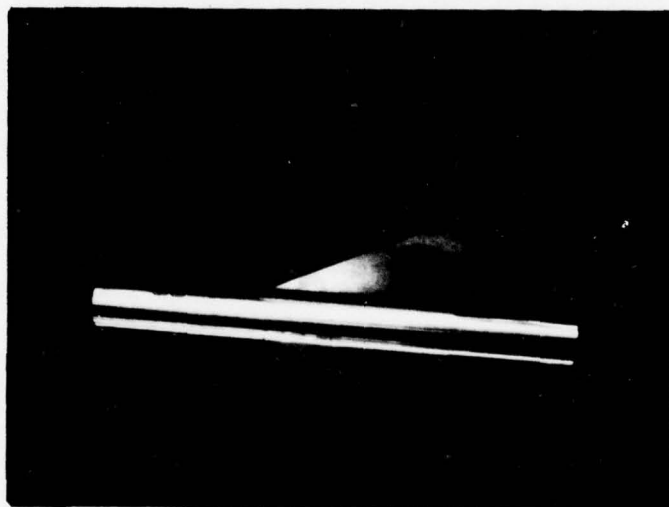
In Fig. 25, the measured smoothed impulse response of a MIG-21 Revelle model is shown for the case where the image plane is perpendicular to the wings and coincides with the rudder. This model was fabricated from Revelle kit H267, cut in half, and painted with Emerson & Cuming, Inc. Eccoshield ES conducting paint. This provides the response for the case of TE polarization. For 0° incidence (nose-on) the return from the nose which should appear at 1.2 ns is embedded in the system noise. At approximately 3.1 ns a negative pulse appears that is due to the scattering from the rear edge of the wings. Note that the return from the nose, the fuselage sides and the leading edge of the wings is negligible relative to the return from the trailing edge of the wing. Finally, at approximately 3.9 ns a second negative return appears that can be attributed to the trailing edge of the stabilizers. As the angle of incidence increases from 0° to 90° the response shape changes smoothly reflecting the change in relative distances of the scattering centers. At 90° the beginning of the return from the side of the fuselage appears at approximately 1.7 ns followed immediately by the large return from the wings and stabilizers

TABLE IV
Summary of Measured Responses

Revelle MIG-21 Model	0°, 30°, 60°, 90°, 120°, 150°, 180°
Machined MIG-21 Model	0°, 30°, 60°, 90°, 120°, 150°, 180°
30° Triangle	0°, 30°, 60°, 90°, 120°, 150°, 180°
45° Triangle	0°, 30°, 60°, 90°, 120°, 150°, 180°
60° Triangle	0°, 30°, 60°, 90°, 120°, 150°, 180°
Large 30° Triangle	0°, 30°, 60°, 90°, 120°, 135°, 150°, 165°, 180°
Large 30° RAM Triangle	120°, 135°, 150°, 165°, 180°
Large Cylinder	0°, 30°, 45°, 60°, 75°, 90°
Large RAM Cylinder	30°, 45°, 60°, 75°, 90°



(a) REVELL MODEL



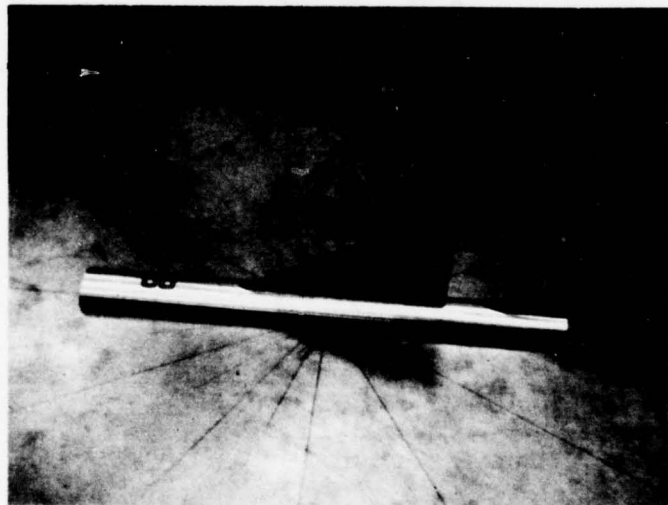
(b) MACHINED MODEL

78-298

FIG. 21 MIG-21 models on a mirror plane.



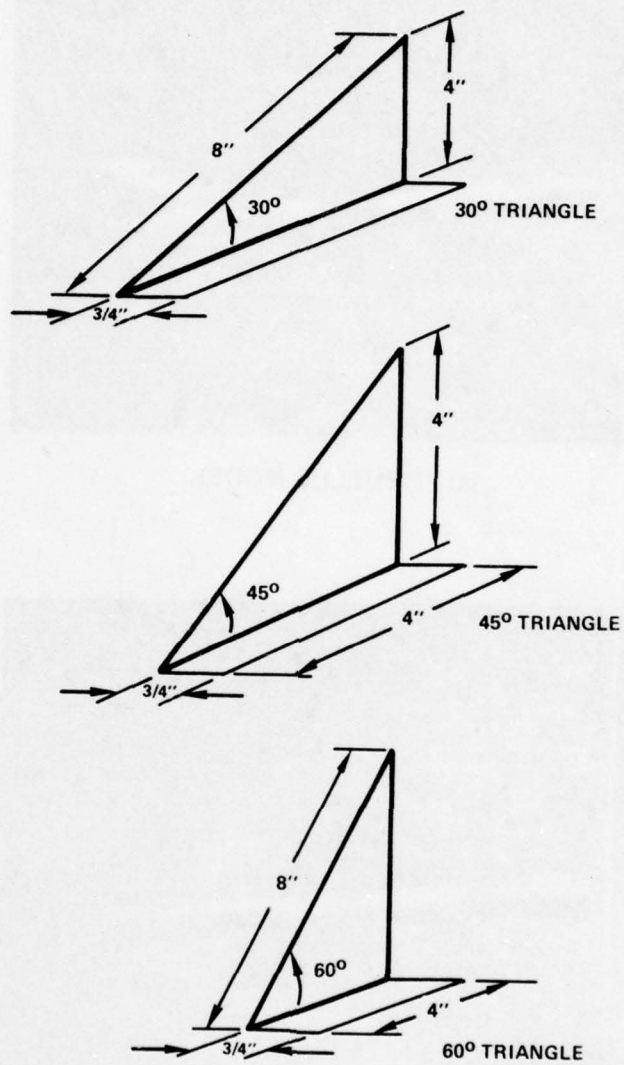
(a) REVELLE MODEL



(b) MACHINED MODEL

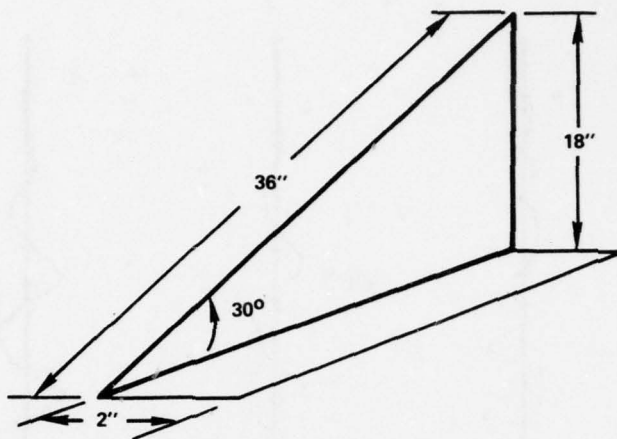
78-297

FIG. 22 MIG-21 models on the scattering range.

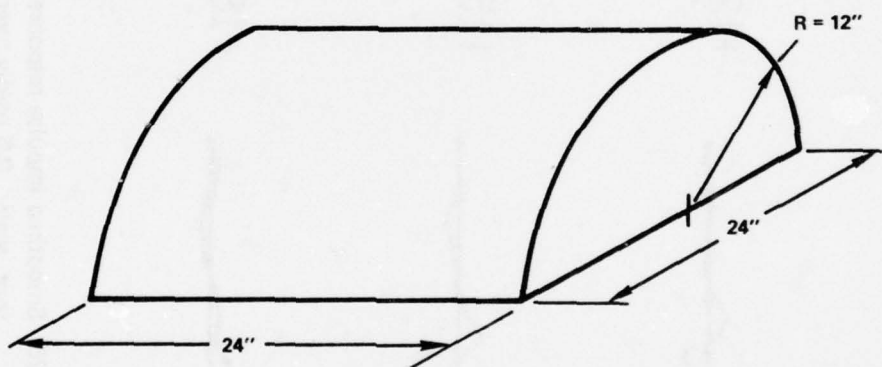


78-299

FIG. 23 Target geometry of triangular plates.



(a) LARGE 30° TRIANGLE, $1/16''$ THICK



(b) LARGE CYLINDER

78-300

FIG. 24 Target geometry of large triangular plate and large cylinder models.

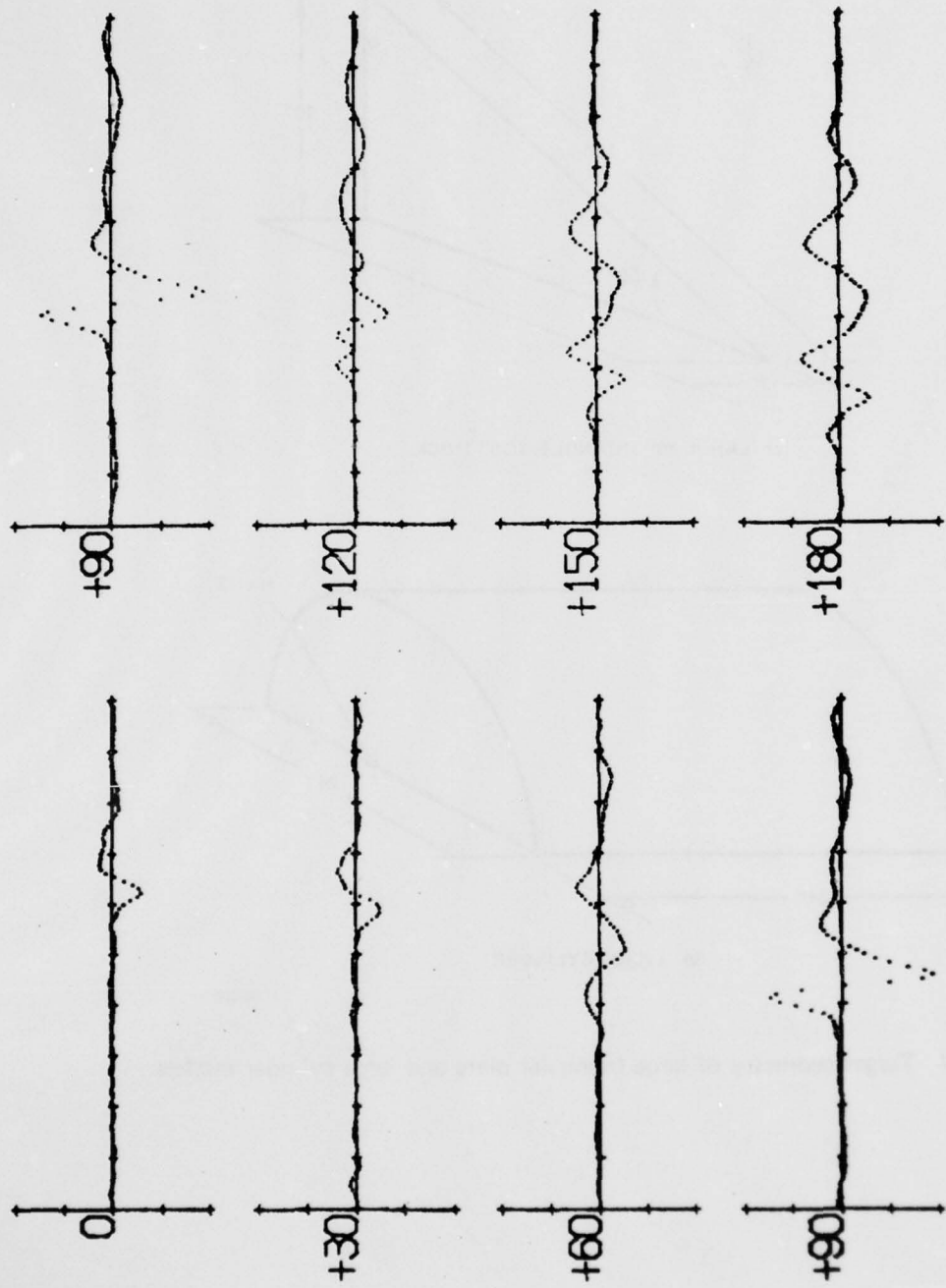


FIG. 25 Smoothed impulse response of Revelle MIG-21 model
(hor. scale: 0.5 ns/div.; vert. scale: 5 mV/div.).

78-301

that approximate a smoothed doublet. This is followed by an oscillating waveform due to currents traveling along the surface of the wings. Continuing on to 180° , the return from the end of the fuselage and the rear of the stabilizers appear first at approximately 0.8 ns. This is followed at approximately 1.6 ns by a second positive pulse due to the return from the trailing edge of the wings. The response oscillates several times before damping out due to currents flowing on the wings. The return from the far end (the nose for this aspect) which should appear at approx. 3.3 ns is buried in the return from these traveling wing currents.

Fig. 26 displays the measured smoothed impulse response of the machined MIG-21 model (see Fig. 2) that represents the actual geometry used for the space-time integral equation computations that were described in Section 2. The responses measured for the machined model in Fig. 26 agree very closely with those in Fig. 25 measured for the Revelle model. The wave shape, amplitude, and relative spacings of features are in good agreement. The machined model exhibits a noticeable return from its nose for aspect angles of 0° to 90° , whereas, the nose return for the Revelle model is smaller. From these measurements, the location of the major scattering centers may be identified to be the trailing edge of the wings, the trailing edge of the stabilizers, the side of the fuselage and the ends of the fuselage.

In Fig. 27, the measured smoothed impulse response of a triangular plate with a 30° half angle as shown in Fig. 23. The image plane is normal to the face of the plate and 0° incidence corresponds to the apex-on direction. In Fig. 27 one can see that at 0° incidence there is very little return from either the apex or the sides. The significant return occurring at 2.4 nsec is a negative pulse from the trailing edge of this plate. As the aspect angle increases from 0° to 90° the return from the other portions of the plate emerge and at 90° the return from the plate approximates the derivative of the incident pulse. The second positive pulse at 90° aspect is due to currents traveling across the face of the plate before returning energy back to the observer. These effects become "stretched out" or dispersed as the aspect angle increases to 180° .

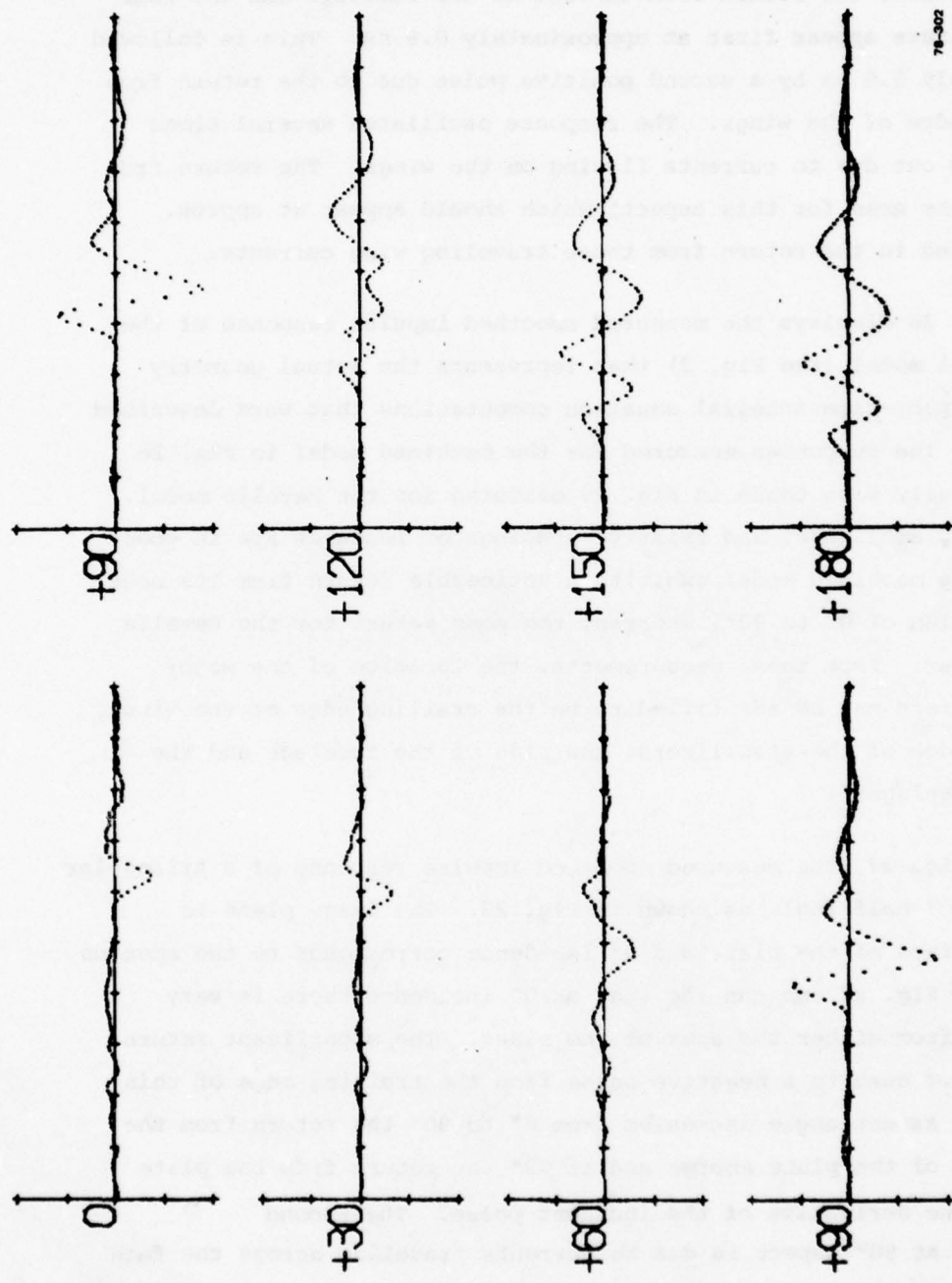


FIG. 26 Smoothed impulse response of machined MIG-21 model
(hor. scale: 0.5 ns/div.; vert. scale: 5 mV/div.).

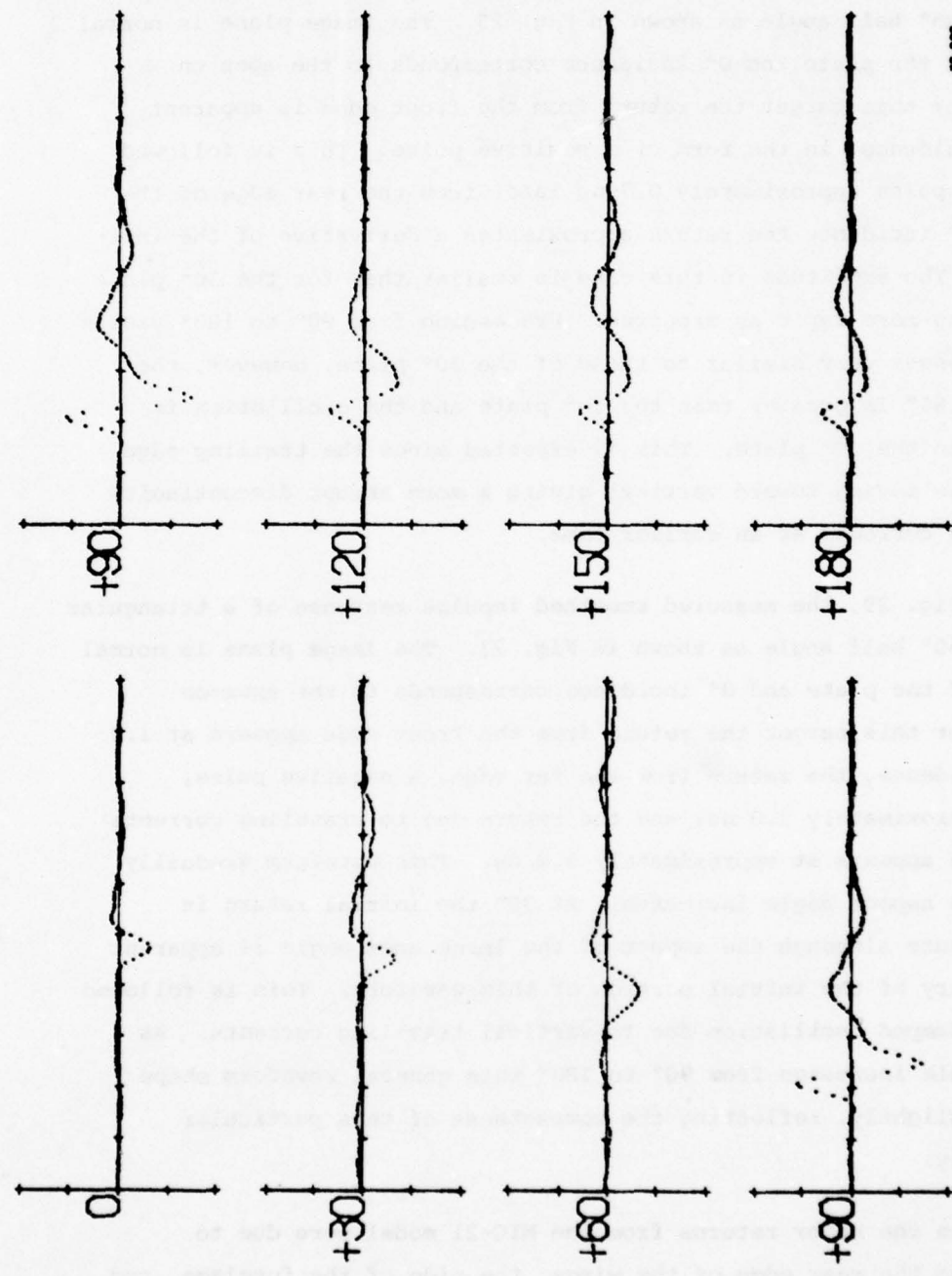


FIG. 27 Smoothed impulse response of 30° triangle
(hor. scale: 0.5 ns/div.; vert. scale: 5 mV/div.).

because now all parts of the plate are illuminated at different times.

In Fig. 28, the measured smoothed impulse response of a triangular plate with a 45° half angle as shown in Fig. 23. The image plane is normal to the face of the plate and 0° incidence corresponds to the apex-on direction. For this target the return from the front edge is apparent even at 0° incidence, in the form of a positive pulse. This is followed by a negative pulse approximately 0.7 ns later from the rear edge of the plate. At 90° incidence the return approximates a derivative of the incidence pulse. The amplitude in this case is smaller than for the 30° plate and the damping more rapid as expected. Proceeding from 90° to 180° yields a set of responses very similar to those of the 30° plate, however, the amplitude at 180° is greater than the 30° plate and the oscillation is more rapid than the 30° plate. This is expected since the trailing edge of the plate is moving toward vertical giving a more abrupt discontinuity to the surface currents at an earlier time.

In Fig. 29, the measured smoothed impulse response of a triangular plate with a 60° half angle as shown in Fig. 23. The image plane is normal to the face of the plate and 0° incidence corresponds to the apex-on direction. For this target the return from the front edge appears at 1.2 ns for 0° incidence, the return from the far edge, a negative pulse, appears at approximately 2.0 ns, and the return due to traveling currents on the surface appears at approximately 3.0 ns. This waveform gradually changes as the aspect angle increases. At 90° the initial return is doublet in nature although the impact of the large apex angle is apparent in the asymmetry of the initial portion of this waveform. This is followed in time by a damped oscillation due to vertical traveling currents. As the aspect angle increases from 90° to 180° this general waveform shape changes only slightly, reflecting the compactness of this particular target geometry.

Since the major returns from the MIG-21 model were due to scattering from the rear edge of the wings, the side of the fuselage, and the end of the fuselage, a large model of a 30° half angle triangular

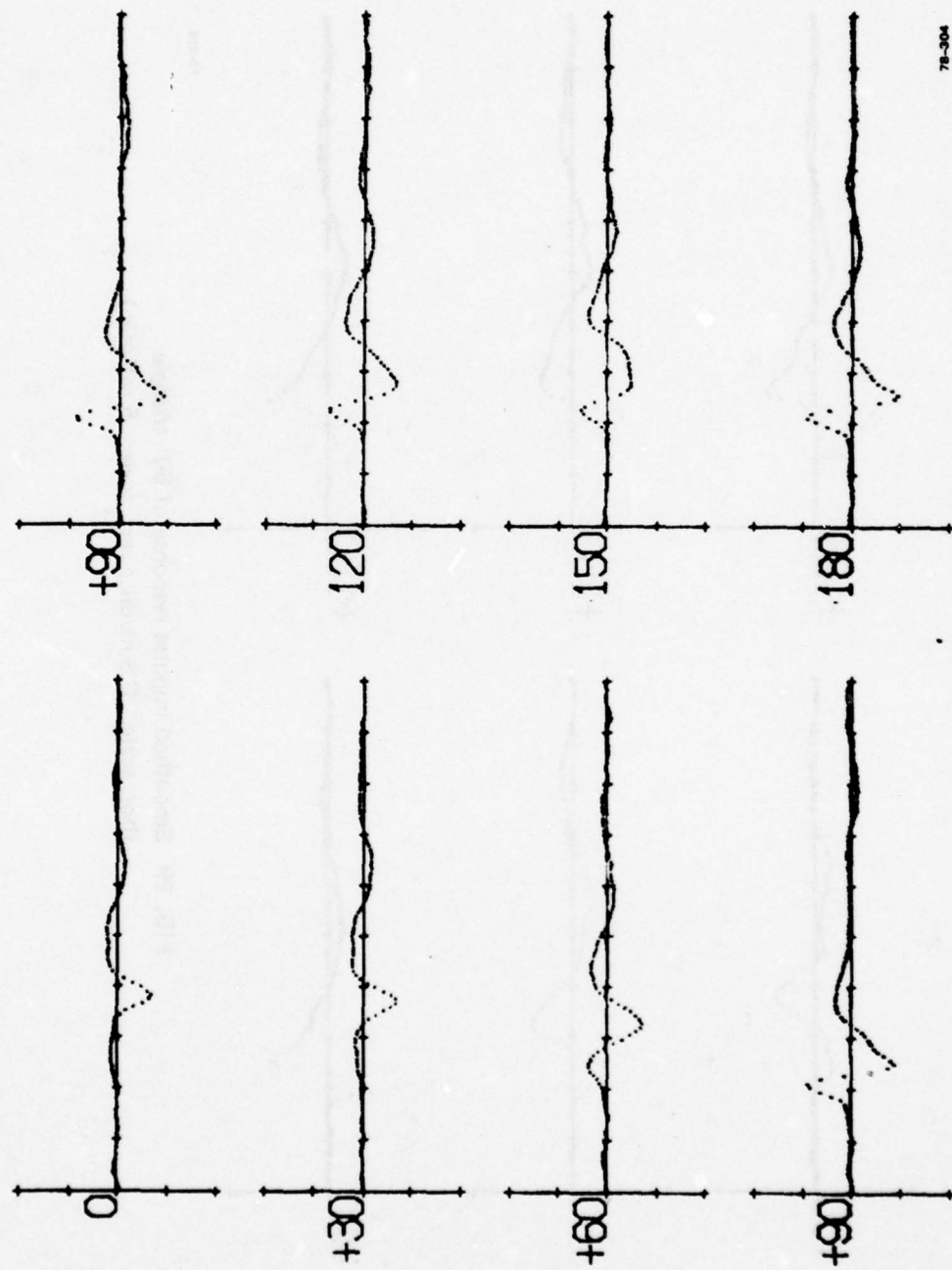


FIG. 28 Smoothed impulse response of 45° triangle
(hor. scale: 0.5 ns/div.; vert. scale: 5 mV/div.).

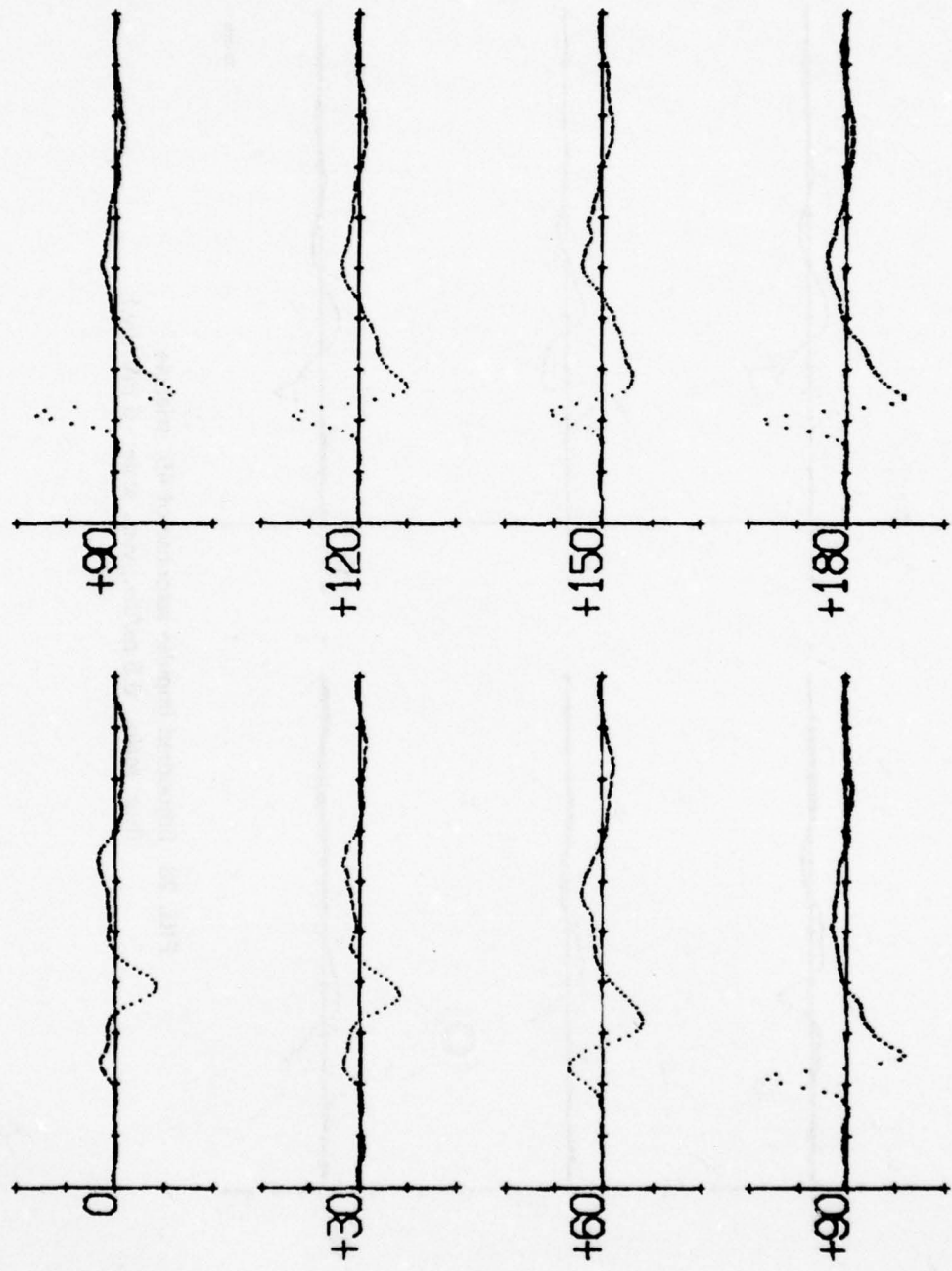


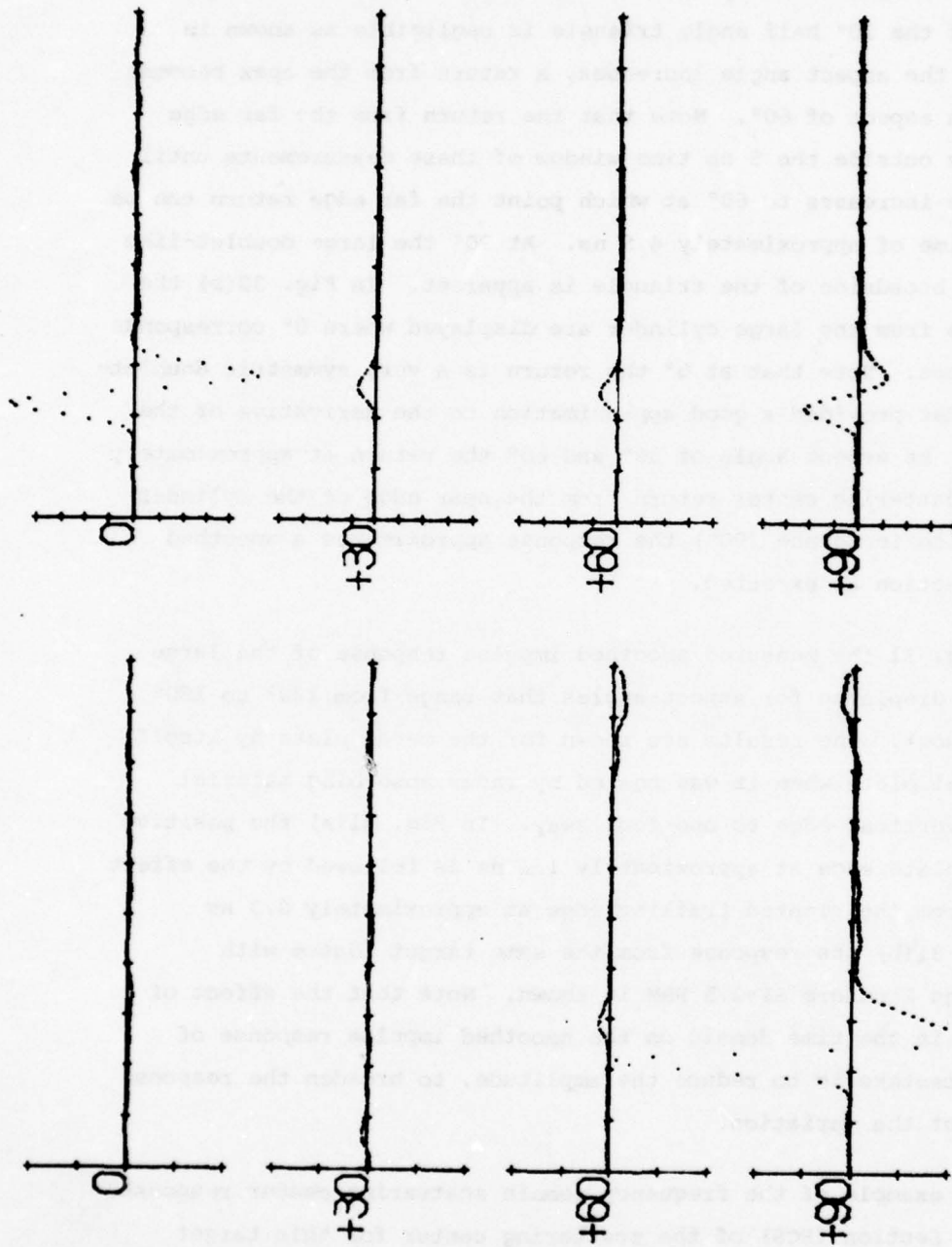
FIG. 29 Smoothed impulse response of 60° triangle
(hor. scale: 0.5 ns/div.; vert. scale: 5 mV/div.).

78-308

plate and a large model of a circular cylinder were fabricated as shown in Fig. 24. The results of smoothed impulse returns from the scattering centers on these targets is displayed in Fig. 30(a) & (b). The return from the apex of the 30° half angle triangle is negligible as shown in Fig. 30(a). As the aspect angle increases, a return from the apex becomes noticeable at an aspect of 60°. Note that the return from the far edge of this plate is outside the 5 ns time window of these measurements until the aspect angle increases to 60° at which point the far edge return can be observed at a time of approximately 4.5 ns. At 90° the large doublet-like return from the broadside of the triangle is apparent. In Fig. 30(b) the measured returns from the large cylinder are displayed where 0° corresponds to axial incidence. Note that at 0° the return is a very symmetric doublet-like waveform that provided a good approximation to the derivative of the incident pulse. At aspect angle of 30° and 60° the return at approximately 1.3 ns is the scattering center return from the near edge of the cylinder end. At broadside incidence (90°) the response approximates a smoothed $t^{-3/2}$ pseudo-function as expected.

In Fig. 31 the measured smoothed impulse response of the large 30° triangle is displayed for aspect angles that range from 120° to 180° (edge on incidence). The results are shown for the metal plate by itself and for the metal plate when it was coated by radar absorbing material (RAM) from the vertical edge to one foot away. In Fig. 31(a) the positive pulse from the plate edge at approximately 1.1 ns is followed by the effect of the return from the slanted trailing edge at approximately 0.3 ns later. In Fig. 31(b) the response from the same target coated with Emerson & Cumings Eccosorb SF-2.5 RAM is shown. Note that the effect of the RAM coating in the time domain on the smoothed impulse response of the scattering centers is to reduce the amplitude, to broaden the response and to smooth out the variation.

As an example of the frequency domain scattering center response, the Radar Cross Section (RCS) of the scattering center for this target is shown in Fig. 32 for aspect angles of 150° and 180°. The RCS of the



78-308

(b) LARGE CYLINDER

(a) LARGE 30° TRIANGLE

FIG. 30 Smoothed impulse response of scattering centers
(hor. scale: 0.5 ns/div.; vert. scale: 5 mV/div.).

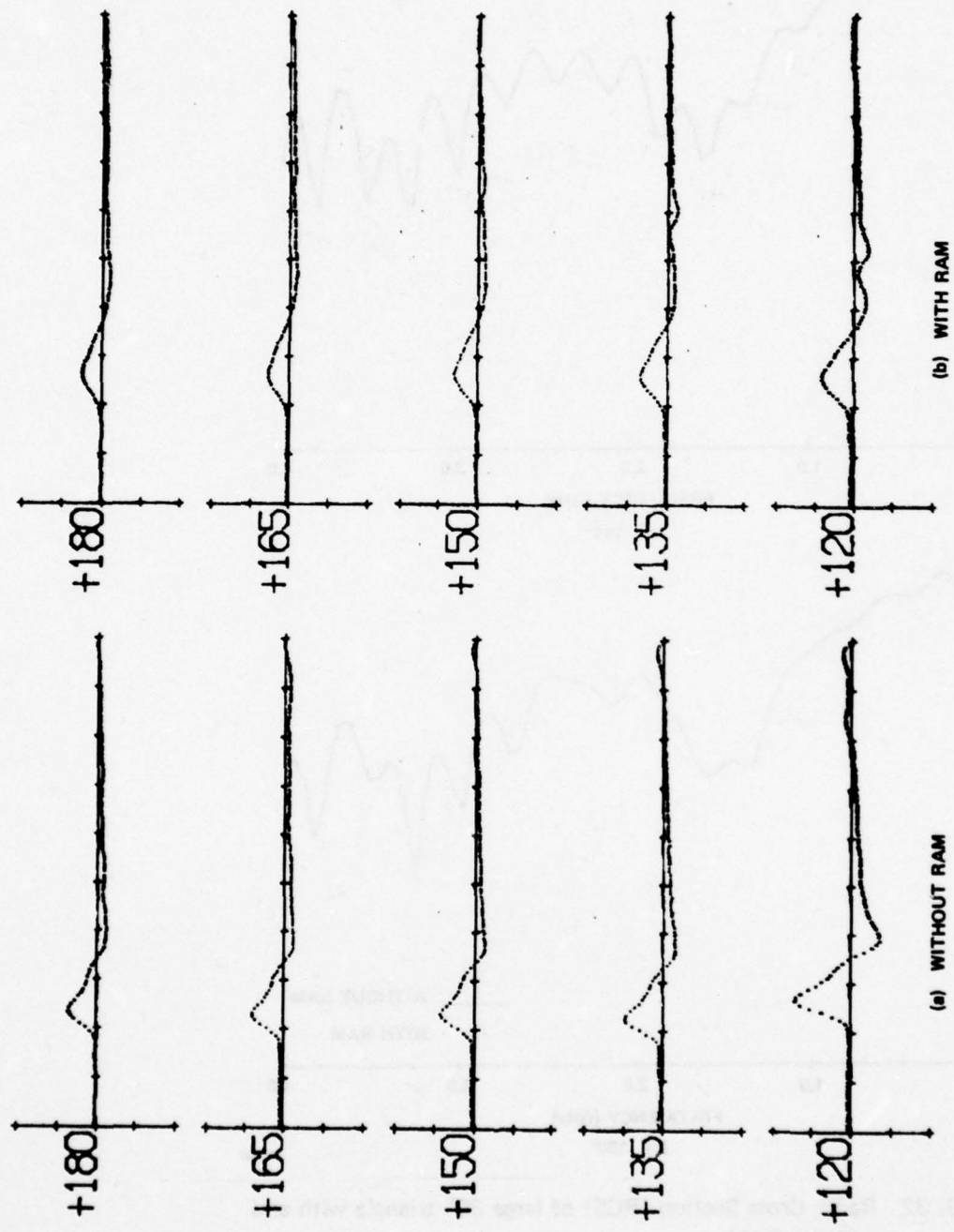
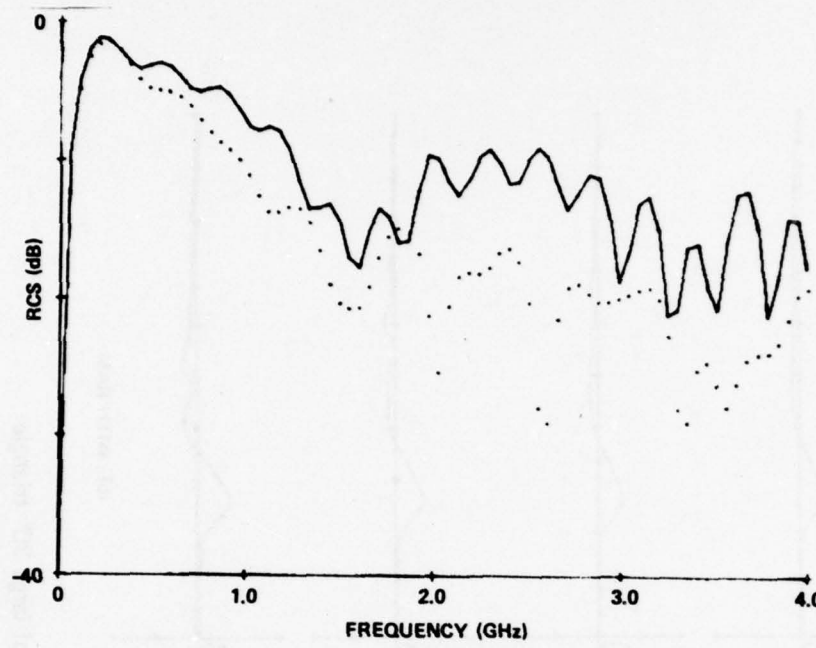
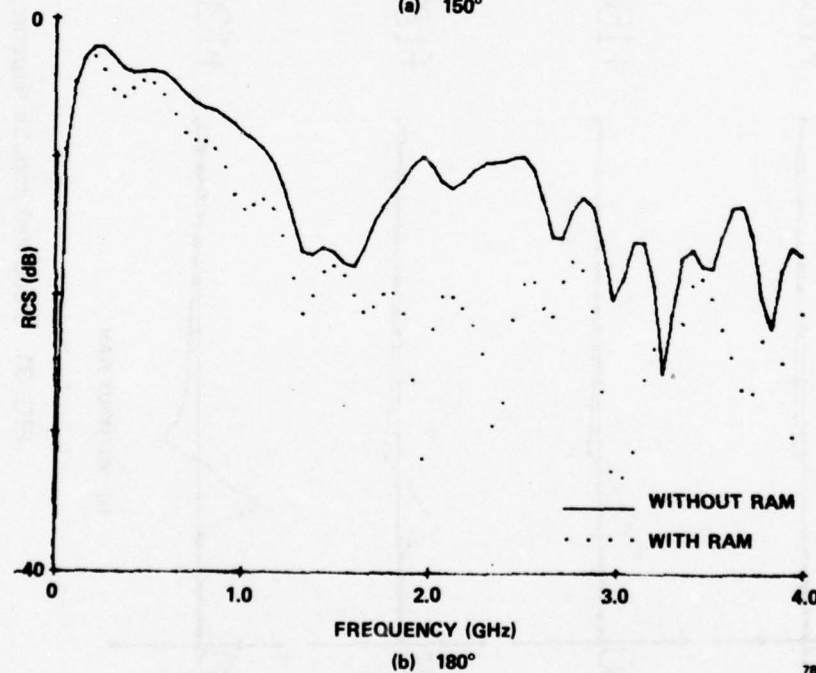


FIG. 31 Smoothed impulse response of large 30° triangle
(hor. scale: 0.5 ns/div.; vert. scale: 5 mV/div.).

78-307



(a) 150°



(b) 180°

78-308

FIG. 32 Radar Cross Section (RCS) of large 30° triangle with and without RAM.

target without RAM (the solid curve) is compared with the RCS of the target with RAM (the dotted curve). Note that for 150° incidence there is approximately 8 dB reduction in RCS between 2.0 and 2.9 GHz with narrow nulls which are down approximately 16 dB at 2.0 and 2.6 GHz. For 180° incidence there is approximately 10 dB reduction in RCS between 2.0 and 3.0 GHz, with narrow nulls which are down approximately 20 dB at 2.0, 2.4, and 3.0 GHz.

In Fig. 33 the measured smoothed impulse response of the large cylinder is displayed for aspect angles that range from 30° to 90° (broadside incidence). Results are shown for the naked cylinder and for a cylinder coated with Emerson & Cumings Eccosorb SF-2.5 RAM. The response in Fig. 33(a) for the clean target shows a scattering center return from the near edge at aspect angles of 30, 45, 60, and 75°. The positive pulse returns are all similar in size and shape. At 90°, however, the return approximates a smoothed $t^{-3/2}$ pseudo-function, as expected. When RAM is added to the vicinity of the scattering center, the response shown in Fig. 33(b) results. The major effects are a spreading, smoothing, and amplitude reduction of the smoothed impulse response of the uncoated RAM target.

Fig. 34 displays a comparison of the RCS in the frequency domain without and with RAM coating. For a 60° incidence angle the RCS is reduced approximately 10 dB between 1.2 GHz and 3.0 GHz by the RAM coating. Narrow nulls of approximately 20 dB reduction are also noted at approximately 1.5 GHz, 2.4 GHz, and 2.6 GHz. In Fig. 34(b) the comparison for broadside incidence is displayed. A reduction of approximately 20 dB is observed between 2.2 GHz and 2.9 GHz.

It is obvious from these measurements that direct time domain measurement of scattering center response provides a powerful tool in the broadside analysis of radar systems.

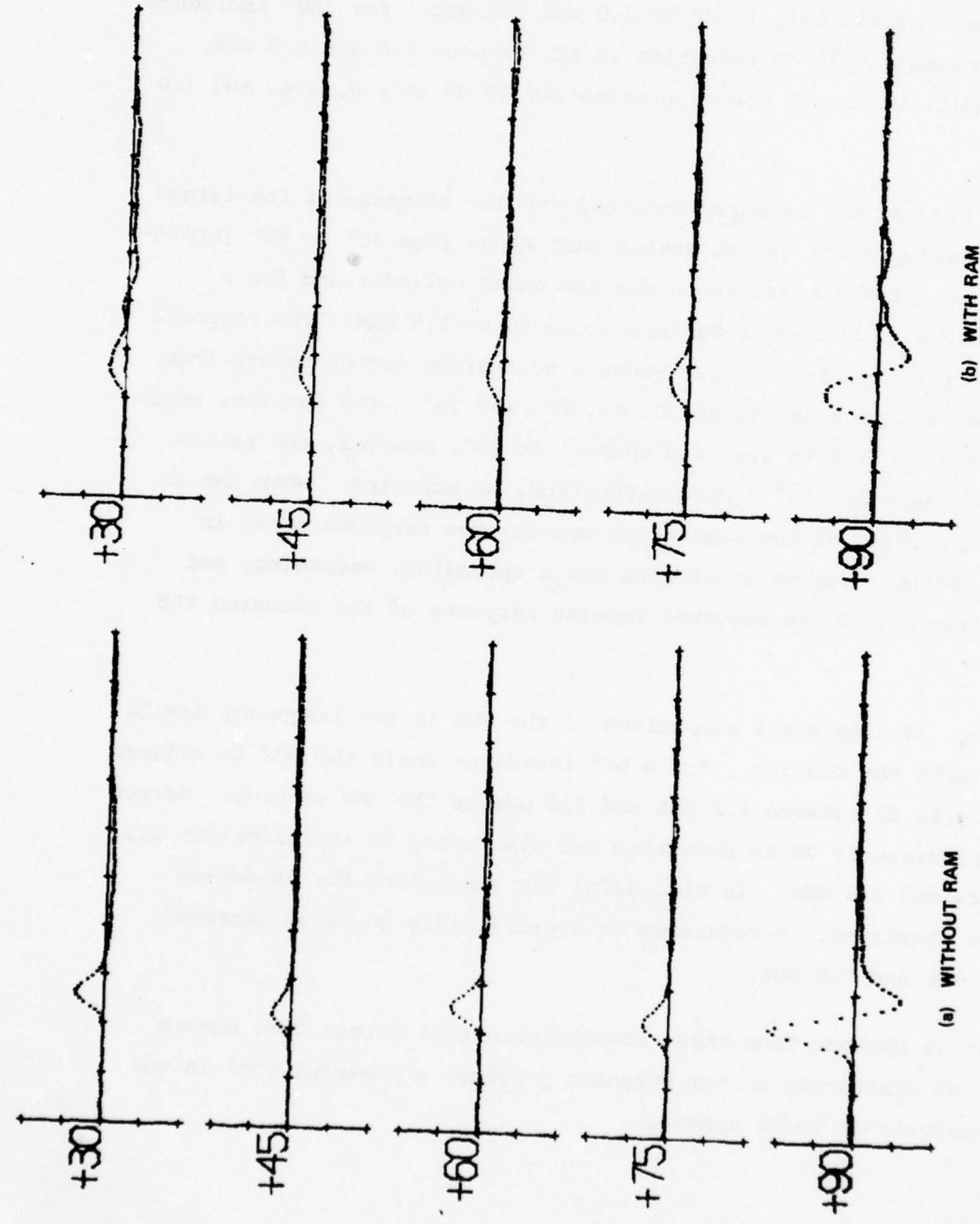
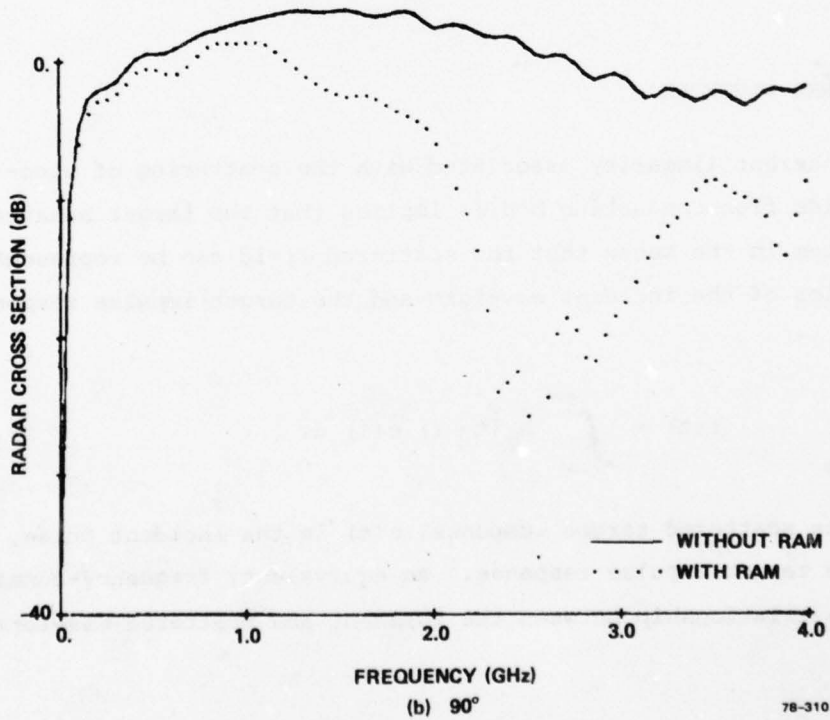
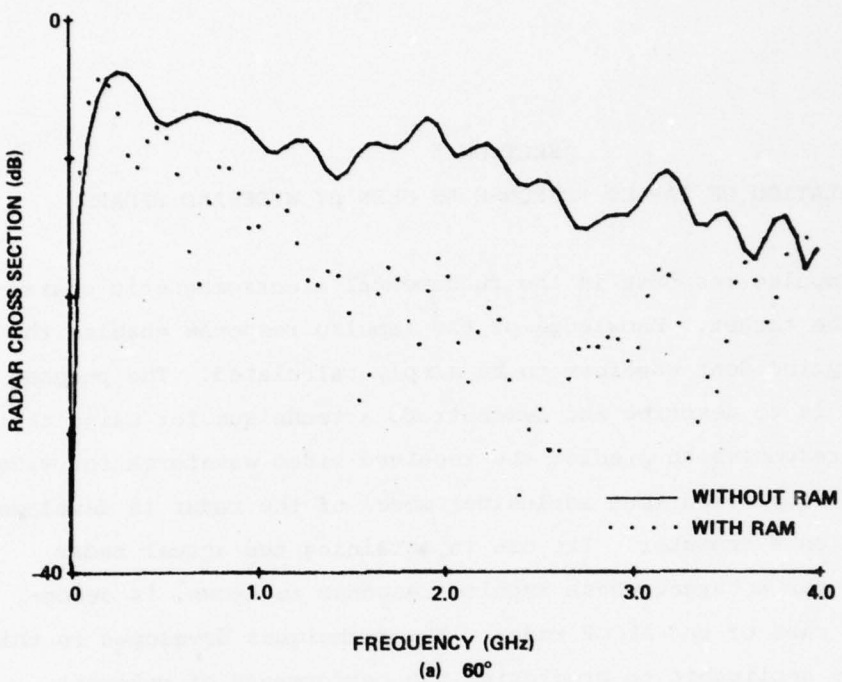


FIG. 33 Smoothed impulse response of large circular cylinder
 (hor. scale: 0.5 ns/div.; vert. scale: 5 mV/div.).

78-309



78-310

FIG. 34 Radar Cross Section of large cylinder with and without RAM.

SECTION 5

CALCULATION OF TARGET RESPONSE AS SEEN BY WIDEBAND RADARS

The impulse response is the fundamental electromagnetic characterization of the target. Knowledge of the impulse response enables the response for any incident waveform to be simply calculated. The purpose of this section is to describe and demonstrate a technique for using the target impulse responses to predict the received video waveforms for wideband radars. A simplified (but inclusive) model of the radar is developed and implemented on a computer. Its use in obtaining the actual radar video response, for a target whose impulse response is known, is demonstrated for the case of the ALCOR radar. The techniques developed in this section are also applicable to predicting the performance of coherent imaging systems.

5.1 BACKSCATTERED WAVEFORM

The inherent linearity associated with the scattering of electromagnetic fields from conducting bodies implies that the target behaves as a linear system in the sense that the scattered field can be represented as the convolution of the incident waveform and the target impulse response as follows:

$$r(t) = \int_{-\infty}^{+\infty} h_T(t-\tau) e(\tau) d\tau \quad (39)$$

where $r(t)$ is the scattered target response, $e(t)$ is the incident pulse, and $h_T(t)$ is the target impulse response. An equivalent, frequency-domain statement of the relationship between the incident and scattered waveforms is [8]

$$R(\omega) = H_T(\omega) E(\omega) \quad (40)$$

where R , H_T , and E are the Fourier transforms of r , h_T and e , respectively. This relationship clearly shows how the target acts as a linear filter on the incident signal.

5.2 COHERENT RADAR SIGNAL PROCESSING

Except for some scaling constants and delays which will be discussed later, equations (39) or (40) describe the waveform at the receiving antenna terminals of the radar.* Thus $e(t)$ is the input to the signal processing section of the radar.[†] The signal processing sections of most modern high-resolution radars are coherent, that is, they manipulate the phase as well as the amplitude of the received waveforms. For example, a very general model of the received waveform is

$$r(t) = b(t) \cos[\omega_0 t + \theta(t)] \quad (41)$$

where $b(t)$ and $\theta(t)$ are the amplitude and phase modulations of the carrier. A simple trigonometric identity shows that (41) is equivalent to

$$r(t) = [b(t) \cos \theta(t)] \cos \omega_0 t - [b(t) \sin \theta(t)] \sin \omega_0 t \quad (42)$$

which can be written

$$r(t) = \operatorname{Re} \left\{ [b(t) \cos \theta(t) + j b(t) \sin \theta(t)] e^{j \omega_0 t} \right\} \quad (43)$$

where Re denotes "real part of". Equations (42) or (43) show that the quantities in the rectangular brackets completely describe the received waveform in the sense that, if they are known, the RF waveform for a known carrier can be reconstructed by (42).

* This statement is true assuming the frequency response of the receiving antenna is flat over the bandwidth of the scattered waveform. If this is not true, then the frequency response of the antenna becomes an additional multiplicative term in (40).

† The effects of an IF section (if any) are unimportant to this discussion.

The slowly varying (relative to ω_0) time functions

$$\left. \begin{aligned} p(t) &= b(t) \cos \theta(t) \\ q(t) &= b(t) \sin \theta(t) \end{aligned} \right\} \quad (44)$$

are the so-called in-phase and in-quadrature components of the waveform relative to the carrier [9].

The p and q components of the received waveform can be obtained by the method of Figure 35. The filters pass the slowly varying p and q components but heavily attenuate all oscillations at much higher frequencies. The two outputs in Figure 35 are often called the baseband signal, bipolar video, the complex modulation, or the complex envelope. The latter terminology is descriptive because (43) can be written

$$\begin{aligned} r(t) &= \operatorname{Re} \left\{ [p(t) + j q(t)] e^{j \omega_0 t} \right\} \\ &= \operatorname{Re} \left\{ \tilde{r}(t) e^{j \omega_0 t} \right\} \end{aligned} \quad (45)$$

where

$$\tilde{r}(t) = p(t) + j q(t) = b(t) e^{j \theta(t)} \quad (46)$$

The elaboration of the preceding paragraphs is intended to show that all the important, or information-bearing, characteristics of typical radar signals are contained in the p and q components or the complex envelope. It is then to be expected that the signal processor must deal only with the complex envelope.

5.3 COMPLEX ENVELOPE OF THE RETURN SIGNAL

A general expression for the pulse applied to the terminals of the transmitting antenna is

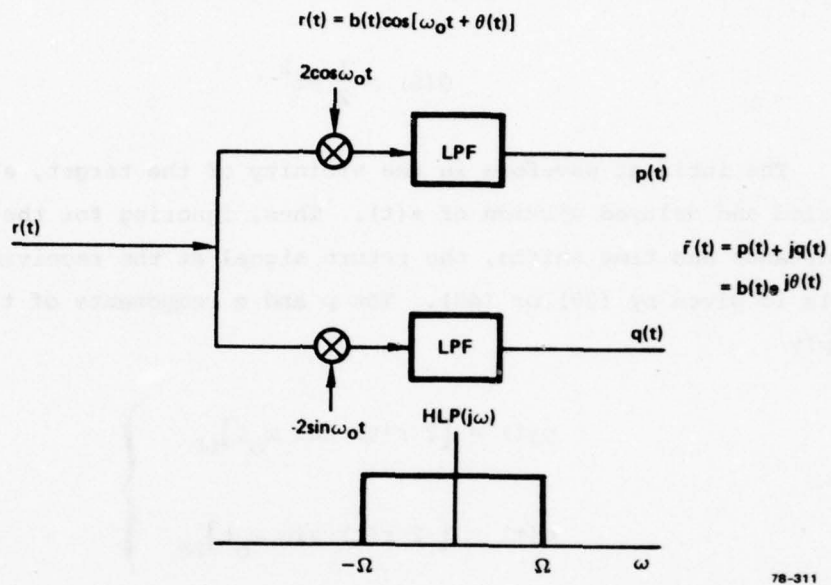


FIG. 35 Radar Receiver processing for p and q (or complex envelope) generation.

$$s(t) = a(t) \cos[\omega_0 t + \psi(t)] \quad (47)$$

where $a(t)$ and $\psi(t)$ are the amplitude and phase modulations impressed on the RF carrier. For example, for a linear FM or chirp pulse,

$$\psi(t) = \frac{1}{2} \beta t^2 \quad (48)$$

The incident waveform in the vicinity of the target, $e(t)$, will be a scaled and delayed version of $s(t)$. Thus, ignoring for the moment some constants and time shifts, the return signal at the receiving antenna terminals is given by (39) or (40). The p and q components of this signal are simply

$$\left. \begin{aligned} p(t) &= [2 r(t) \cos \omega_0 t]_{LP} \\ q(t) &= [-2 r(t) \sin \omega_0 t]_{LP} \end{aligned} \right\} \quad (49)$$

where the subscript LP means "low pass filtered version of" the quantities in the brackets [10]. Using some simple properties of Fourier transforms and some careful algebra, it can be shown that the Fourier transform of the complex envelope (or p and q components) of the received signal is given by

$$\tilde{R}(\omega) = P(\omega) + jQ(\omega) = F[\tilde{r}(t)] = H_T(\omega + \omega_0) \tilde{S}(\omega) \quad (50)$$

where $\tilde{S}(\omega)$ is the Fourier transform of the complex envelope, $\tilde{s}(t)$, of the signal and H_T is the Fourier transform of the target impulse response. Note that the tilde notation indicates a complex or baseband function of time or frequency. Equation (50) shows that the bipolar video return signal (complex envelope) is influenced by the target frequency response in a band centered about the radar carrier as expected. The width of this band is the bandwidth of the transmitted pulse. The returns from wider band transmitted pulses will contain more information about the target

than those from narrower band pulses.

5.4 MATCHED FILTERING AND PULSE COMPRESSION

The full range resolution and detection sensitivity of a radar are obtained by appropriately filtering the received waveform. The matched filter maximizes the output signal to noise ratio (detection) and time compresses phase modulated signals (range resolution). Since the time (or range) sidelobes in the matched filter output are often unacceptably high, exact matched filtering is often not done in practical receivers. In this section, however, we consider matched filtering and pulse compression to be identical operations. In addition, the term matched filtering here means matched to the transmitted signal in white noise, that is, the target is assumed to be an ideal sphere whose radius is much larger than the radar wavelength so that it is illuminated only in the optical region. Note that for target classification, filtering which is matched to the expected return from each different class of extended target would be useful.

In view of the dominant role played by the complex envelope, it is perhaps not surprising that matched filtering can be done in the video section. Figure 36 is a block diagram of the pulse compression receiver assumed in this report. The frequency response of the matched filter is

$$\tilde{H}_{MF}(\omega) = K \tilde{S}^*(\omega) \quad (51)$$

where \tilde{S}^* is the Fourier transform of the complex envelope of the transmitted pulse [10, p. 245] and K is a constant. The Fourier transform of the compressed complex video, $\tilde{r}_c(t)$, is then

$$\tilde{R}_c(\omega) = K H_T(\omega + \omega_0) |\tilde{S}(\omega)|^2 \quad (52)$$

which follows from (50) and (51).

The last equation is the main result of this section. The compressed video return $\tilde{r}_c(t)$ is obtained by taking the inverse Fourier transform of (52). Linear video A-scope traces are then simply

$$v(t) = |\tilde{r}_c(t)| \quad (53)$$

as shown in Figure 36.

The following subsections describe the method used to include noise and scale the A-scope plots so that they are physically descriptive of an ALCOR situation. Several examples are discussed in the final subsections.

5.5 SCALING VIA THE RADAR EQUATION

In this subsection, the constants and delays neglected above are included in order to present the video output in physically descriptive units. The system to be analyzed is shown in Figure 37. This analysis is basically a derivation of the radar range equation [11] and the somewhat tedious details will not be given.

It can be shown that the complex video before pulse compression is approximately given by

$$\tilde{R}(\omega) = \frac{G\lambda_0}{(4\pi R)^2} [R_0 H_T(\omega + \omega_0; R_0)] \tilde{S}(\omega) e^{-j \frac{\omega R}{c}} \quad (54)$$

if we neglect the small variation of antenna gain and effective aperture over the pulse bandwidth. R_0 is the reference range for measuring the target response.* For the idealized target case, (54) in the time domain is

$$\tilde{r}(t) = \frac{G\lambda_0}{(4\pi R)^2} \sqrt{\frac{\sigma}{4\pi}} \tilde{s}\left(t - \frac{2R}{c}\right) \quad (55)$$

* This is discussed further in Section 5.7.

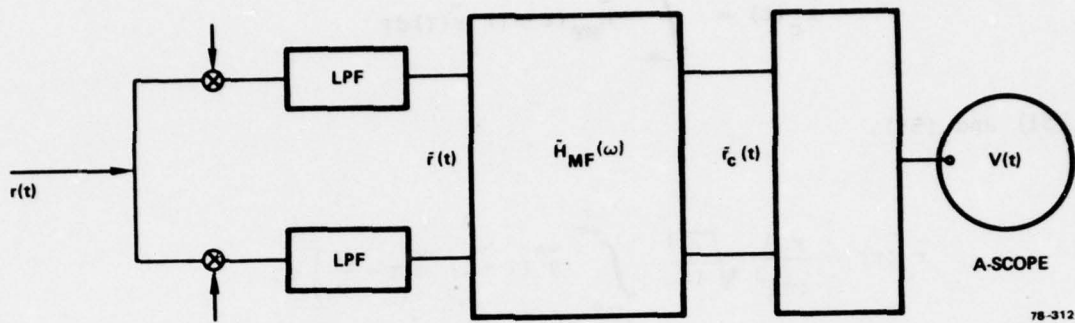


FIG. 36 Pulse compression by complex video matched filtering.

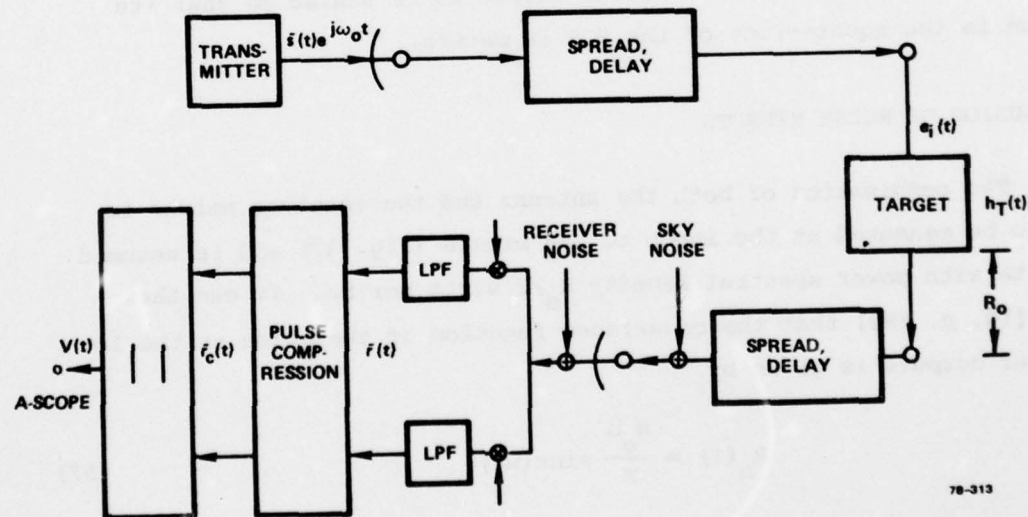


FIG. 37 Block diagram of radar system operation.

where σ is the target RCS. In this case, the compressed complex video is

$$\tilde{r}_c(t) = \int_{-\infty}^{+\infty} \tilde{h}_{MF}(t-\tau) \tilde{r}(\tau) d\tau$$

Using (51) and (55),

$$\tilde{r}_c(t) = \frac{KG\lambda}{4\pi R^2} \sqrt{\frac{\sigma}{4\pi}} \int_{-\infty}^{+\infty} \tilde{s}^*(\tau-t) \tilde{s}\left(\tau - \frac{2R}{c}\right) d\tau$$

from which an application of the Schwartz inequality [8] gives the peak matched filter output

$$\max_t |\tilde{r}_c(t)| = \frac{KG\lambda}{4\pi R^2} \sqrt{\frac{\sigma}{4\pi}} E_T \quad (56)$$

where E_T is the pulse energy measured at the transmitting antenna terminals. This equation allows the matched filter output to be scaled so that its peak value is the square-root of the RCS in meters.

5.6 INCLUSION OF NOISE EFFECTS

The combination of both the antenna and the receiver noises is assumed to be measured at the input to the mixers (Fig. 37) and is assumed to be white with power spectral density $N_o/2$ watts per Hz. It can then be shown [10, p. 582] that the covariance function of the noise at the low pass filter outputs is given by

$$R_n(\tau) = \frac{N_o \Omega}{\pi} \operatorname{sinc}(\Omega\tau) \quad (57)$$

where Ω is the radian cutoff frequency of the ideal low pass filters.

From this, it follows that the covariance function of the complex* noise before matched filtering, $\tilde{n}(t)$, is

$$\tilde{R}_{\tilde{n}}(\tau) = \frac{2N_0\Omega}{\pi} \operatorname{sinc}(\Omega\tau) \quad (58)$$

which has a rectangular power spectrum of level $2N_0$ extending from $-\Omega$ to $+\Omega$ radians per second.

If the matched filter bandwidth is smaller than the low pass filter bandwidth, the power spectral density of the compressed noise is approximately

$$\begin{aligned} \tilde{S}_{\tilde{n}_c}(\omega) &= 2N_0 |\tilde{H}_{MF}(\omega)|^2 \\ &= 2N_0 K^2 |\tilde{S}(\omega)|^2 \end{aligned} \quad (59)$$

where the last equality follows from (51). The variance of the compressed complex noise is simply the total area under the spectrum (59) which is

$$\operatorname{Var}[\tilde{n}_c(t)] = \overline{\tilde{n}_c(t) \tilde{n}_c^*(t)} = 2N_0 K^2 E_T \quad (60)$$

where the overbar denotes statistical average and E_T is the pulse energy at the transmitter terminals

The peak signal to noise ratio at the output of the matched filter for an ideal target is then [11, p. 144]

* As with signals, resorting to complex noise is merely a convenient way of simultaneously treating the quadrature components.

$$\text{peak SNR} = \frac{\max_t |\tilde{r}_c(t)|^2}{|\tilde{n}_c(t)|^2} = \frac{G^2 \lambda^2 \sigma}{(4\pi)^3 R^4} \left(\frac{E_T}{2N_0} \right) \quad (61)$$

which follows from (56) and (60). This is, of course, the noise-limited radar range equation.

The specific examples in the following sections were computed using the inverse Fourier transform of (52). The amplitude scaling of the A-scope traces was done using (56) so that the peak linear video levels have the units of meters (square root of RCS). The noise levels were set using equation (61) for a one square meter target. The results in the following sections give this SNR which is equivalent to specifying the range. For example, a 12 dB SNR on a one square meter target corresponds to the ALCOR range of about 2000 km [12].

5.7 EXAMPLE: IDEALIZED TWO-ELEMENT TARGET

The following simple example will illustrate the ideas of the previous subsections. Assume that the transmitted pulse has the wideband ALCOR [12] parameters of 10 μ sec duration and 500 MHz bandwidth. The target is assumed to be two spheres separated by 10 meters. The sphere nearest the radar has an RCS, σ_1 , of 9 square meters. The other scattering center has $\sigma_2 = 1$.

In order to properly evaluate the inverse Fourier transform of a scaled version of (52), the target frequency response function must be obtained. For this simple target, the result is

$$H_T(\omega; R_0) = \frac{1}{R_0} \left\{ \sqrt{\frac{\sigma_1}{4\pi}} e^{j \frac{\omega L}{c}} + \sqrt{\frac{\sigma_2}{4\pi}} e^{-j \frac{\omega L}{c}} \right\} \quad (62)$$

where H_T relates the incident field to the scattered field at reference range R_0 and L is the distance between the scattering centers. Note that

the reference range cancels out of the properly scaled equation (54).

Figure 38(a) shows the, pulse compressed, scaled, linear video $|\tilde{r}_c(t)|$ for SNR = 20 dB (the target is roughly 1300 km from ALCOR). The time axis is converted to range by

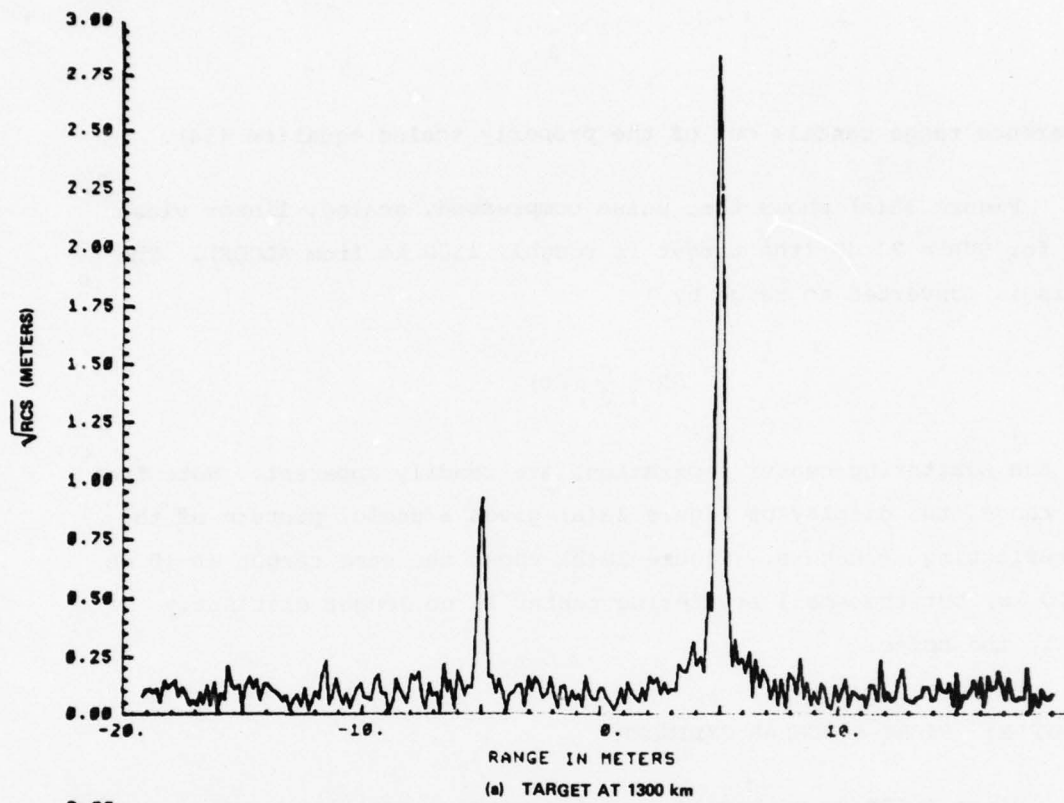
$$\Delta R = \frac{c}{2} (\Delta t)$$

so that the scattering center separations are readily apparent. Note that at this range, the display of Figure 38(a) gives a useful picture of the target reflecting structure. Figure 38(b) shows the same target at 10 dB SNR (2100 km) but the small scattering center is no longer distinctly visible in the noise.

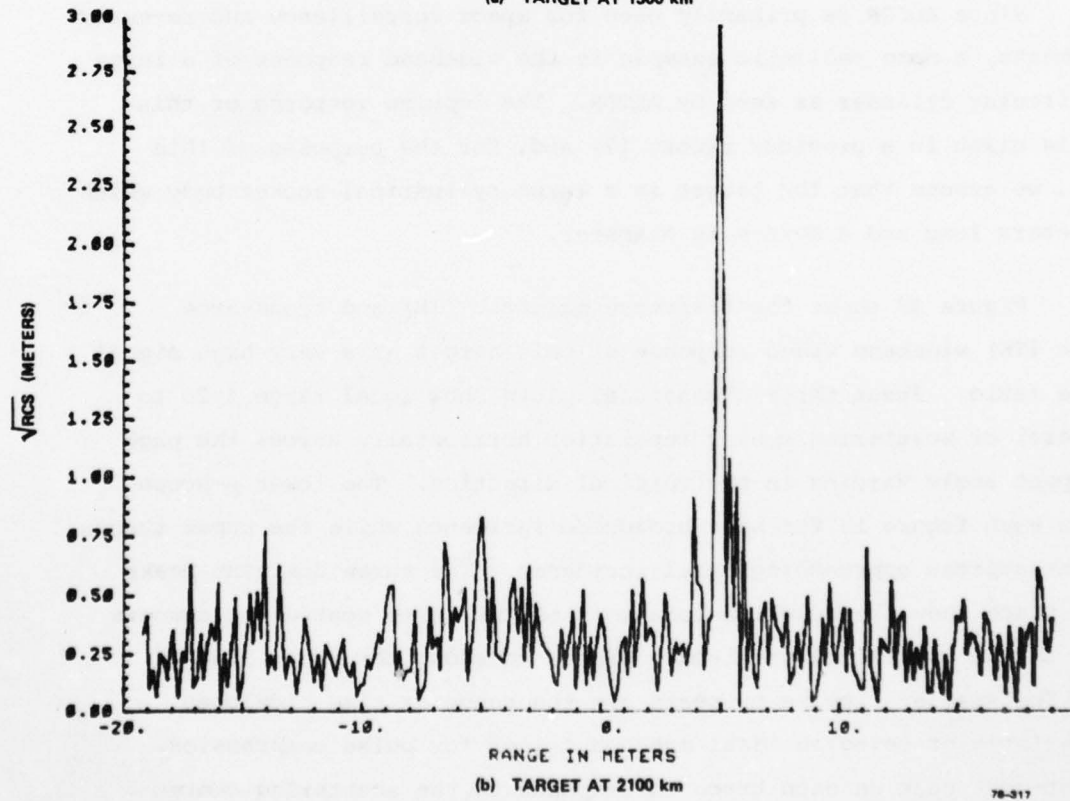
5.8 EXAMPLE: RIGHT CIRCULAR CYLINDER

Since ALCOR is primarily used for space surveillance and re-entry measurements, a more realistic example is the wideband response of a large right circular cylinder as seen by ALCOR. The impulse response of this target is given in a previous report [7] and, for the purposes of this example, we assume that the target is a large cylindrical rocket body which is 20 meters long and 4 meters in diameter.

Figure 39 shows the tranverse magnetic (TM) and transverse electric (TE) wideband video response of this target at a very high signal to noise ratio. These three dimensional plots show local range (-20 to +20 meters) or scattering center separation horizontally across the page with aspect angle varying in the vertical direction. The lower A-scope trace in each figure is for near broadside incidence while the upper traces represent aspects approaching axial incidence. The three dominant peaks in each trace show the relative locations of the three scattering centers as well as the overall target length projected along the radar line of sight. The smaller ripples or peaks are the range or time sidelobes characteristic of using an ideal matched filter for pulse compression. The right-most peak on each trace corresponds to the scattering center



(a) TARGET AT 1300 km



(b) TARGET AT 2100 km

78-317

FIG. 38 ALCOR linear video (\sqrt{RCS}) return from two element target.

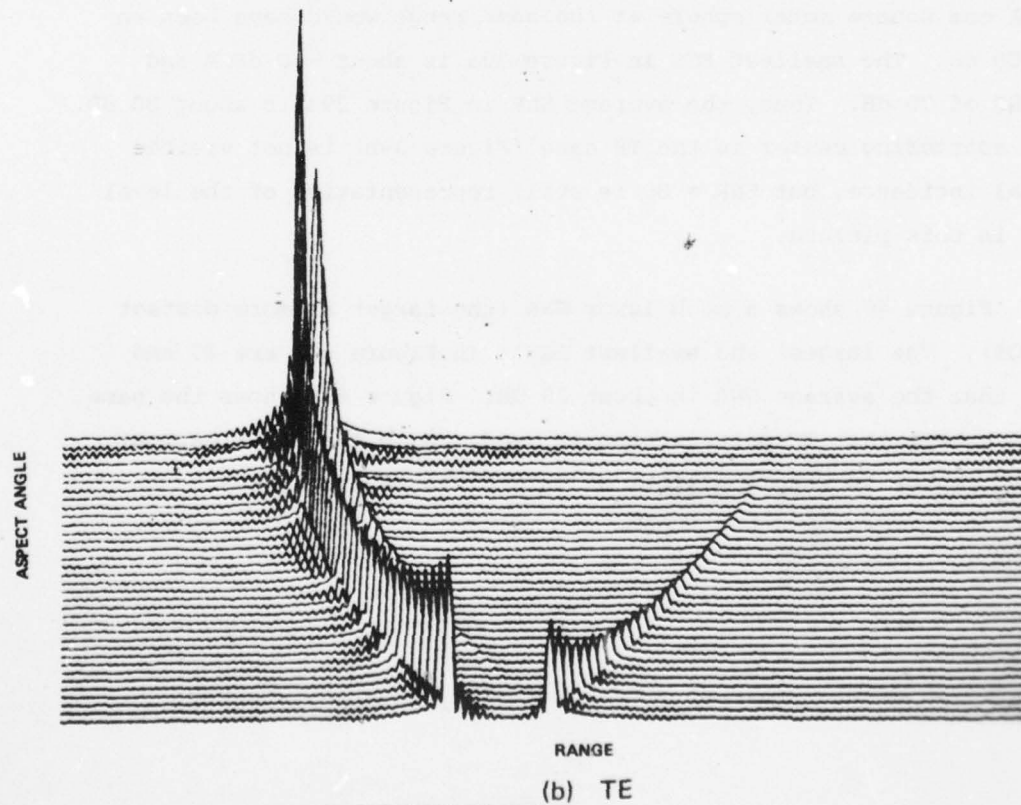
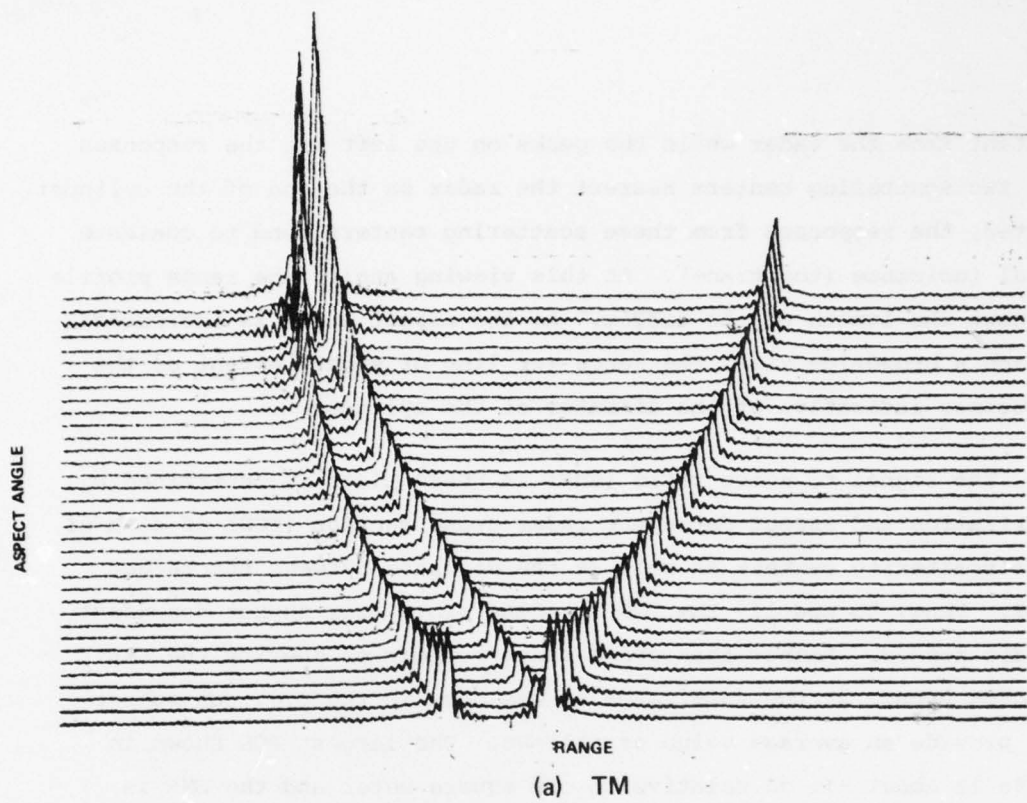


FIG. 39 ALCOR video return from a cylinder (average S/N = 80 dB).

AD-A068 211

SPERRY RESEARCH CENTER SUDBURY MASS
LOW EM SIGNATURE RESPONSE TECHNIQUES. (U)

F/G 17/9

MAR 79 C L BENNETT, H MIERAS, S L TEETER
SCRC-CR-78-61

F30602-77-C-0166

UNCLASSIFIED

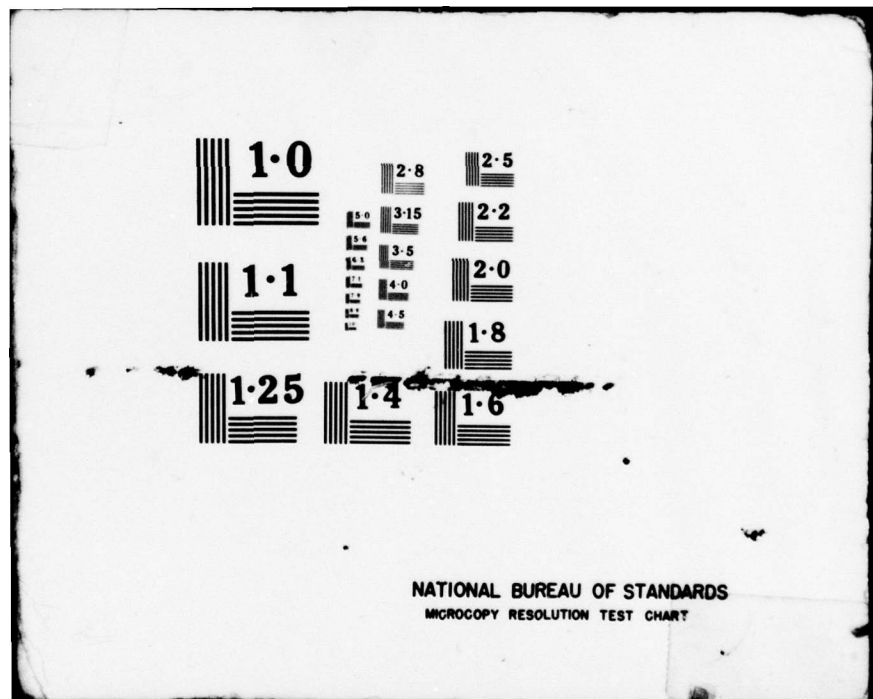
RADC-TR-78-287

NL

2 OF 2
ADA
068211



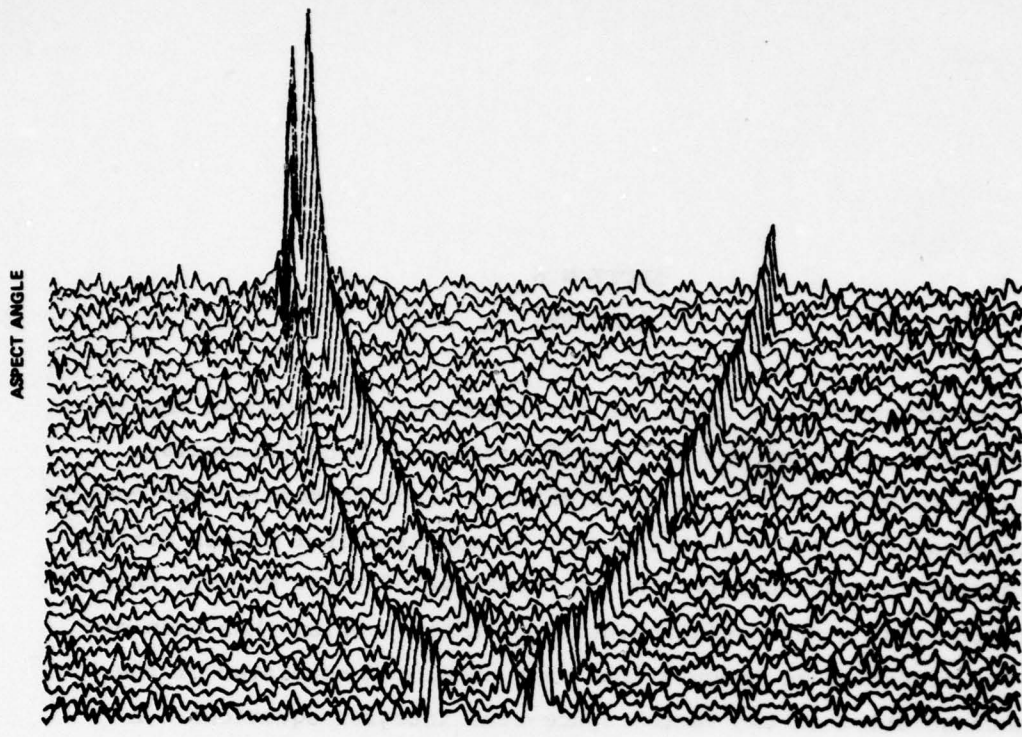
END
DATE
FILED
6-79
DDC



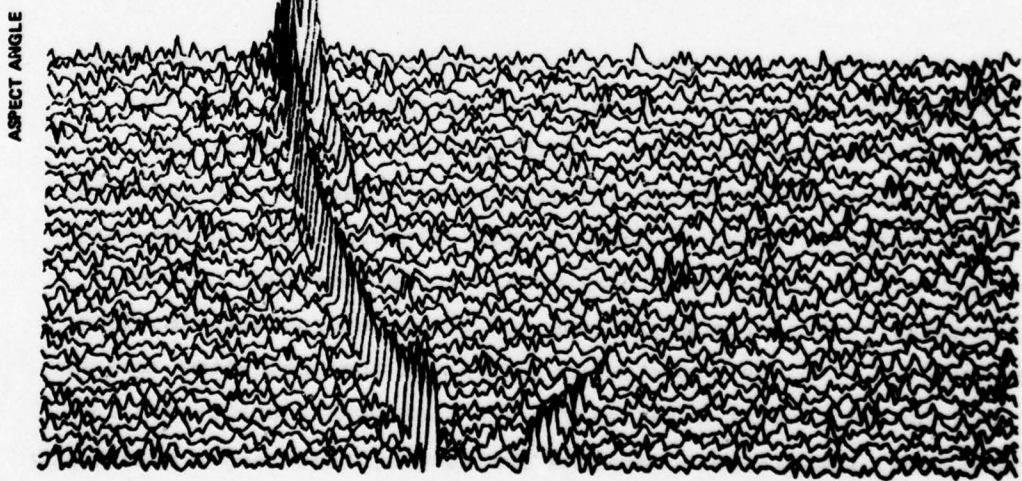
most distant from the radar while the peaks on the left are the responses from the two scattering centers nearest the radar on the end of the cylinder. As expected, the responses from these scattering centers tend to coalesce near axial incidence (top trace). At this viewing angle, the range profile extent shows the length of the target. As the aspect angle is increased to approach a broadside view, the range (or line of sight) extent of the target becomes indicative of the diameter of the cylinder.

The signal to noise ratio (SNR) in these plots is determined by the polarization and aspect-dependent radar cross section (RCS) of each of the three scattering centers as well as the distance between the target and ALCOR. Thus, to specify the SNR in these plots, six aspect dependent numbers are needed. Rather than quote these numbers or specify the SNR for a 0 dB_{SM} sphere at the same range as was done in the previous subsection, we provide an average value as follows. The largest RCS shown in Figure 39a is about -11 dB relative to one square meter and the SNR is 89 dB. A one square meter sphere at the same range would have been an SNR of 100 dB. The smallest RCS in Figure 39a is about -30 dB_{SM} and has an SNR of 70 dB. Thus, the average SNR in Figure 39a is about 80 dB. The rear scattering center in the TE case (Figure 39b) is not visible near axial incidence, but SNR = 80 is still representative of the level of noise in this picture.

Figure 40 shows a much lower SNR (the target is more distant from ALCOR). The largest and smallest SNR's in Figure 40a are 29 and 10 dB so that the average SNR is about 20 dB. Figure 40b shows the same situation except that TE polarization is used. Note that the rearmost scattering center is barely visible at this distance from ALCOR.



(a) TM



(b) TE

FIG. 40 ALCOR video return from a cylinder (average S/N = 20 dB).

78-315

SECTION 6

SUMMARY

In this study the technique for computing the smoothed impulse response has been extended to the case of scattering from triangular plates, quadrilateral plates, and more refined aircraft models that consist of a cylindrical fuselage with triangular or quadrilateral plates for the wings, stabilizers, and rudder. To the knowledge of these writers this is the first time that a successful solution of these problems has been obtained. The numerical techniques that were developed consisted of the simultaneous solution of two vector space-time integral equations. A major effort was required in order to be able to handle non-rectangular plate geometries. The resulting numerical procedure consisted of a set of local coordinate transformations in the plate edge regions in order to be able to properly satisfy the boundary conditions on the surface currents. Results were computed for several triangular plates, finned cylinders, and a MIG-21 aircraft model. These results were found to be in good agreement with measurements taken on the Sperry time domain scattering range.

At high frequencies where the characteristic target dimensions are many wavelengths, the target response is due to returns from only local regions of the target surface. These regions occur where the derivatives of the surface tangent are discontinuous and are referred to as scattering centers. They, in turn, produce singularities in the target impulse response. In this effort time domain techniques that utilize the local nature, both in space and time, of these returns were developed and demonstrated. Both the numerical solution via the space-time integral equation and the measurement solution via the time domain scattering range were carried out. Results were obtained for several test target scattering centers. The power of this time domain approach to target response prediction can not be overemphasized. It provides an efficient analytical and measurement capability for obtaining accurately the response of large

targets. In addition measured results were obtained for the response of scattering centers when coated with RAM. These results show that RAM can indeed lower the scattered response but that the amount of reduction is dependent upon the spectrum of the illumination and the aspect angle. Moreover, there were several frequencies where the RCS experienced nulls of an additional 8-10 dB.

The outstanding achievement of this work has been the development of general techniques for computing the wideband (or impulse) response of realistic targets with a highly efficient and accurate method of computing the noise-corrupted, pulse-compressed video response of these targets when illuminated by a wideband radar. In particular the application of some subtle properties of the discrete Fourier transform enabled the calculation of transforms of large time-bandwidth product waveforms (such as 5000) using an FFT with less than one-tenth the number of points. These techniques were demonstrated using a model of the ALCOR radar.

SECTION 7

REFERENCES

1. C.L. Bennett, R. Hieronymus, H. Mieras, "Impulse Response Target Study," SCRC, Final Report on Contract No. F30602-76-C-0209, May 1977.
2. C.L. Bennett, J.D. DeLorenzo, A.M. Auckenthaler, "Integral Equation Approach to Wideband Inverse Scattering," SCRC, Sudbury, MA, Final Report on Contract No. F30602-69-C-0332, June 1970.
3. C.L. Bennett, K.S. Menger, R. Hieronymus, "Space-Time Integral Equation Approach for Targets with Edges," SCRC, Sudbury, MA, Final Report on Contract No. F30602-73-C-0214, May 1974.
4. C.L. Bennett, R.M. Hieronymus, D. Peterson, "Space-Time Integral Equation Approach to Targets with Fins," SCRC, Sudbury, MA, Final Report on Contract No. F30602-75-C-0040, November 1975.
5. C.L. Bennett, A.M. Auckenthaler, R.S. Smith, J.D. DeLorenzo, "Space-Time Integral Equation Approach to the Large Body Scattering Problem," SCRC, Final Report on Contract No. F30602-71-C-0162, May 1973.
6. R.S. Smith, J.D. DeLorenzo, C.L. Bennett, "Measurements of and Discrimination with Smoothed Impulse Responses of Radar Targets," Sperry Research Center, Sudbury, MA, Interaction Note 232, November 1970.
7. C.L. Bennett and R.M. Hieronymus, "Integral Equation Solution," Sperry Research Center, Sudbury, MA, Final Report on Contract No. F30602-75-C-0040, March 1976.
8. A. Papoulis, The Fourier Integral, McGraw-Hill, 1962.
9. M.I. Skolnik (ed), Radar Handbook, McGraw-Hill, 1970, p. 3-6.
10. H.L. VanTrees, Detection, Estimation, and Modulation Theory, Part III, Wiley, 1971, p. 567.
11. J.V. DiFranco and W.L. Rubin, Radar Detection, Prentice Hall, 1968, p. 448.
12. Kwajalein Missile Range Instrumentation and Support Facilities Manual, USABMDSC, 15 January 1976 (Revision H), Figure 5c-4.
13. Kenneth H. Huebner, "The Finite Element Method for Engineers," J. Wiley & Sons, 1975.

SECTION 8
APPENDICES

8.1 SELF-PATCH INTEGRATION AT EDGE

We need to find the integral over the self-patch

$$\vec{A}_S(\vec{r}_e, t) = \frac{1}{4\pi} \int_S \frac{\vec{J}(\vec{r}', \tau) dS'}{R}, \quad \tau = t - R \quad (8-1)$$

as used in Section 2.3.2, where \vec{r}_e is a node on the edge; and also

$$\vec{J}^{\text{eff}}(\vec{r}_e, t) = \frac{1}{\Delta S_e} \int_S \vec{J}(\vec{r}', \tau) dS' \quad (8-2)$$

We assume a semicircular patch of radius ρ centered at \vec{r}_e and assign a local coordinate system ζ, η, \parallel and \perp to the edge. See Figure 41.

Note that $\Delta S_e = \pi/2 \rho^2$ or $\rho = \sqrt{2\Delta S_e/\pi}$. There is a reference node at \vec{r}_o , which is separated from \vec{r}_e by the perpendicular distance d . Also, $dS' = \rho' d\rho' d\phi$ and $R = \rho'$. In general, \vec{J} cannot be assumed to be constant over the patch, but must satisfy the edge conditions (11). Perform the integration by components (\parallel or \perp).

(a) J is constant.

This condition can be assumed to hold for J_{\perp} at a bound edge, where the boundary condition is $\partial J_{\perp} / \partial \eta = 0$. Then simply:

$$J^{\text{eff}}(\vec{r}_e, t) = J_o \quad (8-3)$$

and

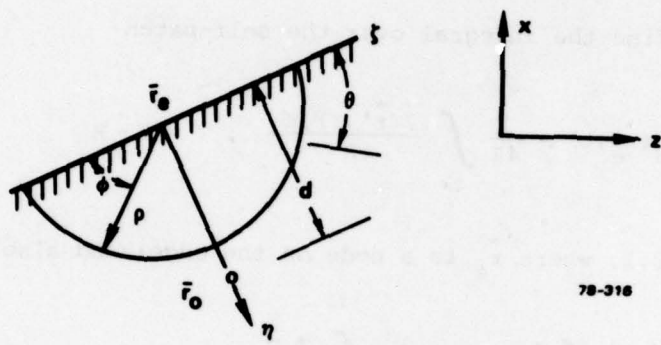


FIG. 41 Edge integration.

$$A_S(\vec{r}_e, t) = \frac{J_o}{4\pi} \int_0^{\rho} \frac{\rho' d\rho'}{\rho'} \int_0^{\pi} d\phi = \frac{J_o \rho}{4} = \frac{1}{4} \sqrt{\frac{2\Delta S_e}{\pi}} J_o \quad (8-4)$$

where J_o is the value at the reference point (\vec{r}_o, t) .

(b) $J = 0$ at edge.

This condition holds for J_1 at a free space edge. Assume $J(\eta) = \eta/d J_o$ and that there is no variation of J in the direction ζ . Using $\eta = \rho' \sin \phi$:

$$J^{eff}(\vec{r}_e, t) = \frac{J_o}{d \Delta S_e} \int_0^{\rho} \rho'^2 d\rho' \int_0^{\pi} \sin \phi d\phi = \frac{J_o}{d \Delta S_e} \left(\frac{\rho^3}{3}\right) (2)$$

$$J^{eff}(\vec{r}_e, t) = \frac{4}{3\pi d} \sqrt{\frac{2\Delta S_e}{\pi}} J_o. \quad (8-5)$$

Similarly

$$A_S(\vec{r}_e, t) = \frac{J_o}{4\pi d} \int_0^{\rho} \rho' d\rho' \int_0^{\pi} \sin \phi d\phi = \frac{(2\Delta S_e/\pi)}{4\pi d} J_o$$

We will write this as

$$A_S(\vec{r}_e, t) = \frac{3}{16} \sqrt{\frac{2\Delta S_e}{\pi}} J^{eff}(\vec{r}_e, t) \quad (8-6)$$

[The condition $J=0$ is also satisfied by the \parallel component at a bound or symmetry edge. For this case we prefer to set $J^{eff} = 0$ and $A_S = 0$, since the image of the self patch has currents with opposite sign in the parallel component.] The effective current is close to zero and its exact value does not matter much.

$$(c) J \sim \sqrt{\frac{1}{\eta}} \text{ at edge.}$$

This condition holds for the parallel components at a free edge.

Assuming no variation in the ζ direction

$$J(\eta) = \sqrt{\frac{d}{\eta}} J_0 \rightarrow \infty \text{ as } \eta \rightarrow 0.$$

Using $\eta = \rho' \sin \phi$,

$$\begin{aligned} J^{\text{eff}}(\vec{r}_e, t) &= \frac{J_0 \sqrt{d}}{\Delta S_e} \int_0^{\rho'} \sqrt{\rho'} d\rho' \int_0^{\pi} \frac{d\phi}{\sqrt{\sin \phi}} \\ &= \frac{J_0 \sqrt{d}}{\Delta S_e} \left(\frac{2}{3} \rho'^{3/2} \right) \left(\sqrt{\pi} \frac{\Gamma(1/4)}{\Gamma(3/4)} \right) \end{aligned}$$

or

$$J^{\text{eff}}(\vec{r}_e, t) = \frac{\sqrt{d}}{(2\Delta S_e/\pi)^{\frac{1}{4}}} \frac{4}{3\sqrt{\pi}} \frac{\Gamma(1/4)}{\Gamma(3/4)} J_0 \quad (8-7)$$

where

$$\frac{\Gamma(1/4)}{\Gamma(3/4)} = 2.959.$$

Similarly obtain

$$A_S = \frac{\sqrt{d} (2\Delta S_e/\pi)^{\frac{1}{4}}}{2\sqrt{\pi}} \frac{\Gamma(1/4)}{\Gamma(3/4)} J_0$$

Write this as

$$A_S(\vec{r}_e, t) = \frac{3}{8} \sqrt{\frac{2\Delta S_e}{\pi}} J^{\text{eff}}(\vec{r}_e, t) \quad (8-8)$$

These results are summarized in (26) and (29).

8.2 FINITE ELEMENT TECHNIQUE

The following is an adaptation of the methods presented in [13] and elsewhere.

We wish to solve the differential equation

$$f(\vec{A}) = \left[\nabla(\nabla \cdot \vec{A}) - \frac{\partial^2 \vec{A}}{\partial t^2} \right]_{\tan} + \epsilon \frac{\partial \vec{A}}{\partial t} \tan = 0 \quad (8-9)$$

on the surface (here contained in the x, z plane), subject to boundary conditions on \vec{J} , where

$$\vec{A}(\vec{r}, t) = \frac{1}{4\pi} \int_S \frac{\vec{J}(\vec{r}', t)}{R} dS' \quad (8-10)$$

$\tau = t - R$

The finite element method proceeds by dividing the surface into elements of arbitrary size and shape with a certain number of nodes on the boundary of the element. Here we will assume that 3 nodes define the element, i.e. the elements are triangles. It is readily seen that each node on the surface usually belongs to 6 triangles for a more or less regular (e.g. hexagonal) tessellation of the surface. The use of 3 nodes per element will result in \vec{A} continuous to first derivatives across element boundaries. (For higher order continuity, more nodes per element would need to be used.)

On the element (e) we can approximate \vec{A} in terms of node values:

$$\vec{A}^e(t) = \sum_j N_j^e(x, z) \vec{A}_j(t), \quad (8-11)$$

where N_j are simple interpolating functions, and where the summation is over the 3 nodes of element (e). Note that time and space variation has

been separated in this expression.

$$N_i^e(x, z) = \frac{a_i + b_i x + c_i z}{2\Delta^e} \quad (8-12)$$

$$\left. \begin{aligned} a_i &= x_j z_k - x_k z_j \\ b_i &= z_j - z_k \\ c_i &= x_k - x_j \end{aligned} \right\} \quad (8-13)$$

$$2\Delta^e \approx \begin{vmatrix} 1 & x_i & z_i \\ 1 & x_j & z_j \\ 1 & x_k & z_k \end{vmatrix} = \text{twice area of element} \quad (8-14)$$

x_i, z_i , etc. are the coordinates of the 3 nodes.

Substituting (8-11) into (8-9) yields $f(\vec{A}^e) \neq 0$ which is called the residual. The method of "weighted residuals" using Galerkin weighting N_i^e , then assures a stable and minimized-error solution; that is, we are to solve for \vec{A}_j such that

$$\int_{S^e} N_i^e f(\vec{A}^e) dS = 0 \quad (8-15)$$

for all nodes i of element (e) . We consider the above equations first for one element, then the equations for all elements will be combined to give one large matrix expression for the \vec{A}_j .

Noting that (8-9) contains only surface components, substitute $f(\vec{A}^e)$ in (8-15). For the x component, we obtain

$$\int_{S^e} N_i^e \frac{\partial}{\partial x} (\nabla \cdot \vec{A}^e) ds - \int_{S^e} N_i^e \frac{\partial^2 A_x^e}{\partial t^2} ds + \int_{S^e} \epsilon N_i^e \frac{\partial E_x^i}{\partial t} ds = 0 \quad (8-16)$$

We now apply the integration by parts formula:

$$\int_{S^e} N_i^e \hat{n} \times \nabla D ds = \oint_C (\hat{n} \times \hat{n}_c) N D d\ell - \int_S D \hat{n} \times \nabla N ds \quad (8-17)$$

where \hat{n}_c (with components n_x and n_z) is the normal to the contour C of region S . Equation (8-16) then becomes

$$\begin{aligned} & \int_{C^e} N_i^e \sum_j N_j (\nabla \cdot \vec{A}^e)_j n_x d\ell - \int_{S^e} \sum_j \frac{\partial N_i^e}{\partial x} \left(\frac{\partial N_j^e}{\partial x} A_{xj} + \frac{\partial N_j^e}{\partial z} A_{zj} \right) ds \\ & - \int_{S^e} \frac{\partial N_i^e}{\partial x} \sum_j N_j^e \frac{\partial A_{yj}}{\partial y} ds \\ & - \int_{S^e} N_i^e \sum_j N_j^e \frac{\partial^2 A_{xj}}{\partial t^2} ds \\ & + \int_{S^e} N_i^e \sum_j N_j^e \left(\epsilon \frac{\partial E_x^i}{\partial t} \right)_j ds = 0 \quad (8-18) \end{aligned}$$

for all nodes i in element e . Note that $(\nabla \cdot \vec{A})$ and $\partial E_x^i / \partial t$ are also expressed by interpolating functions and values at nodes in ways similar to (8-11).

We now define the following quantities:

$$\left. \begin{aligned}
 k_{ij}^{exx} &= \int_{S^e} \frac{\partial N_i^e}{\partial x} \frac{\partial N_j^e}{\partial x} ds \\
 k_{ij}^{exz} &= \int_{S^e} \frac{\partial N_i^e}{\partial x} \frac{\partial N_j^e}{\partial z} ds \\
 t_{ij}^e &= \int_{S^e} N_i^e N_j^e ds \\
 b_{ij}^{ex} &= \int_{S^e} N_i^e N_j^e n_x dl \\
 y_{ij}^{ex} &= \int_{S^e} \frac{\partial N_i^e}{\partial x} N_j^e ds
 \end{aligned} \right\} \quad (8-19)$$

etc.

Summing over all elements which contain both i and j , define

$$k_{ij}^{xx} = \sum_e k_{ij}^{exx} \quad (8-20)$$

and similarly for the other k 's, b 's and t 's.

Hence, summing equations (8-18) for all elements we can write a matrix equation

$$[B^x] [\nabla \cdot \vec{A}] - [K^{xx}] [A_x] - [K^{xz}] [A_z] - [Y^x] \left[\frac{\partial A_y}{\partial y} \right] - T \left[\frac{\partial^2 A_x}{\partial t^2} \right] + T \left[\epsilon \frac{\partial E^i}{\partial t} \right] = 0 \quad (8-21)$$

where k_{ij}^{xx} is an element of $[K^{xx}]$, etc., where $[\nabla \cdot \vec{A}]$, $[A_x]$, etc. are column vectors of values at the nodes. There is a similar equation with

x and z interchanged for the other component. Note that in performing the summation over elements the contributions from the contour integrals cancel, except for the contributions from the problem boundary. That is, $[B^x]$ contains only entries at i, j both on the problem boundary, and $\nabla \cdot \vec{A}$ needs to be evaluated only at the problem boundary.

Writing the time derivative as

$$\frac{\partial^2 A_x}{\partial t^2}(t) = \frac{A_x(t + \Delta t) - 2A_x(t) + A_x(t - \Delta t)}{(\Delta t)^2}, \quad (8-22)$$

combining like terms and multiplying by T^{-1} , obtain the matrix equation:

$$\begin{aligned} [A_x(t + \Delta t)] &= -[A_x(t - \Delta t)] + \left[2I - (\Delta t)^2 T^{-1} K^{xx}\right] [A_x(t)] + (\Delta t)^2 \left[\epsilon \frac{\partial E_x^i}{\partial t}(t) \right] \\ &\quad - \left[(\Delta t)^2 T^{-1} Y^x \right] \left[\frac{\partial A_y}{\partial y}(t) \right] + \left[(\Delta t)^2 T^{-1} B^x \right] \left[\nabla \cdot \vec{A}(t) \right] \\ &\quad - \left[(\Delta t)^2 T^{-1} K^{xz} \right] [A_z(t)] \end{aligned} \quad (8-23)$$

and a similar equation for the other component.

The matrix expressions in brackets are all completely defined by the geometry and hence need to be determined only once at the beginning of the problem.

This is the solution to the original differential equation. It is similar to the finite difference solution presented in Section 2, except that surface differentiation has been replaced by matrix multiplication. In other respects the solution is the same as in Section 2: the surface current, \vec{J} , at all interior nodes is obtained by

$$\vec{J}(t) = \frac{1}{Y} \left(\vec{A}_{NS}(t) - \vec{A}(t) \right)$$

where

$$\vec{A}_{NS}(t) = \frac{1}{4\pi} \int_{NS} \frac{\vec{J}(\vec{r}', t)}{R} dS'$$

The boundary conditions enter into (8-23) via the values of $(\nabla \cdot \vec{A})$ at the boundary. We can write this as

$$\begin{aligned} \nabla \cdot \vec{A} &= \nabla \cdot \frac{1}{4\pi} \int_S \frac{\vec{J}'}{R} dS' = \frac{1}{4\pi} \int_S \nabla \cdot \left(\frac{\vec{J}'}{R} \right) dS' \\ &= -\frac{1}{4\pi} \int_S \left(\frac{1}{R^2} + \frac{1}{R} \frac{\partial}{\partial \tau} \right) \left(\vec{J}' \cdot \hat{R} \right) dS' . \end{aligned} \quad (8-24)$$

This integral is separated into self and non-self parts. The self part is evaluated by applying the boundary conditions on \vec{J} , in a manner similar to the procedure in Section 2. The self-integral is difficult when the integrand is the parallel component of \vec{J} at a free edge, since it $\rightarrow \infty$; it can be evaluated by noting that $J_{||} = J_{||0} + \zeta \frac{\partial J_{||}}{\partial \zeta}$ where ζ is the coordinate $||$ to the edge, and by noting that the contribution of $J_{||0}$ is zero.

This solution, just as the one in Section 2 thus requires special treatment at the edges. Further, it requires a large matrix multiplication, instead of simple differencing, at each time step. The advantage is that any shape surface can be treated and that the solution should be more accurate (and hopefully more stable) due to the fact that \vec{A} is continuous to first derivatives over the surface.

8.3 FIRST ORDER SCATTERING CENTER RESPONSE

The impulse response of a target in the physical optics approximation can be shown to be

$$\frac{r_o}{a} h \left(\frac{ct}{a} \right) = \frac{1}{2\pi} \frac{d^2 s}{c^2 dt^2} \quad (8-25)$$

where $S(t)$ is the illuminated area projected on the plane normal to the direction of incidence. The above expression is polarization independent. By considering the interaction of surface currents near the specular point, one obtains a first order polarization-dependent correction to the above. The first order impulse response of a specular point on a smooth curved patch is derived in Ref. 1. With our usual normalizations it is given by

$$\frac{r_o}{a} h \left(\frac{ct}{a} \right) = \frac{1}{2\pi} \left\{ \frac{1}{ac} \frac{ds}{dt} \Big|_o \delta(\tau) + \left(\frac{d^2 s}{c^2 dt^2} \Big|_o \pm \left(\frac{\kappa_1 - \kappa_2}{2} \right) \frac{ds}{cdt} \Big|_o \right) u(\tau) + \dots \right\} \quad (8-26)$$

$$\tau = \frac{ct}{a} - \frac{cT_z}{a}$$

where T_z is the time of incidence. The first two terms are the physical optics terms, the last is the first order correction; the - sign refers to TE polarization, the + sign to TM polarization (see Section 3.2 for coordinate conventions).

For a prolate spheroid with a, b the semi-minor and -major axes:

$$S(t) = \frac{\pi a^2 b (ct\sqrt{B} - c^2 t^2/4)}{B^{3/2}} u(t) \quad (8-27)$$

where

$$B = b^2 \cos^2 \alpha + a^2 \sin^2 \alpha,$$

$u(t)$ is the step function,

α = angle of incidence with respect to the major (\hat{z}) axis.

$\frac{cT_z}{a} = \frac{-2\sqrt{B}}{a}$, is the time of incidence for the target centered at the origin.

Evaluating the terms in (8-26), we obtain

$$P_z = \frac{1}{2\pi a} \frac{ds}{cdt} \Big|_0 = \frac{ab}{2B} \quad (\text{impulse})$$

$$s_z = \frac{1}{2\pi} \frac{d^2 s}{c^2 dt^2} \Big|_0 = - \frac{a^2 b}{4B^{3/2}} \quad (\text{step})$$

(8-28)

$$\frac{K_1 - K_2}{2} = \frac{(b^2 - a^2)}{2a^2 b^2} B^{\frac{1}{2}} \sin^2 \alpha$$

$$s_{z2} = \pm \frac{1}{2\pi} \left(\frac{K_1 - K_2}{2} \right) \frac{ds}{cdt} \Big|_0 = \pm a \left(\frac{K_1 - K_2}{2} \right) P_z \quad (\text{step correction})$$

with

$$\frac{r_0}{a} h \left(\frac{ct}{a} \right) = P_z \delta(\tau) + (s_z + s_{z2}) u(\tau) + \dots$$

For reference we note that the next higher order term in the expression (8-26) is a ramp. The first order correction contributes to this term (see Ref. 1); we can also expect a contribution from the second order correction. We will write this term as

$$(R_{z2} + R_{z3}) \tau u(\tau) , \quad (8-29)$$

$$R_{z2} = \frac{3}{2} P_z a^2 \left(\frac{K_1 - K_2}{2} \right)^2 \pm a \left(\frac{K_1 - K_2}{2} \right) s_z \quad (\text{ramp correction})$$

R_{z3} is to be obtained from the second order correction.

We will now derive the area function of a right circular cylinder of radius a , at oblique incidence ($0 < \alpha < \pi/2$). It is readily seen that $S(t)$ is a piece of an ellipse given by

$$\left(\frac{x}{a}\right)^2 + \left(\frac{\zeta \cos \alpha}{a}\right)^2 = 1 \quad (8-30)$$

where

x is the usual coordinate,

ζ is the coordinate in the yz plane.

At time t' after incidence on corner, the ellipse is truncated by a vertical line (in the end of the cylinder) at

$$\zeta_1(t') = \frac{a}{\cos \alpha} - \frac{t'}{2 \sin \alpha \cos \alpha},$$

i.e.

$$\zeta_1 \leq \zeta \leq \zeta_0$$

$$\zeta_0 = \frac{a}{\cos \alpha} = \text{major axis of ellipse.}$$

Writing

$$x = a \sqrt{1 - \left(\frac{\zeta \cos \alpha}{a}\right)^2}$$

we have

$$S(t') = \left\{ \int_{\zeta_1(t')}^{\zeta_0} 2\rho d\zeta \right\} u(t') \quad (8-31)$$

Hence

$$\frac{ds}{dt'} = \frac{ds}{d\zeta_1} \frac{d\zeta_1}{dt} = \frac{\sqrt{a} \sqrt{t' \left(1 - \frac{t'}{4a \sin \alpha}\right)}}{(\sin \alpha)^{3/2} \cos \alpha} u(t') \quad (8-32)$$

$$\frac{d^2 s}{dt'^2} = \frac{\sqrt{a} t'^{-\frac{1}{2}} \left(1 - \frac{3t'}{8a \sin \alpha}\right)}{2(\sin \alpha)^{3/2} \cos \alpha} u(t') \quad (8-33)$$

We thus obtain for the normalized impulse response

$$\frac{r_0}{a} h \left(\frac{ct}{a} \right) = \left\{ (H_z + H_{z2}) \tau^{-\frac{1}{2}} + (K_z + K_{z2}) \tau^{\frac{1}{2}} + \dots \right\} u(\tau) \quad (8-34)$$

$$\tau = \frac{ct}{a} - \frac{c^T z}{a}$$

$$H_z = \frac{1}{4\pi (\sin \alpha)^{3/2} \cos \alpha}$$

$$K_z = \frac{3}{32\pi (\sin \alpha)^{5/2} \cos \alpha}$$

H_{z2}, K_{z2} are to be obtained from the first order correction (not performed here), and contain the polarization dependence. For a cylinder of length L and radius a centered at the origin

$$\frac{c^T z}{a} = - \left(\frac{L}{a} \cos \alpha + 2 \sin \alpha \right) \quad (8-35)$$

At broadside incidence ($\alpha = \pi/2$) we have

$$s(t') = 2L \sqrt{a} \sqrt{t' \left(1 - \frac{t'}{4a}\right)} u(t') \quad (8-36)$$

Differentiating this twice we obtain the polarization independent terms

$$G_z = - \frac{L\sqrt{a}}{2\pi} ,$$

$$H_z = - \frac{3L}{32\pi\sqrt{a}} ,$$

where the response is

$$\frac{r_0}{a} h\left(\frac{ct}{a}\right) = \left\{ G_z \tau^{-3/2} + (H_z + H_{z2}) \tau^{-1/2} + \dots \right\} u(\tau) \quad (8-37)$$

H_{z2} is to be obtained from the first order correction.

At axial incidence:

$$S(t') = \pi a^2 u(t') \quad (8-38)$$

$$\frac{d^2 S}{dt'^2} = \pi a^2 \delta'(t') \quad (\text{a doublet})$$

We can expect the first order correction to produce the next higher order term (impulse) and also terms of the form $\tau^{-\frac{1}{2}}$ and higher due to the edges. That is, at axial incidence:

$$\frac{r_0}{a} h\left(\frac{ct}{a}\right) = D_z \delta'(\tau) + P_{z2} \delta(\tau) + H_{z2} \tau^{-\frac{1}{2}} u(\tau) + \dots , \quad (8-39)$$

$$D_z = 0.5$$

MISSION
of
Rome Air Development Center

RAADC plans and conducts research, exploratory and advanced development programs in command, control, and communications (C³) activities, and in the C³ areas of information and intelligence. The principal technical mission areas are communications, electromagnetic guidance and control, surveillance of ground and aerospace objects, intelligence collection and handling, information systems technology, ionospheric propagation, solid state science, microelectronics and electronic reliability, maintainability, and compatibility.